THE UNIVERSITY *of* EDINBURGH

Molecular Simulation Studies of Adsorption of Fuel Components and Their Mixtures in Engine Deposits

Alexander J. Harrison

Thesis submitted for the degree of
Doctor *of* Philosophy
at
The University *of* Edinburgh

July, 2015

Declaration

I declare that this thesis and the work described herein are my own, except where explicitly stated otherwise in the text. These have been conducted under the guidance of Dr. Lev Sarkisov at the Institute for Materials and Processes in the School of Engineering of The University of Edinburgh. The work has not been submitted for any other degree or professional qualification.

Alexander J. Harrison

Acknowledgments

First and foremost, I want to thank my supervisor, Lev Sarkisov, for everything he has done to make this project possible. Working with Lev has been one of the most rewarding aspects of my PhD, and I cannot express how grateful I am to him for all his guidance and supervision. Lev's dedication and passion for learning has been a constant source of inspiration for me, and he has shown me a new way of thinking that extends beyond research and into my everyday life. I do not know how I got so lucky, but I am eternally grateful.

I am thankful to Shell Global Solutions for sponsering the project, and my supervisors there, Dr. Roger Cracknell and Jens Krueger-Venus, for the many insightful discussions and support.

I would like to thank everybody at the Institute of Materials and Processes. Such an array of interesting personalities made every coffee room dance unique, and brought joy to even the most disheartening of days. I hope such interactions will continue to bring as many smiles to future generations of students as they did me. The influence of such a pleasant and friendly environment cannot be overestimated.

I want to express particular gratitude for the immense support offered to me by my fellow students within IMP. Although there are far too many to name, I want to thank all the people, past and present, who I met during my time here. There are some individuals, however, who cannot escape particular mention. To Dani and Pedro, to Olga and Ares, to Alex. The friendships we have forged will always remain with me. You have made my time here one that I shall always look back on with the fondest of memories. I want to mention special thanks to Jiri and Piggley for all the good times we shared. Coming home to such a flat brightened my day more times than I can count.

To Nick, Nelly, Sofia and the remaining guys at IMP, and to future generations of students, take heart! We look to you to keep the IMP traditions alive.

Last but not least, I want to thank my family. Thank you to my mother, my father, my sister and (both) brothers for all the unconditional love and support. I would not have made it this far without you.

Preface

Carbonaceous deposits accumulate on the majority of the inner surfaces of internal combustion engines. The presence of these deposits is known to cause impaired engine performance. This is manifested as increased knocking, higher fuel consumption, higher emissions and other adverse effects. One of the proposed mechanisms for this behaviour is the adsorption and desorption of fuel components in the pores within the deposit. The porous nature of the deposits promotes this behaviour, altering the fuel composition and reducing the amount of fuel entering the combustion chamber.

Previous research in this area was aimed at determining the porous structure of the deposits by combining experimental procedures with molecular simulations to investigate adsorption interactions with fuel components. Using a characterisation procedure regularly applied to activated carbons, a molecular model was developed that was able to provide new insights into the deposit structure. This model enabled predictions to be made for the single-component adsorption of normal heptane and iso-octane, two species commonly used as a gasoline reference fuel. Results showed significant adsorption of both species, and highlighted the impact of adsorption into the internal porous structure of the engine deposits.

The aim of this thesis is to further investigate adsorption in engine deposits by expanding the studies to more complex systems. We develop a model to predict the adsorption of normal heptane, iso-octane, toluene and their mixtures in deposits of different origins and under different conditions. The study of multi-component mixtures provides insight into selectivity effects of adsorption under confinement, while at the same time bringing the systems under consideration closer to realistic multi-component mixtures that better represent fuel blends. The study also considers for the first time adsorption of aromatic species, both as a single component and in mixtures, since aromatics have a high presence in gasoline fuel. We explore the influence of molecular structure of adsorbing species, composition of the bulk mixture

and temperature on the uptake and selectivity behaviour of the engine deposits.

We demonstrate that under equilibrium conditions, deposits can adsorb substantial amounts of hydrocarbon species of all types. However, selectivity behaviour in engine deposits was found to be a subtle and complex property, highly sensitive to both pore size and system pressure.

Contents

Chapter 1

Engine Deposits: Origin, Properties and Impact on Engine Performance

1.1 Introduction

Carbonaceous engine deposits accumulate over time on the inner surfaces of all internal combustion engines.[1–3] Although the nature of these deposits and the mechanism of their formation is not fully understood, it has been established that they have a detrimental effect on engine performance.[4–6] In particular, accumulation of deposits leads to loss of power, reduced engine life, increased hydrocarbon emissions, and in the most severe cases to abnormal combustion effects, or engine knocking.[3,4,6] Figure 1.1 shows an intake valve with a substantial accumulation of deposit. A similar valve after deposit removal is also shown for a comparison of how the shape of the valve is changed due to deposit formation. Deposit formation on an engine piston is also shown in Figure 1.2, where it is clearly visible on the piston head and in the groove rings as well.

Due to the prominence of motor vehicles in modern day life, the scale of the automotive industry is immense. In 2012 over 1.5 million vehicles were produced in the UK alone,[7] and the annual economic worth of this industry, within the UK, has consistently been over £10 billion.[8,9] Given the scale of the industry, even a small improvement in engine efficiency can lead to a substantial overall impact on environ-

Figure 1.1: Intake valve with deposit build up. Pictures on the right show a valve after deposit removal for comparison of original shape.

ment and economy. The fuel efficiency of the car, its life-span, level of emissions and other performance characteristics could be improved if the formation of the deposits was prevented. Not surprisingly, substantial research efforts have been concentrated in recent years on the development of advanced fuel formulations and additives which would prevent formation of the deposits. A recent report from the Technical Committee of Petroleum Additive Manufacturers in Europe (ATC) states the world-wide turnover for these fuel additives is €7,000 million Euros.[10] Estimates show that up to 19 % of these additives are dedicated to deposit control[10] (see Appendix A).

Formulation of these advanced fuels and additives requires better description of how the deposits form, their properties (structure, composition) as well as a detailed understanding of mechanisms for the adverse influence of the deposits on the engine performance. This thesis makes several contributions to this field. Specifically, we use physical adsorption as a technique to provide a better structural characterization of the deposits in terms of their porosity and pore structure. Furthermore, we use the obtained experimental data to construct predictive molecular models for

Figure 1.2: Combustion engine piston, showing deposit build up on the piston head as well as within the groove rings.

adsorption in engine deposits. Using these models we explore whether adsorption of fuel components in the deposits is significant under relevant conditions and how it may contribute to the overall impact on the engine performance. This thesis continues a series of previous contributions to this field with a particular emphasis on multi-component systems.

In this chapter, we will review what is known about the composition and structure of engine deposits so far, the mechanisms of their formation and possible mechanisms responsible for the deteriorated engine performance, including adsorption. We will then provide the justification for the construction of predictive molecular models, leading to the formulation of the objectives of this thesis. The chapter will conclude with the brief review of the remaining structure of the thesis.

1.2 Composition, Structure and Formation of Engine Deposits

A fully comprehensive review of engine deposits is beyond the scope of this thesis, and only important features necessary for this work will be covered. Several in-depth reviews are available, with Kalghatgi being a commonly cited authority in the field,[11,12] while Shu et al. recently published a more up-to-date review of experimental characterisation studies involving a specific class of deposits.[13] There are several main types of engine deposits, classified according to their location within

the engine. Key properties such as the composition, structure, formation mechanism and impact on engine performance also vary in details according to the deposit type.

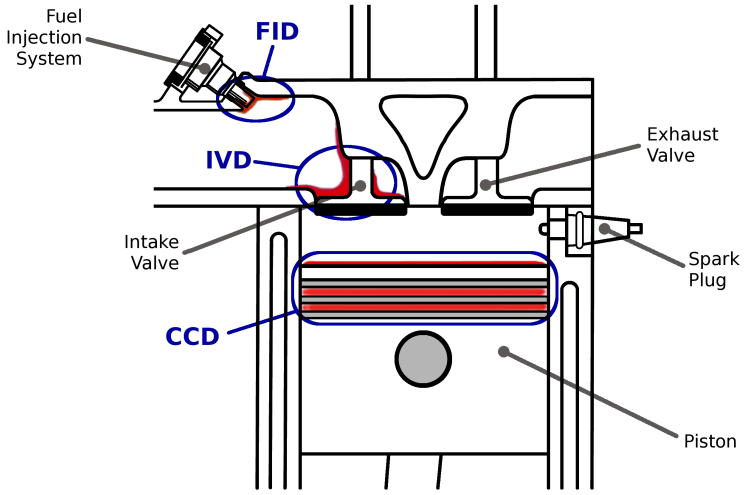

Figure 1.3: Schematic diagram showing key areas of deposit formation within a combustion engine. The areas of formation around the fuel injection system, intake valve and on combustion chamber surfaces deposits are highlighted in red. FID is for Fuel Injection Deposit; IVD is for Intake Valve Deposit; CCD is for Combustion Chamber Deposit. Adapted from Heywood.[4]

Figure 1.3 shows a simplified schematic of the combustion chamber as well as the intake and exhaust manifolds. Highlighted are the positions where the three main types of engine deposit can be found, including fuel injection system deposits forming around the nozzle of the injection valve, intake valve deposits (IVDs) forming on the valve and around the intake manifold, and combustion chamber deposits (CCDs), forming within the combustion chamber. CCDs form on the piston cylinder head, as well as within the piston grooves.

The mechanisms of deposit formation are complex and still not clearly understood, however it is commonly accepted that both fuel and lubricating oil play important roles in their generation.[2,5,11,14–16] This is apparent from the chemical composition of deposits, which contains elements from both fuels (Cu, known to be a fuel impurity[14]) and lubricants (Zn, Ca, Mg, S, P, Si). As an illustration, tables 1.1 and 1.2 provide elemental compositions for two samples of different types of deposits (IVD and CCD) recently reported by Costa et al.[17] Both samples are composed predominantly of carbon, but with a significant presence of a broad range of other

elements. There are also obvious differences in the compositions of the samples. This is rather expected as the composition of the deposits depends on a number of factors, including location in the engine, type of engine, fuel and lubricating oil, as well as the engine operation regime. This is inline with other studies describing engine deposits as predominantly carbonaceous but accompanied by a complex composition profile.[5,14]

Element	C	O	H	Zn	Ca	P	Mg	S	N	Cu	Na	F	Si	Al
(% m/m)	65.0	13.0	5.0	4.5	4.0	2.1	2.0	1.4	1.0	0.7	0.5	0.3	0.1	0.1

Table 1.1: Elemental composition of a sample of combustion chamber deposit, adapted from Costa et al.[17]

Element	C	H	Zn	O	N	Ca	S	Fe	P	Pb	Cu
(% m/m)	74.5	6.7	2.9	2.5	1.9	1.5	1.5	1.4	0.9	0.4	0.3

Table 1.2: Elemental composition of a sample of intake valve deposit, adapted from Costa et al.[17]

Engine deposits are also porous. However, systematic characterisation of their porosity proved to be challenging and publications in this area remain scarce. Zerda et al. applied density functional theory to carbon dioxide experimental isotherms to determine the internal structure of combustion chamber deposits. Distribution of macropores was investigated using mercury porosimetry, and surface areas were investigated using both mercury porosimetry and Brunauer - Emmett - Teller (BET) methods. They observed that the majority of pores were around 5 Å in size, and internal surface areas were in the range of 100 - 200 m^2/g.[2,6] Transmission electron microscopy (TEM) images of a CCD sample were also reported to show clear presence of elements of graphitic, lamellar structure. This TEM image is shown in Figure 1.4. The lamellar structure is highlighted with red lines to aid visibility, and is present across the majority of the surface. The layered nature of the surface is very important for this thesis as it provides a justification for the modelling approaches adopted in this work and described in the subsequent chapters.

Physical adsorption of nitrogen and argon at cryogenic temperatures and carbon dioxide at ambient temperature further complement the arsenal of tools traditionally used for porous material characterisation. Zerda and co-workers made several

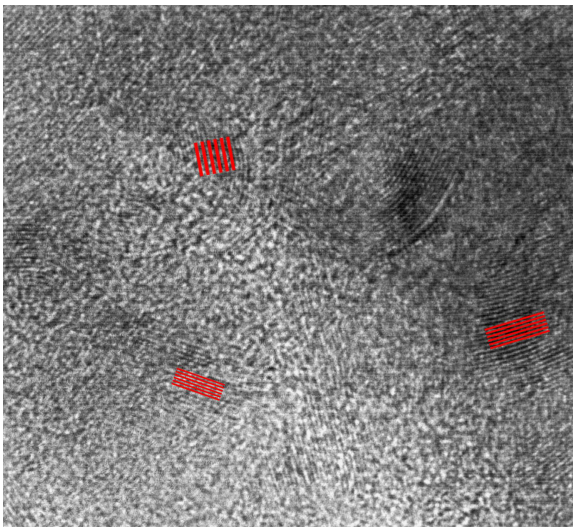

Figure 1.4: A TEM image of the surface of a sample of combustion chamber deposit, reproduced from Zerda et al.[2]

attempts to apply these standard characterisation techniques to the engine deposits, including adsorption of both nitrogen at 77 K and argon at 87 K. However, their results do not conform to the expected behaviour of a microporous material and interpretation of these results is difficult. Consider an adsorption isotherm for nitrogen at 77 K, shown in Figure 1.5. It features substantial adsorption hysteresis (not expected for a microporous material) and the shape of the isotherm does not conform to the expected Langmuir or BET shape, preventing analysis of this isotherm using these classical approaches. Most importantly, the results published by Zerda and co-workers do not seem to correspond to a fully equilibrated isotherm. Specifically, the two sets of adsorption data, one with three minutes of equilibration time per point and the other with nine minutes per point, show substantial differences and drift in the adsorbed density, questioning all consequent analysis presented in the article based on this data. This issue was later revisited by Costa and co-workers (unpublished data), who explored the adsorption of nitrogen at 77 K with equilibration times of up to 60 minutes. These isotherms are shown in Figure 1.6, however it still remains unclear if this time is sufficient for equilibration. This equilibration time is not typical for activated carbons (typically, minutes per point), indicating that, although carbonaceous in composition and featuring elements of lamellar structure, engine deposits are not activated carbons from the adsorption behaviour perspective.

Formation mechanisms of engine deposits are still not clearly understood, des-

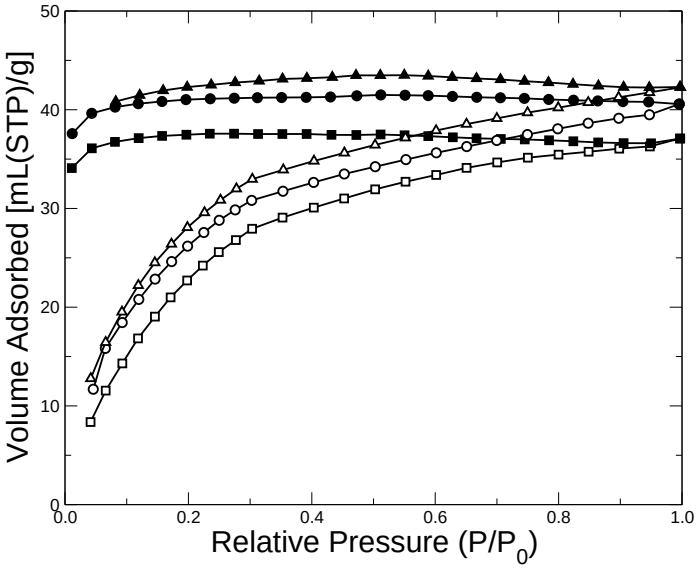

Figure 1.5: Reported gas adsorption (open symbols) and desorption (closed symbols) isotherms on CCD engine deposit. Data shown includes: nitrogen at 77 K, equilibration time of 3 minutes per point (squares); nitrogen at 77 K, equilibration time of 9 minutes per point (circles); argon at 87 K, equilibration time of 3 minutes per point (triangles). Data reproduced from Zerda et al.[2]

pite numerous studies on this subject.[1,5,18] Here we briefly review some of the proposed mechanisms. Again, it is important to note that these mechanisms depend on the location of the deposits within the engine, as these locations would be exposed to different thermophysical conditions (temperature, pressure, ongoing combustion reactions). Specifically, the surfaces of intake valves have, on average, lower temperatures compared to the surfaces within the combustion chamber during engine operation. It is believed that during the injection of fuel, the lighter hydrocarbons evaporate off the surface of the valves leaving behind a layer of heavier species. These are then oxidised which, over time, leads to build up of the intake valve deposits.[1,11] Formation of fuel injection deposits occurs via a similar mechanism to that of intake valve deposits.[11]

For higher temperature conditions, such as in the combustion chamber, the formation mechanism is believed to be different. The review presented by Kalghatgi[12] is quite extensive in collating together ideas about deposit formation, some of which have also been supported by more recent works.[14,18,19] It is believed that fuel and

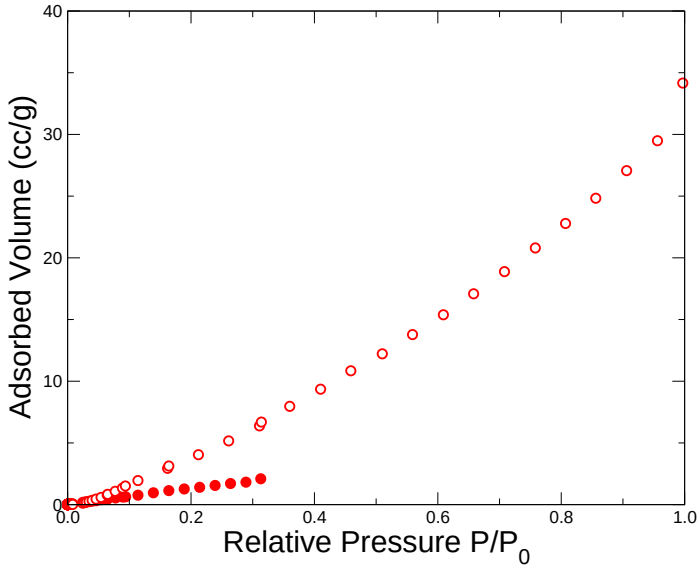

Figure 1.6: Nitrogen adsorption isotherms at 77 K on a sample of IVD (Costa et al, unpublished results). Data for equilibration time of 3 minutes per point (closed circles) and 60 minutes per point (open circles) is shown.

lubricant components undergo addition/substitution reactions of radicals, forming coordinated oxidation products. These products condense onto the engine surfaces. The condensed species undergo polymerisation and form deposit precursors layered on the engine surface. This precursor formation is a key stage in CCD formation, and depends very strongly on surface temperature.

There is strong evidence that the formation process then changes as the deposits grow.[1,5,11,12] Deposits have high thermal insulating properties and so, as deposits thicken, the formation process takes place under higher temperatures. This causes a stark difference in deposit properties across their thickness, as reported by Caceres et al.[14] Specifically, they observed a lower lacquer-like layer forming close to the metal engine surface, and a more carbonaceous layer forming on top of the first layer. Altin and co-workers suggest two other variations of the deposit formation processes at higher temperatures.[1] The first involves decomposition of hydrocarbons into elemental hydrogen and carbon, followed by metal-catalysed deposition of carbon. The second involves the polymerisation of hydrocarbon species into larger poly-nuclear aromatic hydrocarbons. These then nucleate and are "baked" through the exposure to high temperatures. These observations are inline with the structurally different

types of deposit found within the combustion chamber.

As deposits are formed from components of both fuel and lubricating oil, their composition is directly linked to the composition of the resulting deposit as well as to the process of its formation.[12,13,16] Specifically, fuels with higher values of molecular weight and boiling point promote deposit formation.[11] It is also important to note that several factors, affecting formation of the deposits, may be closely coupled with each other and with other parameters of engine operation, such as the temperatures of engine surfaces and flame temperatures in the combustion chamber.[1,3,5,11,18] As the temperature in certain parts of the engine is also closely tied to the combustion process, the air-fuel ratio of the engine has a substantial impact on deposit formation.[3,11,12] This provides a brief overview of the factors, influencing deposit formation and properties, simply highlighting the complexity of processes involved.

1.3 Effects on Engine Performance

1.3.1 Normal Engine Operation

To understand the mechanisms of deposit impact upon the combustion engine it is important to first review how the engine operates under normal working conditions. Figure 1.7 shows the different stages of a four-stroke combustion engine. Before the first stroke, a mixture of air and fuel is vapourised in the intake system. The initial stroke (first frame from the left) then draws this mixture into the combustion chamber by passing through the intake valve. This is known as the induction stroke. The mixture is pressurised by the compression stroke (second frame from the left), and the mixture is ignited via the spark plug just before the piston reaches top-dead centre (the highest point the piston reaches during one cycle of the crankshaft). In ideal working conditions, a single flame-front will propagate through the fuel-air mixture, dramatically increasing the pressure and causing the expansion stroke (third frame from the left). The generated power from this stroke is around five times that required to compress the unburned mixture. The final stroke is the exhaust stroke (the frame on the right) where the burned gases are removed from the combustion chamber via the exhaust outlet. The engine is now ready for the next induction stroke.

During the full cycle, there are substantial variations in temperature and pressure within the engine. The actual values of temperature and pressure depend on the

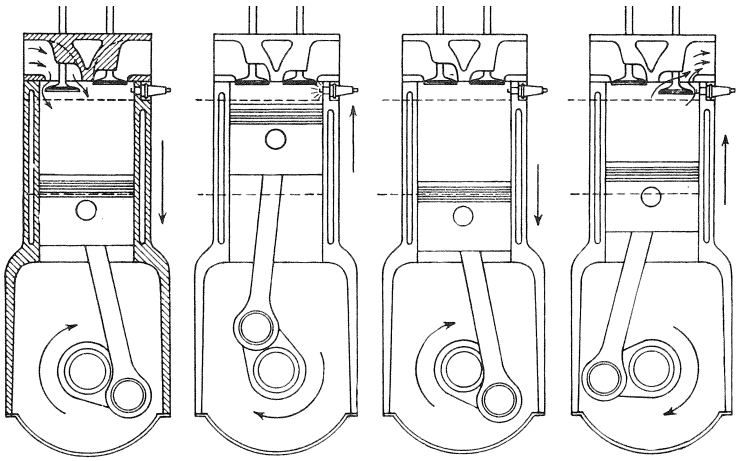

Figure 1.7: Schematic diagram of the stages of a four-stroke combustion engine. From left to right these include the induction stroke, the compression stroke, the expansion stroke and the exhaust stroke. Reproduced from Heywood,[4] Page 10, with the permission of McGraw-Hill Education.

engine configuration, however; Figure 1.8 shows a typical example of these variations. At a typical 2100 rpm, this cycle is repeated about every 0.06 seconds (an engine cycle consists of two full revolutions of the piston in order to achieve the four-strokes). While the graph shown in Figure 1.8 depends heavily on many factors such as engine design and load, we use it here as an example of the highly transient conditions within the engine.

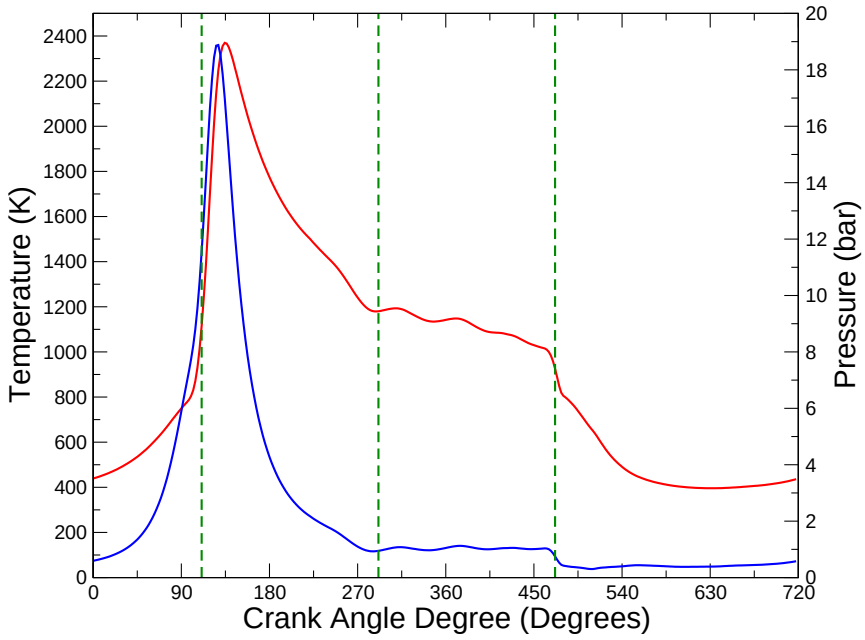

Figure 1.8: Example profile of conditions within a combustion chamber. The red line shows the temperature (left-side scale) and the blue line shows pressure (right-side scale). Dashed green lines separate the four strokes of the engine, described in Figure 1.7. From left to right, these are: compression, expansion, exhaust and induction strokes. Data is provided by Shell Global Solutions through personal communication.[20]

1.3.2 Impact of Deposits on Engine Performance

The mechanisms of how deposits interfere with normal engine operation depend on location. Deposits on fuel-injection systems, for example, tend to form on the nozzle of modern injection systems. This affects both the flow-rate of fuel and the spray pattern, reducing the fuel efficiency of the engine.[1] Intake valve deposits are those forming on and around the intake valve. Formation happens both on the valve itself, and the valve seat where the valve rests when closed. The deposits tend to be sticky, and cause problems with the opening and closing of the valve. By physically restricting the air-flow into the engine, these deposits reduce the amount of fuel in the combustion chamber, lowering the overall engine power. An array of problems could occur if the valve is unable to seal properly due to deposit build up. These could include loss of pressure during expansion and compression strokes, or back-

flow of exhaust gases into the engine. Intake valve deposits can also act as thermal heat-stores (although this is usually associated with combustion chamber deposits), preheating the fuel-air mixture which affects the combustion process.

Combustion chamber deposits can alter the combustion within the engine in a very specific way, promoting a phenomenon known as *knock*.[4,6] Normal combustion, prompted by spark-ignition, causes a single flame front to pass through the compressed fuel-air mixture. The area immediately before this flame-front is called the end-gas region. Abnormal combustion occurs if a portion of the end-gas region were to ignite before the flame front arrives. This premature combustion causes localised very high pressure variation, and is often characterised by a knocking sound, hence the name knock. The increased rate of combustion from knocking causes a decrease in the power output, as well as potentially damaging the engine due to the pressure spikes. The chance of knock occurring in an engine increases when the temperature and pressure of the compressed mixture are higher than expected. Deposits contribute to this by acting as thermal heat stores, pre-heating the air-fuel mixture in the case of IVDs and reaching temperatures high enough to cause surface-ignition of the end-gas region in the case of CCDs. Deposits forming on the combustion chamber walls can also have an insulating effect, due to the low thermal conductivity and porous structure.[3,6] Over multiple cycles the cylinder temperature rises, promoting knock as well as increasing nitrogen oxide emissions.

CCDs can also have a volumetric affect on the combustion dynamics, altering the compression ratio[14] of the fuel-air mixture. Modern fuel-injection is electronically controlled by multi-port injection systems. Sophisticated control of these injection systems provides a higher torque and increased engine power through sensitive and accurate regulation of the compression ratio. Altering volumetric capacity via engine deposits physically present inside the engine is counter-productive to these detailed control systems.[3]

A mechanism of performance degradation that is believed to be universal for almost all types of engine deposit is the adsorption of fuel components, due to the highly porous nature of the deposits. In fact, adsorption in engine deposits is widely accepted as the most influential contribution to changes in engine performance. According to the mechanism, the deposits act as a sponge, up-taking fuel components (CCDs, IVDs), as well as combustion products (CCDs). This causes the engine to operate with a lower amount of fuel than intended. It has been suggested that these adsorbed species could further contribute to deposit formation via carbonisation

while in the adsorbed phase. There is also strong evidence that engine deposits contribute to increased greenhouse gas emissions by desorption some of the previously adsorbed components at other stages of engine operation.[14] Finally, if adsorption was selective towards a certain type of species, it is possible that this process would affect the fuel mixture composition, altering engine operation behaviour and resistance to knock.

Although there is agreement on the importance of adsorption as an influential factor in the engine performance deterioration, there is very little published research properly exploring, assessing and quantifying this mechanism. This lack of insight, coupled with the expectation of strong adsorption behaviour of deposits, provides motivation for this project, in which we intend to develop a better understanding of the structure of the deposits and assess the extent of adsorption of fuel components in these materials under relevant conditions. This is however an immensely challenging task to pursue within an experimental approach and below we provide a justification for the development of the predictive adsorption models based on molecular simulations.

1.3.3 Adsorption and Molecular Modelling

Before approaching the issue of adsorption in engine deposits, the terminology of adsorption must be defined. It is also necessary to assess the capabilities of current experimental adsorption methods. Adsorption is defined as an increase in the density of a fluid (known as the adsorbate) at the surface of a solid or a liquid fluid (the adsorbent), and is a result of interactions between the fluid and the surface. The types of interactions involved determine if adsorption is chemisorption or physisorption; in chemisorption chemical bonds form between the adsorbate and the adsorbent, while physisorption involves dispersion and electrostatic interactions. Physical adsorption of nitrogen and argon at cryogenic temperatures has been used as one of the principal techniques in porous material characterisation to obtain surface area, porosity and pore structure. On the other hand, in the chemical industry adsorption is exploited in catalytic processes (such as hydrocracking using zeolites) and adsorption separation processes. For example, in dehumidification operations, sulphur oxide removal from vent streams, stripping carbon dioxide from power plant exhausts and waste-water treatment from chemical processes, etc. As such, the thermodynamics of adsorption (both from classical thermodynamics and statistical mechanics per-

spectives) is a fairly established field. We will introduce the key concepts within this field in the later chapters.

Here we consider physical adsorption of fuel components in the carbonaceous engine deposits. It is important to acknowledge that the engine environment during operation is very complex. The system consists of a complex ensemble of chemical species (typically hundreds) undergoing chemical reactions. Pressure and temperature inside the engine vary substantially during the engine cycle, as seen from Figure 1.8, while the cycle is repeated with very high frequency. This frequency also changes depending on the power demand of driving conditions at the time. It is impossible to design an adsorption experiment which would address the main topic of this thesis under realistic conditions in the engine. And even if such a bench scale system were possible, the obtained results are unlikely to provide any clear insights as they would be obtained from a system with many processes occurring simultaneously, while being strongly coupled with each other. Therefore, a series of simplifications must be introduced in order to make the system more amenable to studies of one specific process of interest, namely adsorption. Hence, in the simplified systems there will be no combustion reactions, while temperature and pressure will be held at fixed values. To justify this last simplification, we acknowledge that in a highly transient systems we would expect the kinetics of adsorption to strongly impact the adsorption behaviour. However before we can approach the complicated task of modelling these kinetics, it is necessary to first determine the maximum extent to which adsorption *could* occur. By fixing the values of temperature and pressure, this maximum extent is what we focus on in this research.

These fixed values of pressure and temperature must be still relevant to the typical conditions in the engine. Temperatures are based on engine surface temperatures around the areas of interest. Under steady-state conditions of a running engine these tend to remain fairly constant due to the engine cooling systems. For intake valve deposits a temperature of 390 K was chosen, while 420 K was chosen for combustion chamber deposits. These temperatures are based both on typical figures for surface temperatures in these areas[4] as well as the temperature profile from Figure 1.8. For IVDs, this is the lowest temperature during the induction stroke, where the air/fuel mixture is drawn across the intake valves and into the combustion chamber. For CCDs, the most favourable temperature for adsorption is that during the start of the compression stroke. The values of pressure can be also guided by the data in Figure 1.8, and will be discussed in later chapters.

With the cyclic operation of the system removed and temperature and pressure fixed at specific values for each adsorption experiment, the complex chemical composition of the system still remains a challenge. As a further simplification, one could consider only a small selection of components, representative of several key classes of fuel components (linear alkanes, branched alkanes, aromatics) and their mixtures. Unfortunately, experimental measurements of adsorption of complex alkanes (and even more so their mixtures) still remains challenging. The equilibration time for complex species becomes incredibly long due to slow dynamics of the adsorption process. As an example, adsorption of normal butane at room temperature takes 36 hours per isotherm point, and each isotherm requires seven to ten points to accurately capture the isotherm shape. In addition to this, experimental isotherms often require several repeats to ensure the isotherm is accurate. As only one experiment can be performed per adsorption rig, obtaining enough isotherms for thorough investigation would be a very time-consuming process. For mixtures (even as simple as binary) the situation becomes even more complex. The equilibration times are likely to be even longer and the experimental processes require additional gas chromatography steps to establish concentrations of adsorbed species. This provides motivation to develop predictive models of adsorption in engine deposits, which would circumvent the experimental constraints.

Such predictive models are based on one of two possible methodologies; density functional theory (DFT) or molecular simulation. Density functional theory seeks to establish the equilibrium adsorption properties of a system as a function of the adsorbed fluid density, while molecular simulations provide exact solutions to the statistical mechanical equations for adsorbed systems. Both methods are based on statistical mechanical theories and are used to establish individual adsorption isotherms of a desired system. Because of the use of statistical mechanics, these methods are not limited by physical conditions available in a lab environment, and can be run in parallel for multiple systems and most importantly, can investigate multi-component systems with only a slight increase in difficulty compared to single-component systems.

Early investigations into adsorption behaviour tended to favour DFT due to the lower computational cost, and one of the earliest applications of DFT to adsorption under confinement is that of Tarazona et al.,[21] who investigated phase transitions at fluid interfaces in confined pores. Another application was that of Seaton and Quirke, who used isotherms calculated from mean-field density functional theory to

determine information on the solid structure of porous carbons.[22] Such information is vital for the development of predictive models, and significant research has been invested into this challenge using DFT methodologies.[23–31]

As computer processing power advanced over the last half-century, computational investigations have begun to shift away from DFT towards the more computationally intensive molecular simulations.[26,31–37] These are able to provide greater accuracy to adsorption behaviour as they provide exact solutions to the statistical mechanical equations, are generally considered easier to implement,[38] and are more versatile than the DFT methodologies. It is for these reasons that we use molecular simulations in this work. With this in mind, the objectives of the thesis begin to take shape and are outlined in the next section.

1.4 Objectives and Outline of this Thesis

The main objective of this thesis is to understand to what extent engine deposits can adsorb components of the fuel and their mixtures under relevant, fixed conditions of temperature and pressure. In this endeavour we build on a series of previous studies by Costa and co-workers.[39,40] Specifically, we revisit their model with a view to identify possible strategies to make it more systematic and detailed. Using these new, more detailed models, the adsorption tendencies of engine deposits are investigated with regards to key hydrocarbon groups chosen to represent the wide array of species found within a gasoline fuel. Finally, the investigation is expanded to multi-component systems including binary and ternary mixtures of the chosen adsorbate species. The structure of this thesis is as follows.

Chapter 2 provides the theoretical background for the statistical thermodynamics of adsorption underlying this work. We then go on to discuss some key concepts of molecular simulations, including molecular forcefields and the development of molecular models for porous materials. There follows a brief review of some of the more advanced Monte Carlo techniques used for molecular simulations of alkane species. Finally Chapter 2 finishes with a detailed description of the methods used for structural characterisation of porous materials, originally based on the method of Davies and Seaton.[41–43]

In Chapter 3 we present an up-to-date review of the recent work by Costa and co-workers on the adsorption of fuel components in engine deposits. This includes

the motivation and objectives of the original project, as well as key stages of model development. We present the characterised engine deposit samples and review model accuracy via comparisons of predicted isotherms to experimental data. Initial predictions for fuel components at representative engine conditions are shown. Finally, the conclusions are presented along with a discussion on the limitations of the original work by Costa and co-workers and more specific objectives of the current thesis.

Chapter 4 is dedicated to understanding the adsorption behaviour of alkanes in individual slit pores, and so laying the ground work required for future chapters of this thesis. This is done in two parts; in the first we take the opportunity to explore selectivity effects between branched and linear alkanes in the slit pore model. This is an area of research that has received little attention, and is fundamental to the later studies of this work. In the second part of the chapter we study the strength of adsorption interactions in a slit pore by considering Henry's constants and isosteric heats of adsorption as functions of pore width. Information on the simulation methods and parameters is also included at the beginning of this chapter.

In Chapter 5 we explore how adsorption in individual slit pores is translated into adsorption behaviour across a porous material consisting of many pores of varying size. In this chapter we revisit the characterisation process used by Costa and co-workers using a more detailed generation procedure. These changes lead to the development of new engine deposit models, and in this chapter we provide some background on the motivation for these changes, as well as exploring their impact on previous adsorption predictions and conclusions.

In Chapter 6, we collate the investigations of the previous two chapters and present predicted adsorption isotherms for single and multi-component mixtures of key fuel components in two types of engine deposit. We revisit the single-component systems of i-octane and n-heptane using the new model of engine deposits, as well as expanding the studies to include toluene, a common component of gasoline fuels. We present adsorption isotherms for binary and ternary mixtures, and investigate selectivity effects that arise in these systems. Finally, we examine the extent of adsorption uptake, and discuss the impact of engine deposits on the operation of the engine. In the final chapter, Chapter 7, we summarise the conclusions of this work and speculate on future directions that this research can follow.

Chapter 2

Molecular Simulations of Adsorption: Theory and Practice

The main aim of this thesis is to investigate to what extent fuel components can adsorb in engine deposits. This aim is approached by using molecular simulations to predict the adsorption of single, binary and ternary mixtures of specific hydrocarbons into a model of engine deposits based on a slit pore representation of the structure. To achieve this, a wide variety of computational tools are required. Although the theoretical foundation of each of these tools is an immense subject in itself, in this chapter we seek to provide a condensed overview of the basic principles underpinning each of these tools. These include the statistical thermodynamic foundations of molecular simulation, molecular models describing interactions within the systems of interest, advanced molecular simulation methods required for adsorption of flexible alkane molecules, and specific methods, combining molecular simulations and experimental data, to obtain the structure of a porous material.

2.1 Statistical Thermodynamics of Adsorption

Statistical thermodynamics connects the behaviour of systems on a microscopic level with macroscopic thermophysical properties. Both macroscopic and microscopic behaviours of a system are a result of interactions between the molecules on a microscopic scale. Molecular simulation is a class of computational methods within the greater realm of statistical and molecular thermodynamics that allows macroscopic

system properties to be obtained, given information about molecular interactions. In this section we introduce several concepts, within statistical thermodynamics and molecular simulation fields, directly relevant for the thesis.

Consider a system of N particles in a volume, V, at a fixed temperature T. The current configuration of the system is characterised by the particular locations and velocities (or momenta) of the particles. Such a configuration is called a microstate, and a collection of all possible microstates is called an ensemble. The ensemble corresponding to the constant N, V and T conditions is called the canonical ensemble. If we accept a quantum mechanical point of view (that is, instead of classical continuous values of positions and momenta we describe the system using discrete energy values), each microstate occurs with a probability defined by the Boltzmann distribution:

$$p_i = \frac{e^{-E_i/k_BT}}{\sum_i e^{-E_i/k_BT}} \tag{2.1}$$

where p_i is the probability of observing microstate i, E_i is the energy of microstate i, and k_B is the Boltzmann constant. The numerator of Equation 2.1 is an important quantity in statistical thermodynamics, called the partition function. This function contains information about all possible microstates of the system. In the above equation it is acting as a normalisation factor and it is often written as $Q(N,V,T)$ in a short-hand notation:

$$Q\left(N,V,T\right) = \sum e^{-E_i/k_BT} \tag{2.2}$$

The canonical partition function is linked to the Helmholtz free energy, a macroscopic property, through the bridge function:

$$F = -k_BT \ln Q(N,V,T) \tag{2.3}$$

An equilibrium of the system under constant (NVT) conditions corresponds to the minimum of the Helmholtz free energy and thus the bridge function establishes the definitive link between the microscopic properties of the system (the canonical partition function) and the macroscopic thermodynamic properties.

The key principle of statistical thermodynamics is the notion that the time-averaged macroscopic property of the system is equal to the ensemble average. For

this to be true, the system must be ergodic. Ergodic systems, given infinite time, pass through every possible configuration of the system. This implies that various macroscopic properties of the system can be simply obtained by averaging their values for individual microstates over the probability distribution of microstates. In mathematical terms, this leads to:

$$M = \langle M \rangle_{Ensemble} = \sum M_i p_i \tag{2.4}$$

where M is the property of interest**.** In the formulations above we a used quantum-mechanical framework solely for the convenience of notation. Within the modelling approaches employed in this work, intermolecular interactions are described by classical potentials, and therefore a more appropriate description should be based on classical mechanics. In classical mechanics there are no discrete energy levels, and the configurations of the system can be characterised by continuous values of position ($\mathbf{r}$) and momenta ($\mathbf{p}$), forming the so called *phase space*. The starting point in the classical treatment of the partition function is the Hamiltonian, which states the total energy of the system as a function of the system's evolution within the phase space. The Hamiltonian is formed from two contributions: the kinetic energy, that accounts for the momenta of each particle within the system; and the potential energy, a function of the particle positions:

$$\mathcal{H}(\mathbf{r}, \mathbf{p}) = \sum_{i=1}^{i=N} \underbrace{\frac{\mathbf{p}_i^2}{2m_i}}_{\text{Kinetic}} + \underbrace{U_i(\mathbf{r})}_{\text{Potential}} \tag{2.5}$$

The classical variant of Equation 2.2 is obtained by expressing energy as the Hamiltonian and integrating the system over all possible states, i.e. all possible positions and momenta. The classical canonical partition function is therefore given by:

$$Q_{classical} = \frac{1}{N! h^{3N}} \int_{\mathbf{r}} \int_{\mathbf{p}} e^{-\mathcal{H}(\mathbf{r},\mathbf{p})/k_B T} \, d\mathbf{r} \, d\mathbf{p} \tag{2.6}$$

where h is Planck's constant, and h^{3N} accounts for the volume in classical phase-space occupied by each quantum state for N particles within the system. $N!$ accounts for indistinguishability of N particles. The kinetic portion of the Hamiltonian will integrate out, leading to the partition function of an ideal gas. The remaining part is known as the configurational integral. The classical partition function for the

canonical ensemble is then given by:

$$Q_{classical} = \underbrace{\frac{1}{N!\Lambda^{3N}}}_{\left[Q_{ideal}/V^N\right]} \underbrace{\int_{\mathrm{r}} e^{-U(\mathbf{r})/k_BT}\, d\mathbf{r}}_{\text{Configuration Integral}} \tag{2.7}$$

where Λ is the thermal de Broglie wavelength, related to Plank's constant by:

$$\Lambda = \frac{h}{\sqrt{2\pi m k_B T}}$$

Here, m is the mass of the particles. The configurational integral contains information about all intermolecular interactions in the system, and therefore it is this integral where deviation of the system from the ideal gas is represented.

The focus of this thesis is on the adsorption in porous materials. A porous material is an open system at fixed volume and temperature, in order words, it corresponds to the grand canonical ensemble (μ, V, T), with μ being the chemical potential of the adsorbing species. The partition function for the grand canonical ensemble can be seen as a sum of all canonical partition functions formulated for all possible values of the number of particles in the system from zero to infinity:

$$\Theta(\mu, V, T) = \sum_{N=0}^{\infty} \frac{1}{N!} \frac{1}{\Lambda^{3N}} e^{\mu N/k_BT} \int e^{-U(\mathbf{r})/k_BT} d\mathbf{r}^N \tag{2.8}$$

With knowledge of the partition function, it is possible to derive all other thermodynamic properties of the system. In particular, the grand potential is a macroscopic system property and is linked to the grand canonical partition function via:

$$\Omega = -k_BT \ln \Theta\left(\mu, V, T\right) \tag{2.9}$$

The main property we are interested in obtaining from this consideration is the average adsorbed density at a fixed chemical potential of the adsorbing species (which can be related to the bulk pressure, concentration or fugacity). From Equation 2.4, an approximation of this is taken by averaging the adsorbed density over a large number of generated microstates. The equation then becomes:

$$\langle \rho\left(\mu VT\right) \rangle \approx \frac{1}{S} \sum_{i=1}^{i=S} \rho_i \tag{2.10}$$

where S is the number of microstates sampled.

For convenience, the necessary components of the theory have been formulated using single component system of mono-atomic molecules. This formalism can be easily extended to multi-component systems and, with a slightly more involved notation, to complex molecular species. In general, the potential energy component in the Hamiltonian describes interactions between the molecules, external potential fields on the molecules (for example, emanating from the walls of the porous material) and also within the molecule, if it is a flexible entity made of several atoms. Calculation of the average properties according to Equation 2.8 requires a model that describes these contributions to the interaction energy. In the next section we will describe these contributions in more detail.

2.2 Molecular Forcefields

Consider a system of several single-atom molecules, for example argon, confined within a slit pore (Figure 2.1). The slit pore can be considered as the simplest model of a porous material. It has played an important historical role in understanding the thermodynamics of adsorption and confined systems, and is also of a particular importance for this thesis.

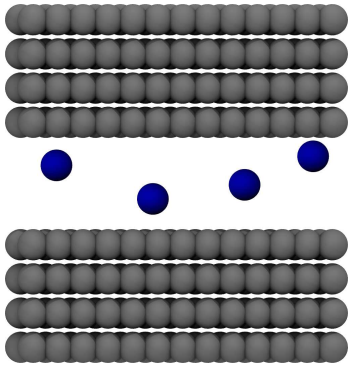

Figure 2.1: Schematic diagram of a slit-shaped pore showing adsorption of some mono-atomic species (blue). The walls (grey) are made of stacked graphene layers.

The dispersion interactions between the confined argon atoms can be described using the well known 12-6 Lennard-Jones potential, defined as:

$$U = 4\varepsilon_{ij}\left[\left(\frac{\sigma_{ij}}{r}\right)^{12} - \left(\frac{\sigma_{ij}}{r}\right)^{6}\right] \tag{2.11}$$

where ε_{ij} is the potential well depth and σ_{ij} is the finite distance at which the interaction potential is zero. Equation 2.11 has two main contributions: the attractive term, $(\sigma/r)^6$ arising from longer-range forces such as van der Waals, or dispersion forces; and the repulsive term, $(\sigma/r)^{12}$, that accounts for the short-range interactions due to overlapping electron clouds. The subscripts ij in Equation 2.11 indicate a combination of interaction parameters taken from two different atoms, i and j. In this work, these combined parameters are calculated using the standard Lorentz-Berthelot mixing rules, defined as:

$$\begin{aligned} \varepsilon_{ij} &= \sqrt{\varepsilon_i \varepsilon_j} \\ \sigma_{ij} &= \frac{\sigma_i + \sigma_j}{2} \end{aligned} \tag{2.12}$$

A description of the interaction between argon atoms and the walls of the slit pore depends upon the nature, or model, of the walls. For example, if the walls are modelled as atomistically detailed graphene layers (that is, each individual atom of the wall is explicitly considered in the simulation), then the interaction with the walls will be the summation of all the pairwise interactions between each argon atom and those of the wall. For fully graphitic walls, taking this summation over infinitely long, and infinitely thick walls leads to an analytical expression known as the Steele potential:[44]

$$U_{sf}(z) = 2\pi\rho_s\varepsilon_{sf}\sigma_{sf}^2\Delta\left[\frac{2}{5}\left(\frac{\sigma_{sf}}{z}\right)^{10} - \left(\frac{\sigma_{sf}}{z}\right)^4 - \frac{\sigma_{sf}^4}{3\Delta\left(0.61+z\right)^3}\right] \tag{2.13}$$

Here ρ_s is the density of the solid, Δ is the distance separating the graphene layers of the walls and z is the perpendicular position of the molecule from the wall. The terms ε_{sf} and σ_{sf} are the combined values of ε and σ, as in Equation 2.11.

Our example system in Figure 2.1 uses a simple fluid that is represented by a single spherical interaction site. Complex fluids are made of several atoms, or interaction sites. These sites lead to additional contributions to the potential energy in order to account for the internal degrees of freedom within the molecule. These can include bond stretching, bond bending, proper and improper dihedral potentials, and so on (we will return to these terms later in the chapter). Finally, if the molecules or walls feature polar groups then long-range Couloumbic interactions should also be taken into account along with those from dispersion. This can be done via either

Ewald summation between partial charges, or some other appropriate method. The final potential energy of the system represents a sum of all these contributions, whereas the specific form and parameters of the individual terms comprise what is known as the molecular force field.

2.3 Grand Canonical Monte Carlo Simulations

2.3.1 Basic Principles

The partition functions outlined in Section 2.1 can rarely be estimated explicitly. An alternative way to estimate thermodynamic properties of a system is to generate a large sequence of microstates and average the desired property over all generated states, as stated in Equation 2.4. If the generation of these states follows the appropriate probability distribution then averaging over a large enough number of states will yield a close approximation to the true value of the thermodynamic property, with no need to calculate the partition function at all.

The generation of these states is the basic idea and essence of all molecular simulation methods. These simulations broadly fall into two categories: molecular dynamics (MD) and Monte Carlo (MC) methods. In molecular dynamics, the system advances in time by numerical integration of the equations of motion, according to the Newtonian mechanics. In this work the systems we are interested in are open, meaning that the number of particles is free to change. Such systems cause substantial technical difficulties for MD, and a more convenient method is a grand canonical Monte Carlo simulation.

Before we begin with Monte Carlo in the grand canonical ensemble, first let us consider a canonical system, (N, V, T), of some simple mono-atomic species. Thermodynamic properties could be estimated by randomly sampling from the possible microstates and summing the calculated property via Equation 2.4. However, the majority of these microstates would have very unfavourable interaction energies due to steric overlap of particles. The probability of observing these microstates is very low, and so (from Equation 2.4) the impact of these microstates will be very small. Because of this, random sampling of the microstates proves to be very inefficient.

The basic Monte Carlo scheme can be improved by biasing the sampling of microstates towards configurations that have a meaningful impact on the property average. Instead of accumulating configurations randomly and evaluating their probability-

weighed contribution to the desired property, we can accumulate configurations according to their Boltzmann probability and then take a simple arithmetic average. Such a process is called *importance sampling*, and a commonly used scheme is the Metropolis Monte Carlo method.[45] Within this scheme, the selection of microstates is carried out by comparing the existing configuration to that of a new *trial* state. The algorithm then determines if the new trial state should be accepted and used in the calculation of the average properties. The acceptance or rejection process is governed via a set of rules that ensure the detailed balance condition (see below), required for the Metropolis scheme, is upheld. Other conditions that the system must obey include being ergodic (every point in configurational space is accessible via a finite number of trials) and Markovian (the sequence of configuration states must form a Markov chain; i.e. the outcome of each trial depends only on the outcome of the trial that immediately preceded it).

Within the canonical ensemble, the initial configuration, o, has an associated probability density of being observed:

$$p_o = \frac{e^{-\beta U_o(\mathbf{r}_o)}}{Q(N,V,T)}$$

where $U_o(\mathbf{r}_o)$ is the potential energy of configuration o (for "old"), and $Q(N,V,T)$ is the canonical partition function. A trial configuration is generated by moving one of the particles in the system (commonly known as a translation move) to a new, random location. The new configuration, n (for "new"), occurs with a probability density:

$$p_n = \frac{e^{-\beta U_n(\mathbf{r}_n)}}{Q(N,V,T)}$$

The Metropolis scheme determines if the trial configuration is accepted or not. As mentioned earlier, one of the conditions of the Metropolis scheme is that the system maintains the detailed balance. This condition implies that at equilibrium, the probability of the system leaving state o must equal the probability of the system entering state o. In mathematical terms this principle, or condition, is formulated as:

$$p_o\,\pi(o \to n) = p_n\,\pi(n \to o) \tag{2.14}$$

where $\pi(o \to n)$ is the probability of state o transitioning to state n. This latter

property can be seen as a product of two stochastic events:

$$\pi(o \to n) = \alpha(o \to n)\, acc(o \to n) \tag{2.15}$$

where $\alpha(o \to n)$ is the probability of *creating* the trial configuration n from configuration o, and $acc(o \to n)$ is the probability of *accepting* such a move. With this in mind, Equation 2.14 then becomes:

$$p_o\, \alpha(o \to n)\, acc(o \to n) = p_n\, \alpha(n \to o)\, acc(n \to o) \tag{2.16}$$

According to the original Metropolis scheme[46] $\alpha(o \to n)$ is chosen to be equal to $\alpha(n \to o)$, although other conventions are possible. In more advanced Monte Carlo techniques it is often useful to bias the creation of a trial state in some way to increase simulation efficiency. In order to maintain the microscopic balance of Equation 2.14, the probability of accepting such a move must be adjusted to remove any bias. In this example, we adhere to the simpler case of $\alpha(o \to n) = \alpha(n \to o)$.

After rearrangement of Equation 2.16, the following expression is obtained:

$$\frac{acc(o \to n)}{acc(n \to o)} = \frac{p_n}{p_o} = e^{-\beta(U_n - U_o)} \tag{2.17}$$

This result is significant in that it shows how this Monte Carlo scheme does not require the calculation of the partition function, nor the explicit probability of each microstate. Instead, microstate generation is based on the ratio between the two microstate probabilities. There are many schemes that satisfy Equation 2.17. In the Metropolis scheme, the probability to accept a translation move is given by:

$$P_{acc(o \to n)} = \begin{cases} 1 & \text{if } U_n < U_o \\ e^{-\beta(U_n - U_o)} & \text{if } U_n > U_o \end{cases} \tag{2.18}$$

If the new configuration is more energetically favourable, then the transition is automatically accepted. If the new state is less energetically favourable, then the transition is accepted with a probability related to the energy difference between the old and new configurations: the less favourable the new energy is, the lower the probability of accepting, however such an acceptance remains possible. The algorithm for the Metropolis Monte Carlo scheme is shown as a flow diagram in Figure 2.2.

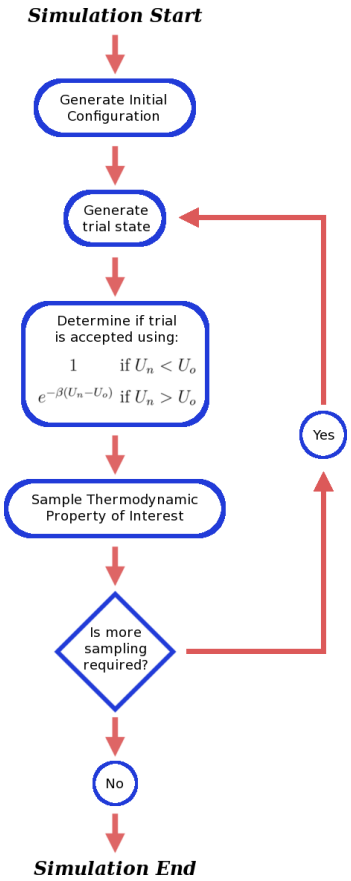

Figure 2.2: Flow chart showing the basic Monte Carlo algorithm.

For the grand canonical Monte Carlo procedure, fluctuations of the number of particles in the system must be accounted for. The starting point for this is the probability distribution of the ensemble, given by:

$$p\left(\mu, V, T\right) = \frac{e^{-\left(E_i/k_B T\right)}\, e^{\left(\mu N/k_B T\right)}}{\Theta\left(\mu, V, T\right)} \tag{2.19}$$

where $\Theta(\mu, V, T)$ is the grand canonical partition function, μ is the chemical potential of the adsorbing species, and T is temperature as usual.

In order to account for the possible fluctuations of particles, two additional trial moves are included: the creation of a particle within the system and the removal of an existing particle from the system. These two moves, along with the translation move, are shown schematically in Figure 2.3.

Using the same approach as for 2.18, but with the probability defined in Equation 2.19, acceptance criteria for deletion and creation of particles in the system can be

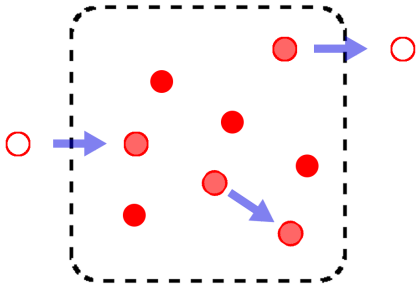

Figure 2.3: Trial moves in the grand canonical Monte Carlo simulation. These include: creation of a new molecule, translation (or rotation) of an existing molecule, or deletion of an existing molecule.

obtained. These acceptance criteria are now functions of temperature, interaction energy and volume of the system, but also chemical potential and current number of particles in the system. It is convenient to replace chemical potential with the fugacity, defined as:

$$\beta f = \frac{e^{\beta\mu}}{\Lambda^3} \tag{2.20}$$

which leads to the following acceptance criteria for insertion and deletion of a particle:

$$\begin{aligned} p_{acc(N\to N+1)} &= \min\left(1, \frac{\beta f V}{(N+1)} e^{-\beta(U_{N+1}-U_N)}\right) \\ p_{acc(N\to N-1)} &= \min\left(1, \frac{N}{\beta f V} e^{-\beta(U_{N-1}-U_N)}\right) \end{aligned} \tag{2.21}$$

The basic principles covered here set the foundation for all Monte Carlo simulations, however for complex systems more advanced variations of these methods are required to achieve the appropriate efficiency. The next section is dedicated to introducing such methods used in this work, including configurational and energy bias schemes.

2.3.2 Advanced Configurational Bias Monte Carlo

For complex molecules, the random insertion of a whole molecule becomes inefficient, in the sense that the insertion move is rarely accepted due to steric overlaps with the existing molecules or the pore walls. Over the years, a series of advanced methods

have been developed that circumvent this problem by following a scheme where a molecule is gradually grown into a position via several stages, thus effectively searching for the available space for a fragment of a molecule to be inserted. These methods are collectively known as the configurational bias Monte Carlo methods (CB-MC). While several variants of configurational bias Monte Carlo are available,[47–49] below we describe the most basic and general scheme outlined by Frenkel and Smit[45,50] and rooted in the original method by Rosenbluth and Rosenbluth.[51] This is followed by a few additional comments on the specific features of the CB-GCMC method, adopted in this thesis, and on our approach to handling the branched alkanes.

In this section we consider stage-by-stage trial insertion of a molecule of n-pentane and formulate acceptance criteria for CB-GCMC insertion, deletion and translation moves. The objective here is to illustrate the workings of the basic CB-GCMC scheme, while the proper justification of the method and other more fundamental issues are addressed in the original publications and molecular simulation textbooks.[45,47,51,52]

First, it is important to describe this molecule in accordance with some forcefield. In this work, we employ the TraPPE forcefield, based on the united atom representation of typical building blocks or groups constituting hydrocarbons. Specifically, each group of atoms, for example CH_3, CH_2, CH, etc., is represented with a single, parameterised interaction site according to this force field. Within TraPPE, a molecule of n-pentane consists of two termini CH_3 sites and three CH_2 sites, as shown in Figure 2.4.

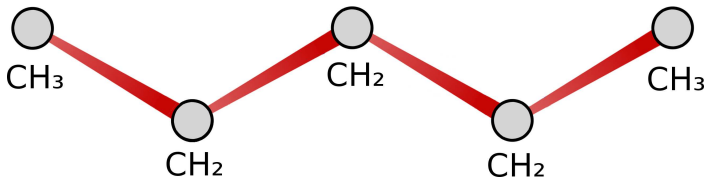

Figure 2.4: Representation of a normal pentane molecule within the TraPPE forcefield, made up of CH_3 and CH_2 interaction sites.

Early configurational bias Monte Carlo schemes were developed for linear molecules described within a united atom approach, such as pentane in the TraPPE representation. Branched alkanes as well as species in all-atom representation feature branching nodes, treatment of which requires more recent and advanced CB-GCMC methods.

As will become evident in due course, it is useful to separate the potential energy of interaction between this molecule and its environment into two components. The internal component, (u^{int}), is comprised of all the intramolecular energies with the molecule, such as bond stretching, bending and torsional terms. The external component, (u^{ext}), is comprised of all the intermolecular interactions that the molecule experiences within the system, including interaction with the walls and other molecules.

Let us consider the internal component, (u^{int}), in more detail. Within TraPPE the bonds between atoms are considered as rigid, with the bond length equal to 1.54 Å. Bond bending interaction involves three atoms within the chain. TraPPE uses a simple harmonic potential to describe this interaction:

$$u_{bend}(\theta) = \frac{k_\theta}{2}\left(\theta - \theta_0\right)^2 \tag{2.22}$$

where k_θ is the force constant, θ is the current bending angle and θ_0 is the equilibrium bending angle.[53–55] Every four atoms within a chain form a dihedral angle. Rotation of two termini sites within the set of four sites around the dihedral bond is described using the following torsional potential:

$$u_{torsion}(\phi) = c_0 + c_1\left[1 + \cos(\phi)\right] + c_2\left[1 - \cos(2\phi)\right] + c_3\left[1 + \cos(3\phi)\right] \tag{2.23}$$

where ϕ is the torsional angle, and c_1, c_2, c_3 and c_4 are the Fourier constants defined for each component, taken from the TraPPE forcefield.[53–55] In addition, united atom sites separated by four or more bonds also experience intramolecular Lennard-Jones interaction, according to Equation 2.11.

Consider now insertion of a single pentane molecule in the united atom representation. As the molecule consists of five united atoms, the insertion is accomplished in five steps or stages. Each stage is associated with a property called the *Rosenbluth weight*. The role of these weights will become clear as we progress with the insertion process and reach the final acceptance criteria.

The process starts with the first CH_3 site. This site is inserted randomly throughout the system (this is clearly not a very efficient approach for dense liquids and confined systems and we will revisit this issue in Section 2.3.3). The Rosenbluth weight is

calculated as:

$$w_{i=1} = k_1 e^{-\beta u^{\text{ext}}(\mathbf{r}_1)}$$

where $\mathbf{r}_1$ is the location of the first site. Here, k_1 here is an arbitrary constant and can be taken as 1.

In TraPPE, bond lengths are fixed and therefore the second site must be located on a sphere of radius r_0, equal to the bond length. This is where the biasing strategy comes into play for the first time. We are interested to find such a position on the surface of the sphere for the second site which does not lead to overlaps with other molecules or elements of the structure, and in general has favourable interactions with its environment. For this we probe several locations on the surface of the sphere as shown in Figure 2.5.

The Boltzmann factor $\left[e^{-\beta u^{\text{ext}}(\mathbf{r}_2)}\right]$ of each trial location on the sphere is calculated using the associated external energy interactions. A single trial location is selected with a probability:

$$p = \frac{e^{-\beta u^{\text{ext}}(\mathbf{r}_2)}}{w_2}$$

where $\mathbf{r}_n$ is the location of the chosen trial and w_i, the Rosenbluth weight, is defined as:

$$w_2 = \sum_{j=1}^{k_2} e^{-\beta u^{\text{ext}}(\mathbf{r}_2)}$$

and k_2 is the number of trials.

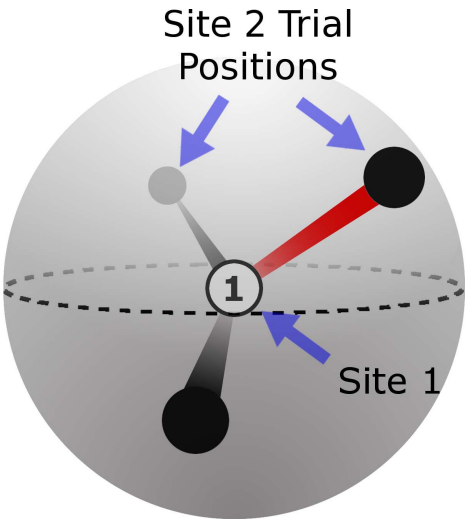

Figure 2.5: Representation of trial site locations for the placement of the second site during the growth of an alkane chain in configurational bias Monte Carlo. Trials are projected onto the surface of a sphere, originating from the position of the first site. No internal energy contributions are considered in the placement of the second site.

For the addition of the third united atom we need to consider two energy contributions: the bending potential associated with the angle formed by three atoms, and how the third atom interacts with its environment via non-bonded interactions. The bond bending potential is considered a hard degree of freedom, in that any deviation from the equilibrium value of the bond angle would lead to significant energy penalties. Therefore it makes sense to consider the insertion of the third atom in two stages as shown Figure 2.6. First we select the value of the bond angle with the probability:

$$p(\theta) = \frac{e^{-\beta u_{bend}(\theta)}}{C}$$

where the normalising coefficient C is of no consequence,[50] and $u_{bend}(\theta)$ is given by Equation 2.22. Once the angle has been selected and fixed, several trial locations of the site are probed, as shown in Figure 2.6. This placement step is often called disc-sampling, as the final positions of the trial sites are located on the rim of the cone, forming a disc shape. Again, the Boltzmann factor $\left[e^{-\beta u^{\text{ext}}(\mathbf{r}_3)}\right]$ of each trial location on the disc is calculated using the associated external energy interactions.

A single trial location is selected with a probability:

$$p = \frac{e^{-\beta u^{\text{ext}}(\mathbf{r}_3)}}{w_3}$$

where $\mathbf{r}_3$ is the location of the chosen trial, and w_3, the Rosenbluth weight, is defined as:

$$w_3 = \sum_{j=1}^{k_3} e^{-\beta u^{\text{ext}}(\mathbf{r}_3)}$$

and k_3 is the number of trials.

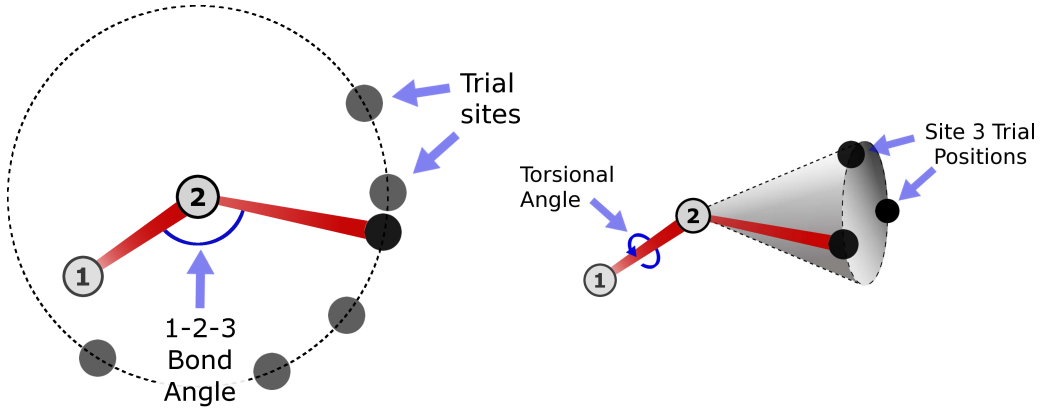

Figure 2.6: Two stage process for the placement of the third site during the growth of an alkane chain in configurational bias Monte Carlo. The first stage, shown on the left, involves the selection of the 1 - 2 - 3 bond bending angle, θ. Trial locations are placed on a 2D circle centred on the second site. The second stage, shown on the right, involves the selection of the axial rotation about the 1-2 bond ϕ. Trial locations are placed on the rim of a cone, projecting from the second site with the 1 - 2 - 3 bond angle θ. Note that for placement of the third site, the axial angle shown is for orientation only, there is no internal energy consideration associated with this bond.

Addition of the fourth site is similar to the addition of the third site. The process is again split into first selecting an angle formed by sites 2, 3 and 4, followed by testing trial locations projected onto the disc. Unlike the previous case of the third site, this case involves an additional energy term associated with the dihedral angle formed by atoms 1 and 4 around the bond connecting atoms 2 and 3. This energy term is small in magnitude compared to the bond angle and it is not necessary to consider selection of the dihedral angle in a separate stage. Instead this term is

incorporated into the $u^{\text{int}}(\mathbf{r}_4)$, recognizing that if a favourable location is found in terms of bond angle, it is unlikely to be rejected because of the torsional energy term. The Rosenbluth weight for this step is calculated similar to the expression for w_3 above.

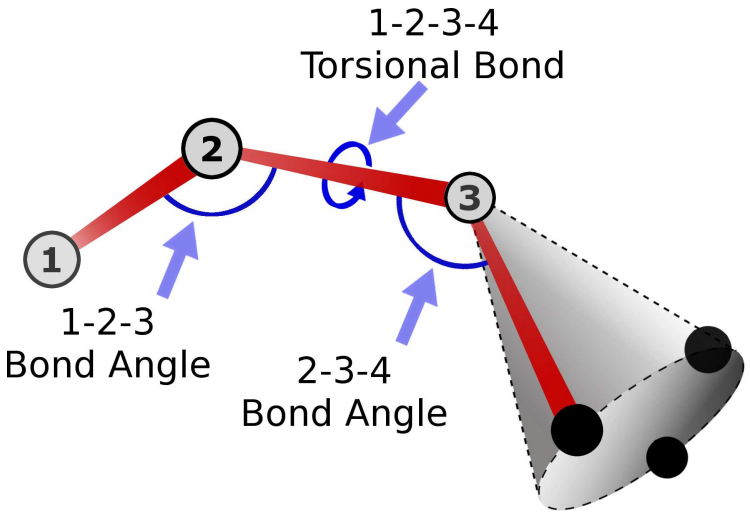

Figure 2.7: Representation of trial site locations for the placement of the fourth site during the growth of an alkane chain in configurational bias Monte Carlo. Axial rotation about the 2-3 bond cause the trial locations to be projected onto the rim of a cone, projecting from the third site. Internal energy considerations include both bond bending, as well as the torsional contribution around the 1-2-3-4 bond.

Addition of the fifth site is in turn similar to the addition of the fourth, with the only difference being that the $u^{\text{ext}}(\mathbf{r}_5)$ now involves intermolecular interaction with the other molecules and adsorbent as before, plus dispersion interaction between sites 1 and 5. Figure 2.8 shows how two configurations with similar internal bending energies can have very different intramolecular interactions. On the left the configuration shows that the two ends of the molecule are much closer (and so with stronger interactions) than the configuration on the right. The indicated arrow shows how a change in the torsion of such a bond can change the intramolecular interaction by changing the distance. Within TraPPE forcefield[53] intramolecular dispersion interactions are modelled via the 12-6 Lennard-Jones potential (Equation 2.11) for interaction sites separated by 4 bonds and above. For longer alkanes the process is repeated in the same fashion as for site 5.

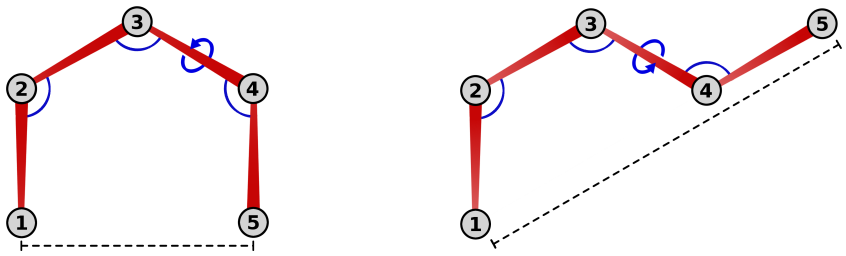

Figure 2.8: Example of two n-pentane configurations with similar internal bending energies, but different intramolecular dispersion interactions. In n-pentane, intramolecular forces arise between the first and last sites. As shown by the dashed lines, these sites are much further apart in the conformation on the right and so have weaker intramolecular interaction.

Once all the sites are placed, the complete Rosenbluth factor of the whole chain is calculated using:

$$W^{\text{ext}}(n) = \prod_{i=1}^{l} \frac{w_i}{k_i}$$

The Rosenbluth factor of the new conformation is compared to that of the old molecule, which is calculated in a similar way except one of the trial locations chosen for each site is given by the actual location of the molecule. In the translation and deletion moves, we also need to calculate the Rosenbluth factor of the current selected chain conformation. For this we pretend to grow a chain into its existing conformation using the procedure described above, with the resulting (old) Rosenbluth factor:

$$W^{\text{ext}}(o) = \prod_{i=1}^{l} \frac{w_i}{k_i}$$

The acceptance criteria for translation, insertion and deletion moves must correctly reflect the bias, introduced at every stage of the process, and this is where the role of the Rosenbluth factors becomes apparent, with the final expressions being:

$$\begin{aligned} p_{acc(o\to n)} &= \min\left(1, \frac{W^{\text{ext}}(n)}{W^{\text{ext}}(o)}\right) \\ p_{acc(N\to N+1)} &= \min\left(1, \frac{V\beta f}{(N+1)} \frac{W^{\text{ext}}(n)}{W^{\text{ext}}_{IG}}\right) \\ p_{acc(N\to N-1)} &= \min\left(1, \frac{N}{V\beta f} \frac{W^{\text{ext}}_{IG}}{W^{\text{ext}}(o)}\right) \end{aligned} \tag{2.24}$$

Here, W^{ext}_{IG} is the Rosenbluth factor for the ideal gas of alkane molecules. It can

be obtained via the same procedure as described before. In this case, however, the only energy contributions arise from the intramolecular energy terms, with $u^{\text{ext}}(\mathbf{r})$ having contributions from the intramolecular dispersion interactions only. The W_{IG}^{ext} is required to correctly convert the chemical potential of the system of ideal chains (alkane chains featuring no intramolecular dispersion interactions) to fugacity, consistent with the experimental measurements. A variant of the translation move is a cut-and-regrowth move where a portion of a chain is removed and regrown, with the partial Rosenbluth factor accumulated only for the portion of the chain in question. This has been shown to improve efficiency of the Monte-Carlo sampling, particularly for longer alkanes.[50,56]

2.3.3 Combined Configurational Bias and Energy Bias Methods

A way to further increase simulation efficiency is the energy-bias method, proposed by Snurr and co-workers.[57] Conventional GCMC methods randomly sample the system volume when attempting to insert a molecule (or the first site in CB-GCMC, as described above). In dense systems, such as liquids, or in porous systems, where a substantial proportion of the volume is occupied by the solid structure itself, the fraction of accepted insertion trials tends to be very low due to the high proportion of energetically unfavourable locations.

The energy bias method seeks to increase simulation efficiency by focusing the attempted insertion trials on the energetically favourable regions. For this the simulation volume is split into a number of small cubic elements, V_n. A preliminary simulation determines the interaction of some probe molecule (depending on the species) with the adsorbent by placing the probe molecule in the centre of each cubelet. Location of the position for the trial insertion is then selected from the cubelets according to a weight assigned to each cubelet:

$$\rho_i = \frac{e^{-\beta U_{V=i}}}{\sum_{j=1}^{V_n} e^{-\beta U_{V=j}}} \tag{2.25}$$

where the sum in the denominator is the sum over all cubelets and $\beta = 1/k_B T$ as usual. This effectively eliminates attempts to insert the molecule into locations occupied by atoms of the adsorbent. Of course, biasing the insertion moves in this way must

be counter-balanced by altering the acceptance rules for insertions and deletions to maintain detailed balance, so that the ensemble is sampled correctly. In this thesis we use a combination of the energy bias method by Snurr et al. and configurational bias method by Macedonia and Maginn[49] as implemented in Multipurpose Simulation Code, MuSiC.[58]

2.3.4 Branched Alkanes

A number of methods have been proposed, extending CB-GCMC methods as described above to branched alkanes (or alkanes in fully atomistic representations). For example, Macedonia and Maginn proposed to use an additional simulation to generate a large library of fragments, associated with each branching point.[49] The CB-GCMC scheme in this case involves stage-by-stage assembly of the branched fragments with their mutual orientation sampled in the same way as in the CB-GCMC process above to obtain the associated Rosenbluth factor. In case of i-butane, this simply reduces to an insertion of a whole molecule from the library of conformers. Furthermore, i-octane, one of the primary species of interest in this thesis, can be seen as an assembly of two branched fragments, requiring two additional simulations for each fragment. Therefore, we use a simplified approach, where branched alkane molecules are inserted as rigid structures, selected from a library of conformations, corresponding to the canonical distribution at a particular temperature. As has been shown in our previous publication[59] this approach is as accurate as CB/EB GCMC for i-octane.

2.4 Predictive Molecular Models for Adsorption in Carbon Materials

So far we have described the methods and tools required to simulate an adsorption isotherm in a slit pore of a given geometry. There is still a considerable gap between these types of simulations and a predictive model for the adsorption in a real porous material. In this section we describe a general approach, adopted in this thesis.

In general, interest in the characterisation of porous adsorbents was sparked by their widespread use in various industrial applications such as gas separation, purification and reaction processes.[29,60,61] Of a particular importance, and a key element

of this thesis, is the size and frequency of the pores found in the porous material. This property is known as the pore size distribution (PSD). For crystalline or ordered porous materials (such as MCM - 41), information on pore sizes within the material can be obtained via a number of alternative techniques, including X-ray crystallography (simply giving the explicit structure of the crystal and, hence, pores) and transmission electron microscopy (TEM). For disordered materials, direct observation of their porous structure is not possible. A common technique to obtain this information is physical adsorption of nitrogen at 77 K (although argon at 87 K and carbon dioxide at 278 K are also used). The key idea behind the methods based on the physical adsorption of gases is that thermophysical properties of confined fluids, such as the pressure at which the adsorbed fluid undergoes capillary condensation, depend on the degree of the confinement, or in other words, on the size of the pore within which the fluid is located. From this perspective, an adsorption isotherm contains, in an encoded form, information about the collective behaviour of all pores in the system. Thus, to extract the information on the PSD from an adsorption isotherm requires some interpretation.

Over the last hundred years, since the pioneering work of Langmuir, a number of theories or methods have been developed to provide this interpretation, including Langmuir, Brunauer–Emmett–Teller and Freundlich isotherms, Dubinin-Radushkevich and other approaches.[62,63] However, these methods have well known limitations extensively covered in the literature.[29,38,62–64] Modern statistical mechanical approaches, in the form of density functional theory and molecular simulations, offer an alternative route to characterisation of porous materials based on physical adsorption.[25] Here we consider one of these more modern approaches in application to adsorption in activated carbons. At the heart of this approach, developed via a number of contributors over the years,[22,34] is an assumption that the structure of an activated carbon can be considered as a collection of independent slit pores, the walls of which are made out of graphite. In this situation, it follows that adsorption in the whole material must be a composite result of adsorption in individual pores. The link between adsorption in the whole sample and adsorption in individual pores is then established through the so-called Adsorption Integral Equation (AIE):

$$N\left(P_i\right) = \int_0^\infty \rho\left(w, P_i\right) f\left(w\right)\, dw \tag{2.26}$$

where $N\left(P_i\right)$ is the adsorbed loading at a given pressure P_i, $\rho\left(w, P_i\right)$ is the density of

loading in a pore of width w, at pressure P_i, and $f(w)$ is the Pore Size Distribution as a function of pore width, w.

Construction and use of the predictive models based on these ideas is depicted schematically in Figure 2.9. It consists of the following steps. First, an experimental adsorption isotherm is obtained for the porous material in question (panel A). Next, a kernel of adsorption isotherms is generated for pores of different widths (panel B), using GCMC methods, or for simpler species, density functional theory. The final stage is the solving of the AIE to obtain the PSD (panel D). Once the PSD is known, the model can be used in the predictive mode. In this situation, we are interested in adsorption at other conditions, adsorption of other species, or adsorption of mixtures of species. For this, a new kernel of adsorption isotherms is generated for the new conditions of interest. This kernel of isotherms, in combination with the PSD, is used to obtain the composite adsorption isotherm (panel C in Figure 2.9), according to the AIE.

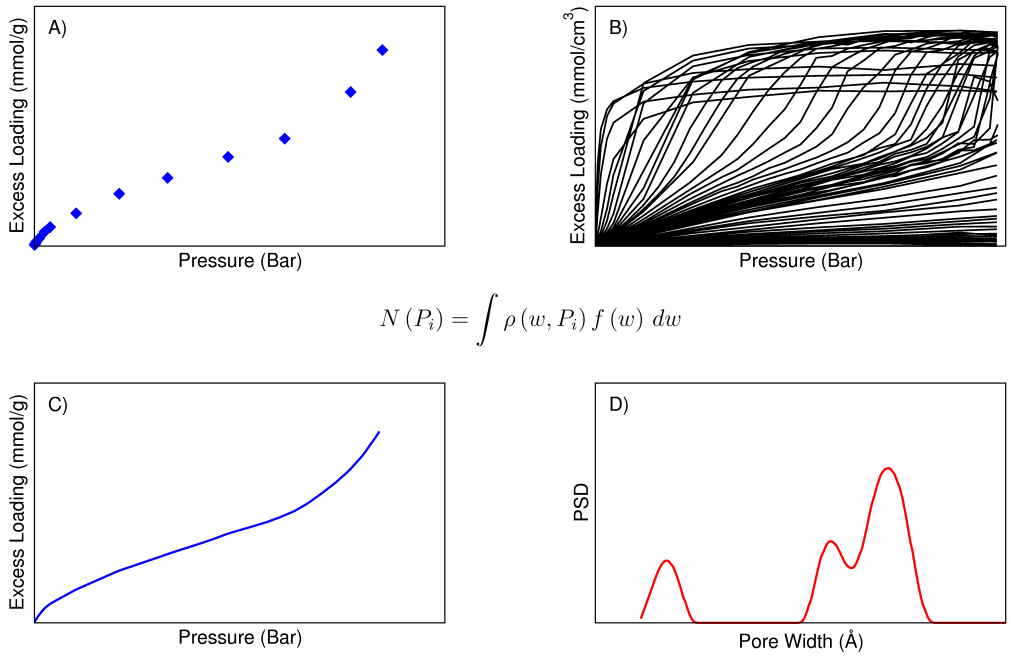

Figure 2.9: A schematic diagram showing the necessary elements and steps in the construction of predictive adsorption model. The AIE is shown in the centre (Equation 2.26). A) shows an experimental isotherm, B) shows an adsorption kernel for conditions identical to the experimental isotherm, D) shows the pore size distribution, and C) represents a predicted adsorption isotherm.

Although elegant in principle, the solution of the AIE faces a number of technical challenges. The AIE corresponds to a Fredholm integral equation of the first kind,[65] commonly known to be both an ill-posed and ill-conditioned problem.[23,26,31,32,66] This leads to either no solution or to an infinite number of possible solutions which in turn are extremely sensitive to small changes in the input.

Several alternative strategies have been proposed to obtain the PSD. One class of these strategies simply tries to find an analytical form of PSD with the best fit to the AIE and experimental data. For example, Sweatman and co-workers[34] employed a sum of log-normal functions, each with three free parameters, and used a simulated annealing scheme to converge to the most appropriate PSD by minimising the errors between the fit isotherm and the experimental data. Similar methods were used by Lastoskie et al.,[29] Sosin and Quinn[66] and Scaife et al.[67] These methods require an initial guess on the functional form of the PSD, before characterisation has taken place. An alternative protocol adopts a matrix-based approach based on a discretised representation of the PSD. Works such as those by Figueroa-Gerstenmaier and co-workers,[23] Gusev et al[32] and Ravikovitch et al.[26] adopt this approach. Here we outline the methodology following that of Davies and Seaton.[41–43,68]

In this protocol the range of pores is split into quadrature intervals, $\hat{w}_j$. The discrete from of the AIE becomes:

$$N\left(P_i\right) \approx \sum_{j=1}^{m} \rho\left(\hat{w}_j, P_i\right) f\left(\hat{w}_j\right)\, \delta\hat{w}_j \tag{2.27}$$

where δw_j is the quadrature interval that the discretised pore range has been split into, m is the total number of quadratures and $\hat{w}_j$ is the average pore size of each quadrature interval. In a more compact matrix notation, this equation becomes:

$$\mathbf{N} = \mathbf{AWf} \tag{2.28}$$

$$\begin{array}{rrcl} \text{where:} & \mathbf{N} & = & N\left(P_i\right) \\ & \mathbf{A} & = & \rho\left(\hat{w}_j, P_i\right) \\ & \mathbf{W} & = & \mathrm{diag}\left(\delta\hat{w}_j\right) \\ & \mathbf{f} & = & f\left(\hat{w}_j\right) \end{array}$$

Equation 2.28 can in turn be written as:

$$\mathbf{N} = \mathbf{Af}^{*} \tag{2.29}$$

$$\text{where: } \mathbf{f}^* = \mathbf{W}\mathbf{f}$$
$$\mathbf{f} = \mathbf{W}^{-1}\mathbf{f}^*$$

This formulation of the AIE inversion problem makes it possible to use matrix methods to find the PSD. Several scenarios are possible, depending on the number of experimental data points, n, and the number of quadratures used, m.

1. $n > m$ The problem is over specified, and the best solution determined through least-squares methods
2. $n = m$ If a solution exists, it will be unique and can be determined through regularisation procedures
3. $n < m$ There is either no solution, or an infinite number of solutions

Case 1 is unlikely to occur as acquiring sufficiently resolved experimental data is usually more difficult than generating simulation isotherms. In case 3, solving Equation 2.29 leads to multiple solutions (if a solution exists at all), a result of the ill-posed nature of the AIE equation.[41,42] It is quite possible that these solutions are significantly different from each other leading to the conundrum of determining which PSD is the most realistic.[41,42] In case when $n = m$ (Case 2), stabilisation methods can be applied leading to a unique solution corresponding to the most representative PSD. In some situations, even under $n < m$ condition, increasing the number of quadratures cannot yield a solution to Equation 2.29, indicating a failure of the model to accurately capture the adsorption properties of the material.[33]

Therefore, finding a PSD satisfying the AIE is split into a two tier problem. First, we are interested in establishing whether any feasible pore size distribution exists; second, given that a feasible pore size distribution is possible, we are interested in finding the representative (i.e. most realistic) PSD. The first problem is addressed by considering the number of quadrature intervals larger than the number of data points: $n < m$. The solution to Equation 2.29, and so the existence of a PSD, can be determined by using minimisation techniques, attempting to reduce the following residual to an acceptable tolerance:

$$R = \sum_{i=1}^{n} \left[N(P_i) - \sum_{j=1}^{m} \rho(\hat{w}_j, P_i)\, f(\hat{w}_j)\, \delta\hat{w}_j \right]^2 \tag{2.30}$$

If the minimisation method is unable to reduce R to the desired level, then no PSD solution exists that can be fitted to the available data. If it is successfully

reduced, then an infinite number of solutions exist.

As argued by Davies and Seaton, for the most representative PSD, the number of quadratures m should be equal to the number of data points n. Therefore, once it is established that a feasible PSD does exists, we need to revisit Equation 2.30 with the condition: $n = m$. In practice, under the $n = m$ condition, it is unlikely to obtain a solution to Equation 2.30; in other words it is unlikely to find a combination of m pores which can precisely capture the experimental behaviour in all n pressure points. In a number of studies it was proposed to alleviate this problem by incorporating regularisation methods.[69,70] Specifically, in regularisation methods an additional constraint is introduced representing some measure of the PSD smoothness. A common choice of this constraint is the square of the second derivative of the PSD. An approximate solution to the Equation $\mathbf{N} = \mathbf{AWf}$ is then found through the minimisation of the following residual:

$$R = \sum_{i=1}^{n} \left[N\left(P_i\right) - \sum_{j=1}^{m} \rho\left(\hat{w}_j, P_i\right) f\left(\hat{w}_j\right) \, \delta\hat{w}_j \right]^2 + \alpha \sum_{j=1}^{m} f''\left(\hat{w}_j\right)^2 \delta w_j \tag{2.31}$$

Here α is some non-negative smoothing parameter, with the remainder being the function representing the smoothness of the PSD.

With the new objective function defined, the most representative PSD solution can be obtained for a specific value of the smoothing parameter. The problem is now to optimise the value of the smoothing parameter. Clearly, for the predictive adsorption models, the most appropriate value of smoothing should be selected based on the minimisation of the differences between the reference experimental data and the fitted simulation isotherm. Here we employ two specific methods for systematic search for the best value of the smoothing parameter, and hence the most representative PSD.

The first is the L-Curve method. This method plots the error of the fit (to the reference data) against smoothing parameter using Equation 2.32, an example of which is plotted in Figure 2.10. In practice this error remains fairly constant as the smoothing parameter is increased. At some threshold the error increases dramatically, leading to an "L" shape in the curve. The optimal smoothing parameter is commonly taken to be the parameter immediately prior to this steep ascent.

$$E(\alpha) = \frac{1}{n}\sum_{i=1}^{n}\left[N(P_i) - \sum_{j=1}^{m}\rho(\hat{w}_j, P_i)\, f(\hat{w}_j)\, \delta\hat{w}_j\right]^2 \tag{2.32}$$

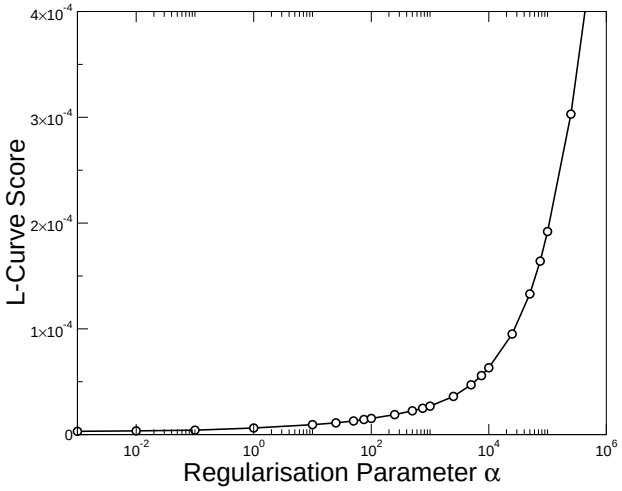

Figure 2.10: Typical L-Curve for the characterisation of a combustion chamber deposit sample taken from this work. Shape and scale are similar to those found in the literature.[17,71,72]

The second method is the Generalised Cross Validation (GCV) method. The assumption behind the GCV is that within any experimental data set, n, a good choice of smoothing parameter should allow the prediction of any individual data point from a PSD that is generated using the remaining $n-1$ points. This method assigns each smoothing parameter a GCV score based on how accurately these predictions match the reference data points. The parameter with the lowest score is determined to be the most optimal. Figure 2.11 shows an example GCV curve used in this work.

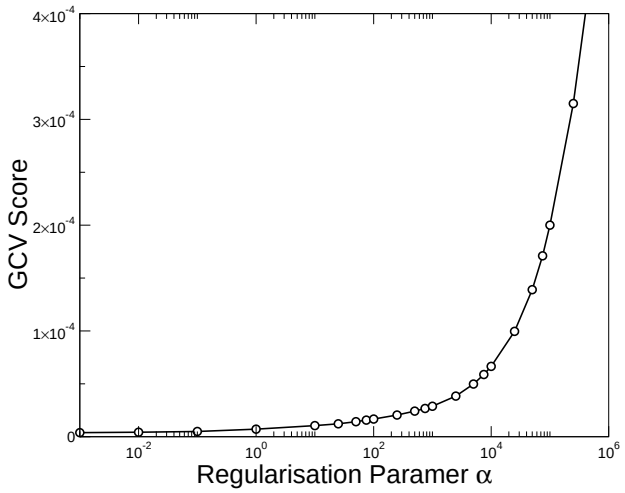

Figure 2.11: Typical GCV Curve for the characterisation of a combustion chamber deposit sample taken from this work. Shape and scale are similar to those found in the literature.[17,71,72]

The choice of smoothing parameter is occasionally somewhat subjective and often requires cross-comparison between the above two methods and visualisations of the corresponding PSDs. A selection of smoothing parameters deemed acceptable via the GCV and L-Curve methods are gathered and any unrealistic PSDs are eliminated. These might include PSDs with very narrow or jagged peaks.

2.5 Summary

In this chapter we introduced the necessary foundations behind the models and methods employed in this thesis, including a statistical thermodynamic background, a general approach to the molecular forcefield, and the simulation methods used. A general approach to the characterisation of porous materials was also given. Specific details of the parameters of the models and simulations, as well as additional, more specialised methods will be introduced as necessary in the next chapters.

Chapter 3

Review of the Recent Studies of Adsorption in Engine Deposits using Predictive Molecular Models

3.1 Introduction

The work presented in this thesis continues an going collaboration between Shell Global Solutions and Sarkisov's group at the University of Edinburgh, started in 2006. The general objective of this collaboration is to understand the structure of engine deposits (and in particular their porosity) and to what extent they can adsorb hydrocarbon components of the fuel. The basic idea is to use the available experimental data and modern molecular simulation methods to construct predictive models of adsorption in engine deposits. This allows one to consider chemical species representative of fuel blends under conditions relevant to the engine operation. Despite the important implications for the automotive industry, in 2006 this area of research was, and still is, a largely uncharted territory, with the publications from Sarkisov's group being the only existing publications on hydrocarbon adsorption in engine deposits. The pioneering contributions to this field were made by Dr. Pinto da Costa, in his 2009 PhD thesis titled "Structural Characterization of Carbonaceous Engine Deposits". There it was realised that the construction of the predictive models for carbonaceous deposits could be based on the strategy previously developed by Seaton and co-workers for predictive models of adsorption in activated carbons.

Although this idea was simple and elegant in principle, its development encountered a number of technical challenges, and also illuminated future research directions in this area, including the remit of this thesis. It is therefore instructive to review the original studies of Costa and co-workers, their findings and limitations, and based on these foundations formulate the specific original contribution of the current work.

3.2 Structural Characterisation of Engine Deposits and the Predictive Model Development

Prior to the studies of Costa et al,[39,40] little was known about the adsorption interactions of engine deposits with fuel components. A number of publications agreed that engine deposits decreased engine performance, and there was a general consensus that adsorption must be an important contribution to this process.[4,11–13] However, the work by Costa and co-workers was the first attempt to quantitatively examine this hypothesis and the extent of adsorption of fuel components in the deposits. For reasons outlined in Chapter 1 (see Section 1.3.3), an experimental approach to this investigation was considered infeasible. Instead, molecular modelling techniques were used to predict the adsorption behaviour of engine deposits at conditions of interest. For this Costa and co-workers adopted an approach previously developed for predictive adsorption studies in activated carbons. This approach has been described in Chapter 2. Briefly, within this approach the structure of the porous material is treated as a collection of independent slit pores. The frequency with which pores of different widths are represented in the sample of material is called a Pore Size Distribution (PSD). The first step of this approach aims to obtain this PSD. For this an adsorption isotherm is measured on a real sample, molecular simulations are used to generate adsorption isotherms in individual slit pores for the same adsorbate and at the same temperature, and the Adsorption Integral Equation (AIE) is solved to obtain the PSD. Various techniques described in Chapter 2 are applied to generate the most accurate PSD (in other words, the PSD providing the most accurate and robust predictions). In the second step of the approach, molecular simulations are employed to generate adsorption isotherms in individual slit pores for the other species of interest, at other conditions, or mixtures, and the PSD in combination with

AIE is applied to generate a predicted adsorption isotherm for the actual sample of the material.

With this approach in mind, the objectives of the studies by Costa and co-workers were threefold:

1. to develop a molecular model capable of describing adsorption behaviour of engine deposits
2. to use this model to characterise the structure of selected engine deposits
3. to use both the developed model and the information on deposit structure to predict adsorption behaviour of representative fuel components in engine deposits.

In the original work, investigations were concentrated on two main samples of engine deposit. The first was a sample of CCD generated in a bench mounted spark-ignition engine operating under simulated urban conditions, and the second was a sample of IVD taken from the engine of a Ford Fiesta, a four-cylinder 1.2 L spark-ignition model. These samples were subjected to elemental and thermal gravimetric analysis. The elemental analysis (tables 1.1 and 1.2, in Chapter 1) demonstrated that although carbon was present in the deposits in significant amounts, other elements such as oxygen, hydrogen, zinc and calcium also constituted a substantial proportion of the elemental composition. The presence of zinc and calcium in particular indicate the contribution of lubricating oils in the formation of the deposits. Furthermore, samples differed from each other in the elemental composition, implicating an important role of the location where they form and conditions.

The sample of CCD, generated in a bench-mounted engine, was originally formed by mixing two deposits collected from the piston top and the cylinder head. Before these were mixed, thermal gravimetric analysis (TGA) was performed on each sample, the results of which are reproduced from the original thesis of Dr. Costa,[17] along with TGA results for the IVD, in Figure 3.1. During this procedure, the temperature was linearly increased at a rate of 5 K/min from 300 K to 840 K. The red lines correspond to the two CCD samples, circles correspond to the cylinder head deposits, and diamonds correspond to the piston top deposits. The blue line shows the TGA results for the intake valve deposit. Results show that all samples are stable and retain at least 95% of the original mass at 500 K, at which point the piston top deposit and IVD began to degrade rapidly. The behaviour of these two

deposits is very similar. At 650 K they both have around 80% of the original mass, and this degrades down to 50-55% at 800 K. The cylinder head deposit follow the same behaviour, but the degradation occurs at a higher temperature. At 650 K the cylinder head deposit is still at 92% of the original mass, and this drops to 65% at 800 K. This difference is thought to be related to the difference in composition of the deposits, which in turn results from a higher temperature profile for the cylinder head compared to that of the piston top.

Mass spectrometry of the two CCD samples was performed during the TGA process, and shows the breakdown of the carbon framework at around 700 K. The results of the samples are very similar, and so only the results for the piston top deposit are shown. These results, reproduced from the thesis of Dr. Costa,[17] are found in Figure 3.2. The graph shows that before 420 K only water is desorbed from the sample, while CO_2 and CO begin to desorb after 550 K, indicating the degradation of the carbon structure. The data from the TGA outlined the appropriate degassing and sample activation regimes for the consequent adsorption studies.

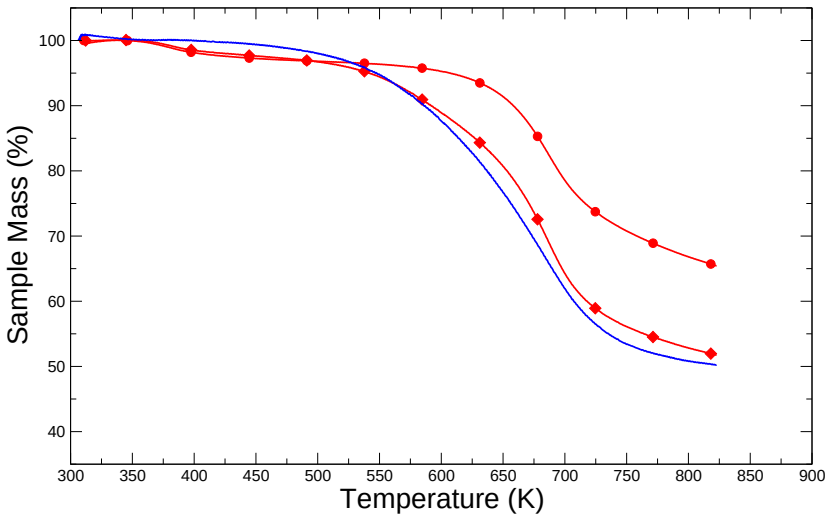

Figure 3.1: Thermogravimetric analysis for cylinder head (red line with red circles), piston top (red line with red diamonds) and intake valve (blue line) deposits**.** Reproduced from Costa.[17]

The next phase of the work was associated with collecting the necessary experimental data and obtaining the PSD for the samples. Ethane was chosen as a probe adsorbate. It is gas under conditions of interest and at the same time, being a

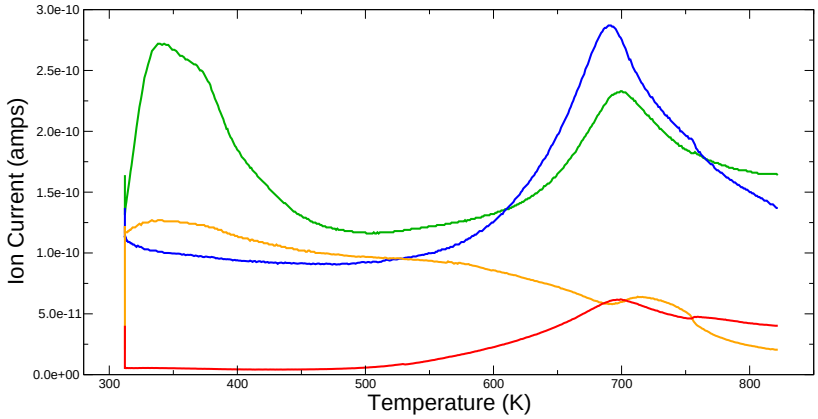

Figure 3.2: Mass spectrometry results following thermogravimetric analysis of CCD (piston top). Components emitted, and the corresponding atomic mass, include: water, 18 (green line); carbon monoxide, 28 (blue line); oxygen, 32 (orange line); and carbon dioxide, 44 (red line). Reproduced from Costa.[17]

member of the hydrocarbon family, it must possess some chemical properties characteristic for the whole alkane family, including the chosen fuel components. It is also worthwhile to note that attempts to measure nitrogen adsorption at 77 K (see Figure 1.6) and CO_2 adsorption at 278 K were made, but abandoned due to very long equilibration times per point and low reproducibility. While the diffusion-limited nature of the nitrogen adsorption, leading to long equilibration times, agrees with the findings of Zerda et al,[2] attempts to reproduce the carbon dioxide results by Zerda et al failed. Carbon dioxide isotherms were found to be irreversible, with substantial hysteresis failing to close.

In contrast, ethane adsorption isotherms at 278 K were found to be reproducible and exhibited no hysteresis loop. For molecular simulations, ethane was described using the TraPPE potential,[53] while the slit pore model was based on the well-known Steele potential with the parameters taken from the literature, corresponding to activated carbons.[44] The original model contained slit pores from the microporous region only (less than 20 Å). This was justified based on the work of Zerda et al. who reported micro-pores as the most dominant pore size found in CCDs.[2]

Figure 3.3 on the left shows the comparison between the experimental data (blue diamonds) and the simulated isotherm obtained from the original microporous model. It is clear that this fitted isotherm, based on the best estimate of the PSD, was in poor agreement with the experimental data. It was speculated that this failure was

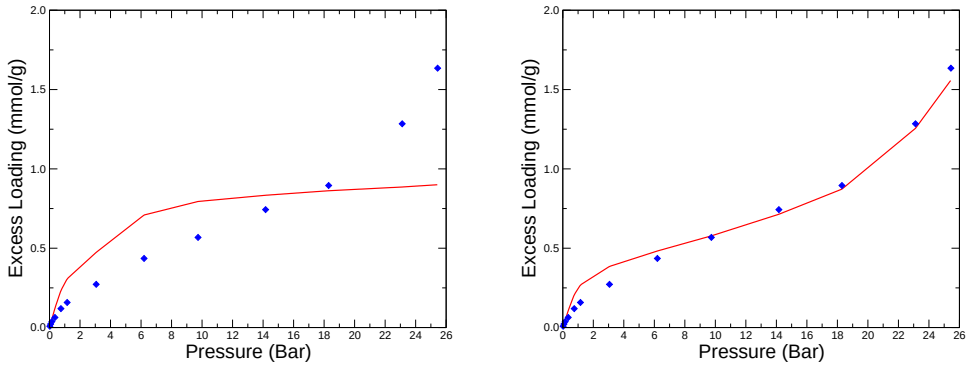

Figure 3.3: Comparison of experimental (solid blue diamonds) and simulated (red line) adsorption isotherms for ethane on CCD at 278 K. Predictions from adsorption kernels containing exclusively micropores (left) and both micro and mesopores (right).

a result of significant differences in properties between the typical activated carbons and the engine deposits, particularly in density, composition of the materials and features of the PSD. As an initial attempt to improve the model, a much broader range of pores was considered by including the mesoporous region (greater than 20 Å). We note here that the analysis of the window of reliability was not performed on this broader range at the time. Figure 3.3 on the right shows the comparison between this new model and the reference experimental results. The shape of the experimental isotherm was reproduced much better with this model. However, even when the mesopore range was included, there were still some noticeable differences at lower pressures. Adsorption in this pressure range is dominated by interactions between the solid structure and adsorbing fluid. A lack of agreement here indicated that the parameters of solid-fluid interactions, based on activated carbon models, were not appropriate for engine deposits. This is not surprising given the large differences in elemental composition between activated carbon and engine deposits, with tables 1.1 and 1.2 (see Chapter 1) showing that deposits are only between 65 and 75 % carbon. Hence, there was a need to adjust the potential well depth of the solid-fluid interactions to take into account this compositional difference.

In the original studies of Costa and co-workers, the well-depth of the potential associated with the atoms of the slit-pore walls was treated as an additional optimisation parameter.[39] Assuming a homogeneous distribution of elements within the

deposit, it was anticipated that the effective potential well depth should be larger for engine deposits than that for activated carbons due to the presence of elements such as zinc, calcium, phosphorous etc. However, the best agreement between simulation and experimental data was obtained using a smaller value of the solid-fluid well depth parameter compared to a common value for activated carbons. This could indicate the inhomogeneous nature of the engine deposits; if the majority of non-carbon elements are not close to the solid surface they would have a reduced impact on adsorption properties. It could also indicate that the higher interaction strength from non-carbon elements is off-set by the lower density of the engine deposits compared to standard activated carbons, such as BPL. In principle, both the density of the material and the parameters of the solid-fluid could be treated as independent optimisation parameters. However, the investigation of Costa and co-workers focused only on the parameters of the solid-fluid interactions, which effectively incorporated all other deviations of the engine deposits from activated carbons, not captured in the wider pore range. A preliminary study within this thesis work also considered alternative values for both the density of the materials and solid-fluid interaction parameters, and arrived to the same combination of parameters and properties, as in the original study by Costa and co-workers. Hence, this set of parameters is adopted throughout this thesis.

Results from the new model, with a wider range of pores and optimised solid-fluid interactions, for ethane at 278 K on CCD are shown on the left-hand side of Figure 3.4. A better fit at low pressures (compared to Figure 3.3) indicates a more appropriate interaction potential (in combination with the specific PSD).

The pore size distribution obtained for this structure is shown in Figure 3.5, the left-hand side graph shows the full range of pores, while graph on the right shows a more detailed picture of the pores below 60 Å. The CCD structure shows four major peaks indicating pores around 10, 45, 140 and 440 Å. Peaks in the micro and lower mesoporous regions are typical of activated carbons and are of primary interest as the larger pores tend not to influence adsorption significantly (in other words, the 440 Å should be beyond the window of reliability as introduced by Gusev and co-workers,[33] this is discussed in more detail in Chapter 5). The robustness of the model was examined by predicting adsorption of the same species (ethane) at other conditions. The right-hand side of Figure 3.4 shows both the simulated and experimental adsorption data for ethane on CCD at 298 K. The experimental data for this system is shown as blue diamonds, while the red line indicates the

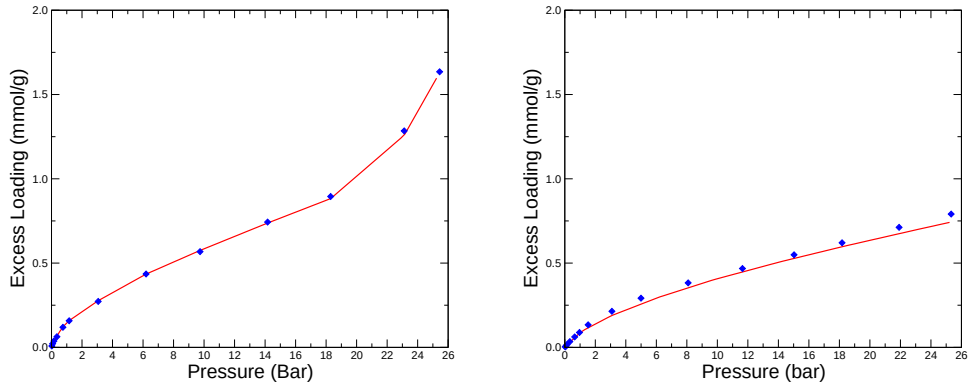

Figure 3.4: Comparison of experimental (solid blue diamonds) and simulated (red line) adsorption isotherms for ethane on CCD at 278 K (left) and at 298 K (right).

simulated isotherm. From this figure, the model is able to accurately reproduce the experimental results.

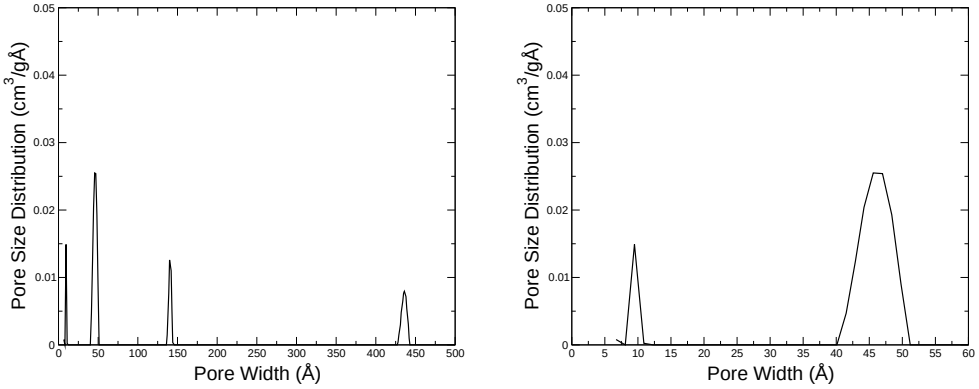

Figure 3.5: Pore size distribution for CCD . The full spectrum is shown on the left, while the right panel shows only the micro- and lower mesoporous range.

The next stage in model validation was to test the transferability of parameters between different types and samples of engine deposits, given that deposits generally differ from each other in structure and composition. For this a sample of IVD was considered without any modifications of the solid-fluid interaction parameters, obtained for CCD and using CCD experimental data. A new PSD was generated for the IVD sample, using experimental data on ethane adsorption in the sample at

278 K. Figure 3.6 shows comparisons between the experimental results and predicted adsorption isotherms for ethane at 278 K and 293 K. The isotherms in Figure 3.6 show a very good match between experiments and simulations. This indicates that the interaction parameters of engine deposits, developed using only the CCD, are also applicable to IVDs. It is quite surprising to observe such a good transferability of the model between different types of engine deposits given their compositional differences. This could be associated with the PSD of the materials acting as a fitting parameter and mitigating these differences.

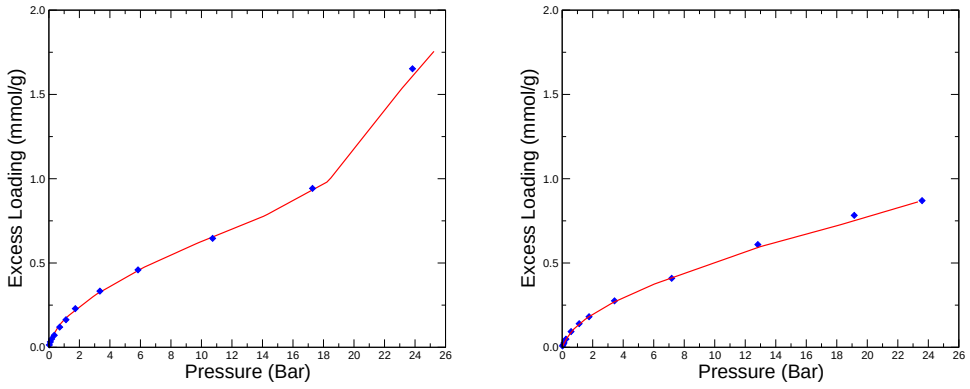

Figure 3.6: Comparison of the experimental (solid blue diamonds) and simulated (red line) adsorption isotherms for ethane on IVD at 278 K (left) and 293 K (right).

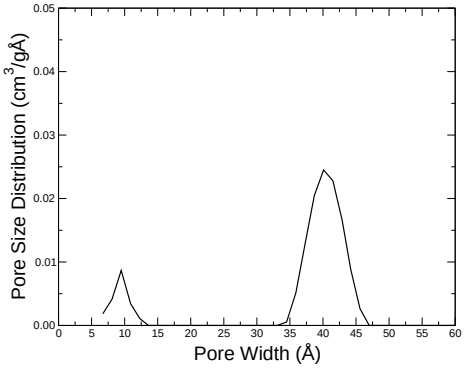

Figure 3.7: Pore size distribution for IVD. Full spectrum is shown.

Figure 3.7 shows the PSD obtained for the IVD sample. From this figure, the structure contains only two peaks, one in the micro-porous region around 10 Å, the

other around 40 Å. There are slight differences in the peak locations when compared to CCD, but overall the IVD structure is similar in general features.

Having shown transferability of the model between conditions and types of deposits for ethane adsorption, Costa and co-workers proceeded to examine adsorption of more complex species. Investigations in this area are difficult, as diffusional limitations of the samples constrain the complexity of the species for which experimental data can feasibly be obtained. Figure 3.8 shows a comparison between experimental data and simulated predictions for the adsorption of n-butane at 293 K on CCD. It is worth nothing that each isotherm point of the experimental data took at least 24 hours to obtain, highlighting the very slow adsorption kinetics of these materials. While the fit of the simulations is not as good as that for ethane, the model is still able to predict adsorption behaviour to a satisfactory degree.

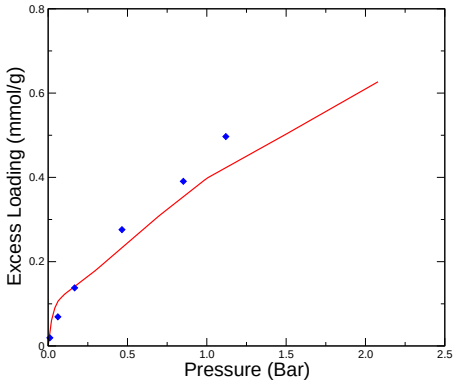

Figure 3.8: Comparison of experimental and simulated adsorption isotherms for n-butane on CCD at 293 K. Experimental points are shown as solid blue diamonds, and the simulated prediction is shown as the red line.

3.3 Adsorption of Fuel Components

With the validated model the final stage of the original project was to offer some insight into the adsorption behaviour of key fuel components onto the engine deposits. The species iso-octane (i-octane) and normal heptane (n-heptane) were chosen to represent branched and linear alkanes. These two fuels are often used as *primary reference fuels*[4] as two extremes of octane number (n-heptane being zero, i-octane being 100). Predictions of these isotherms were generated for the two engine deposit

structures, CCD and IVD. Temperatures of 420 K and 390 K were chosen to represent indicative system temperatures for each structure, and the results are shown in Figure 3.9.

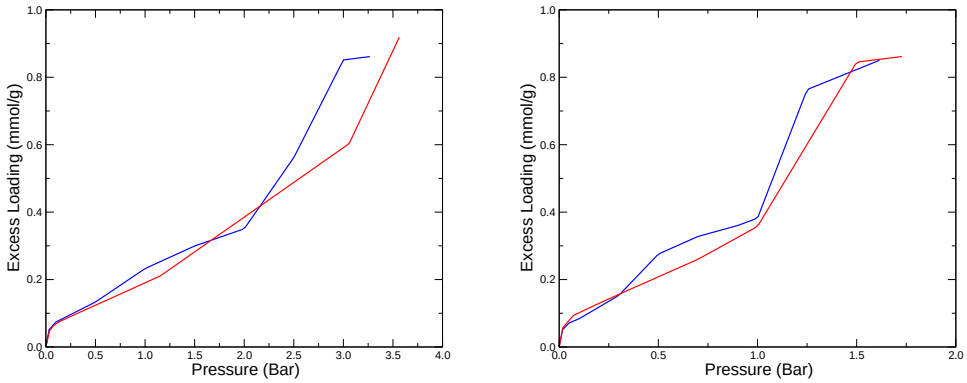

Figure 3.9: Predicted single component adsorption isotherms for CCD at 420 K (left) and IVD at 390 K (right). Blue lines are for i-octane and red lines are for n-heptane.

It can be seen from the isotherms that both i-octane and n-heptane adsorb with similar trends and in comparable amounts on both CCD and IVD. Large steps in density (particularly evident for IVD at 390 K, above 1 bar) result from both a limited number of points on the adsorption isotherms and limited number of adsorption isotherms within the kernel. Using these results, Costa and co-workers speculated that under static conditions engine deposits must adsorb substantial amounts of fuel, possibly comparable to the total amount of fuel introduced in the cylinder at a single stroke. This speculation will be re-visited on more quantitative grounds in Chapter 6. Of course, in reality an engine is a highly transient system, and it is difficult to predict how these isotherms may change when exposed to rapidly cycling conditions over a long period of time. We will speculate on the possible routes to this problem in the final chapter of the thesis.

3.4 Conclusions

To briefly summarise the conclusions drawn from the previous work, using only a single adsorption isotherm for ethane at 278 K on combustion chamber deposits, it was possible to develop a molecular model capable of predicting adsorption behaviour

of increasingly complex hydrocarbons under a variety of conditions. The accuracy of this model was established for simple species under different conditions, and for more complex alkanes. Using this model, it was possible to characterise the structure of a sample of CCDs by determining the associated pore size distribution. The model was shown to be transferable to intake valve deposits, accurately capturing adsorption properties of this deposit class as well. This transferability allowed insight into the structural features of an IVD sample in addition to that of the CCD.

Although the model accuracy began to decrease for more complex hydrocarbons, an understanding of the limitations of the model still gives merit to the predictions of more complex species where experimental studies are not feasible. It was shown that both CCD and IVDs have the capacity for substantial adsorption of both i-octane and n-heptane at the equilibrium limit. Engine conditions are dynamic, and equilibrium is unlikely to be achieved, however transient adsorption proceeding to a fraction of the equilibrium extent may still result in significant impact on fuel composition.

3.5 Limitations of the Model and Objectives of the Current Work

The original work by Costa and co-workers was the first step in studies of adsorption behaviour of engine deposits with respect to fuel components. The development of the model and its use in characterisation of the porous structures was the main focus in their investigation. However, the full potential of predictive simulations was not realised, as the studies of Costa and co-workers were limited to single component adsorption. Molecular simulations make it possible to investigate, in detail, multi-component adsorption phenomena in engine deposits. Along a similar line of thought, the representation of species that make up the gasoline fuel can be more accurately captured by including aromatic compounds. In the same way that linear and branched alkanes are represented using n-heptane and i-octane, extending the study to toluene would allow insight into the adsorption behaviour of aromatic species. Finally, building on the previous model of Costa and co-workers allowed us to critically re-examine this model and identify areas where it can be further refined. However, as shown in Chapter 5, this required further analysis into the robustness and accuracy of the model as a result of the introduced modifications.

With these in mind, the more detailed objectives of this thesis, as a progressive continuation of the work by Costa and co-workers, can be formulated as follows:

1. to further develop the original model by Costa and co-workers by considering more detailed adsorption isotherms and kernels; to explore behaviour of the modified model in characterisation of the deposits and in prediction of their adsorption properties

2. to investigate adsorption of aromatic species, represented by toluene, in different classes of deposit under relevant conditions

3. to explore adsorption of binary and ternary mixtures of representative fuel components in engine deposits under relevant conditions

Given the lack of data on adsorption of alkane mixtures in carbonaceous structures in general, either in application to engine deposits or in a broader context of activated carbons, the third objective of the thesis seems to be a particularly interesting and novel contribution.

Chapter 4

Adsorption of Alkanes in a Slit Pore

4.1 Introduction

Previous studies, as reviewed in Chapter 3, revealed a tendency of engine deposits to adsorb substantial amounts of alkane species. They also highlighted an important and underdeveloped avenue of research related to selectivity effects in engine deposits, in other words, possible preferential adsorption of one class of alkane species over the other. This effect may have important consequences for the composition of the mixture during the transient engine operation, biasing it towards alkane species with lower octane ratings. This idea is explored in further detail in Chapters 4, 5 and 6. In the current model, engine deposits consist of many pores of different sizes. However, in order to provide correct interpretation of results in this model, it is imperative to first understand adsorption processes and selectivity in individual slit pores. This will allow us to explore the ties between selectivity effects in the individual pores and behaviour of the whole sample, in which these effects are suppressed or amplified depending on the presence of the pores of a particular width in the PSD. Therefore, adsorption phenomena in a single slit pore is the focus of this chapter.

Two subjects are under investigation in this chapter. The first is concerned with selectivity effects between linear and branched alkanes. The motivation for such an investigation is two-fold: aside from the primary objective of this work, there is a distinct lack of fundamental studies for the adsorption of longer (C_4 and

above) alkanes in slit pores. Although adsorption of linear and branched alkanes has been extensively investigated in the context of catalytic cracking and separation in zeolites, slit pore geometries have received substantially less attention. At the same time, studies on different zeolitic pore geometries have revealed some interesting trends regarding alkane branching and chain length. There is some indication that these trends could extend to slit pore geometries as well. To this end, we compare single component adsorption isotherms for several branched and linear alkanes, as well as selectivities in binary mixtures. Selectivity will be revisited in later chapters in the context of adsorption in engine deposits.

For the second subject, we are interested in exploring the strength of interaction between different alkane species and a slit pore and how this property varies as a function of pore width. Here we will focus on the species directly related to the engine operation. Linear, branched and aromatic alkanes make up a significant proportion of standard gasoline fuels in the automotive industry (81 % by volume[73]). Thus, here we take the opportunity to introduce a third family of alkanes by also considering the adsorption of toluene alongside n-heptane and i-octane. The focus in this investigation still remains on adsorption in individual slit pores, and is limited to single component systems only. However, multi-component mixtures involving toluene are explored in Chapter 6.

The structure of Chapter 4 takes the following form. We begin by outlining the simulation methods and parameters used throughout this thesis, including details of the slit pore model, forcefield parameters and simulation details. We then present the first set of our results, comparing adsorption isotherms for single component systems of normal and branched alkanes. We look at the adsorption of n-butane, iso-butane (i-butane), n-heptane, n-octane and iso-octane (i-octane) at 390 K. Butanes are selected as the simplest alkane species for which the effect of branching can be studied. Normal heptane and i-octane are considered as representative fuel components, and n-octane is used to highlight the effect of branching on adsorption properties of i-octane. We focus only on three pore widths. Pores of 10 Å are typically present in all types of engine deposit studied, and 40 Å pores are selected to represent a characteristic width from the 30 - 50 Å range. While 20 Å pores do not exist in the deposits, this width is selected to understand any possible transitions in the adsorption regimes between 10 and 40 Å pores. We extend these studies to a binary mixture of n-heptane and i-octane, using a typical reference fuel composition, and investigate adsorption of the mixture at 390 K as a function of pore width.

Finally, we briefly explore adsorption hysteresis effects, observed for the cases where capillary condensation of adsorbing species takes place.

In the second part of the chapter, the affinity of adsorption of different species in slit pores is characterised using two key properties: Henry's constants of adsorption and isosteric heat of adsorption, which will be defined when appropriate. These properties are calculated as a function of pore width for n-heptane, i-octane and toluene. It should be noted that each stage of the results is preceded by a short review of the current state of knowledge in that particular area.

4.2 Simulation Parameters and Methods

In this section we take the opportunity to outline the parameters and simulation details used for all the adsorption simulations in this thesis. This includes force field parameters, details of the slit-pore model as well as simulation-specific information such as the types of attempted Monte Carlo moves and the number of cycles per simulation point. Critical properties of all the species considered in this work are available in Appendix B. Specific details on the characterisation procedure for obtaining pore size distributions are introduced in Chapter 5, where they become relevant. Procurement of the IVD and CCD samples and their characteristics, such as the elemental analysis, have been described in Chapter 3. Experimental results on ethane and normal butane adsorption used in this work have also been previously published,[17,39,40] including the details of the experimental procedure.

4.2.1 Force Field Parameters and the Slit Pore Model

All species are modelled using the TraPPE united atom forcefield,[53–55] within which an alkane CH_x group is represented as a single interaction site. The forcefield has been extensively parameterised to accurately reproduce vapour-liquid equilibria of various alkanes and their mixtures. This has been the primary reason (in addition to simplicity of the forcefield and high transferability of parameters) for selecting the forcefield for the studies in this thesis. For the atoms constituting the walls of the slit pores we adopt parameters from the previous work of Pinto da Costa et al.[39,40] A detailed table of the Lennard-Jones parameters is provided in Appendix C. Standard Lorentz-Berthelot rules are applied to generate Lennard-Jones parameters for the interactions between the unlike atoms. Toluene and ethane are treated as

rigid molecules. Details of the TraPPE forcefield for intramolecular contributions for flexible molecules are also summarised in Appendix C. The potential for adsorbate-adsorbate interactions is truncated at the cut-off distance of 15 Å, with no long-tail corrections applied.

A model slit pore in this study consists of two walls, where each wall is made of six graphene layers. Within the walls the layers are separated from each other by 3.35 Å. The width of the slit pores corresponds to the distance in the z direction between the centres of the atoms of the inner graphene layers, as shown in Figure 4.1, using 10 Å as an example. Each pore has x and y dimensions of 31.73 and 34.08 Å respectively and the system is placed in periodic boundary conditions in both x and y directions.

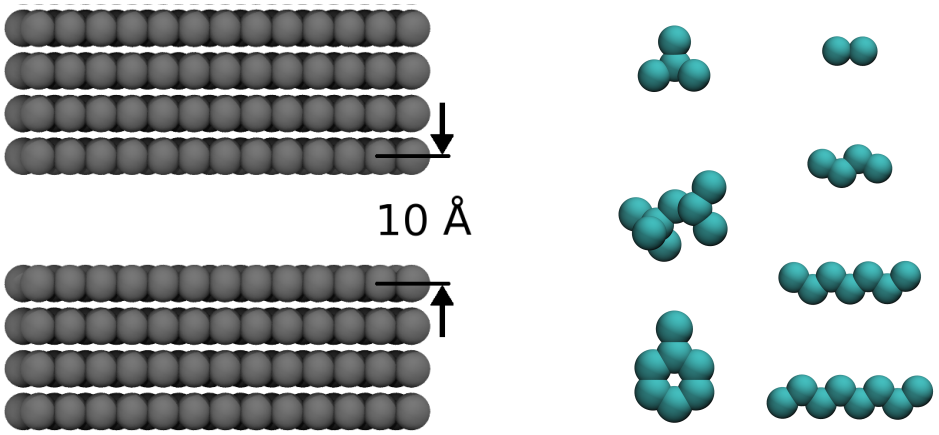

Figure 4.1: On the left: a schematic visualisation of the 10 Å slit pore model. Only four layers of each wall are shown, in the actual model each wall consists of six layers. On the right: united atom representations of the adsorbate species considered in this work. The first column shows, from top to bottom, i-butane, i-octane and toluene. The second column shows, from top to bottom, ethane, n-butane, n-heptane and n-octane. The size of the atoms in both panels is scaled down from the original σ values by ~30 % for better visualisation.

4.2.2 Simulation Details

All grand canonical Monte Carlo simulations are performed using the Multipurpose Simulation Code, MuSiC.[58] For linear alkanes we employ configurational bias Monte Carlo (CB GCMC) combined with the energy bias method (CB/EB GCMC), using

the pre-calculated potential maps.[57] These maps are generated using 30 Å cut-off for interactions between atoms of the walls and atoms of the adsorbing species. To accommodate this cut-off in the generation of the maps, several replicas of the system are considered in periodic boundary conditions. Each CB/EB GCMC move consists either of insertion, deletion, translation or re-growth attempt, selected with equal weight.

As mentioned in Chapter 2, for branched alkanes we use a simplified version of the Macedonia and Maginn CB GCMC scheme.[49] In the scheme of Macedonia and Maginn, an additional simulation is required to generate a library of conformations of each branched fragment which are later used in the CB GCMC simulation to assemble the whole molecule. We found that highly branched species considered in this work benefit little from the complicated machinery of the CB GCMC approach.[59] Instead we use a simplified approach, where branched alkane molecules are inserted as rigid structures selected from a library of pre-calculated conformations corresponding to the canonical distribution at a particular temperature. For this, we first perform a Molecular Dynamics simulation of a small set of molecules (100 - 200) in the bulk gas phase, under constant volume and temperature conditions. The temperature of the system is maintained with the Nosé-Hoover thermostat. The molecules are treated as ideal gas and only intramolecular interactions are considered. This simulation provides a library of canonically distributed molecular conformations of the branched alkane in question. In the second stage, an energy bias grand canonical Monte Carlo (EB GCMC) simulation is performed. Here the configurations of the molecules attempted for insertion are drawn from the pre-calculated library. Overall, an EB GCMC scheme for a branched alkane consists of insertion, deletion, rotation and translation attempts, selected with equal weights. We have shown in the previous publication that in the case of highly branched molecules, such as i-octane, this approach is as accurate as the complete CB/EB GCMC.[59]

Each point on the isotherm is generated using at least 5×10^6 (and up to 1×10^8) moves, with 70 % of these being allocated for equilibration. Upon adsorption, we consider a series of increasing pressure values, and the last configuration from a lower pressure point serves as a starting configuration for the next, higher pressure point. To simulate the desorption process, the protocol is reversed and a simulation consists of a series of decreasing pressure values, again with the configuration of the preceding point used as an input configuration for the following point. This set-up has been employed in several previous studies to investigate hysteresis in slit pores

and more complex porous materials.[74,75] An adsorption simulation takes fugacity of adsorbing species as an input parameter and returns the absolute amount of adsorbed species as a result. However, it is usual to report isotherms as the *excess* amount of loading versus the pressure of adsorbing species. In order to convert between these conventions, we use the Peng-Robinson equation of state to relate the fugacity and pressure of adsorbing species, and the following expression to obtain the excess amount.[76]

$$n^{\text{ex}} = n^{\text{abs}} - \rho_{\text{bulk}} V_p \tag{4.1}$$

where n^{ex} and n^{abs} are the excess and absolute amounts adsorbed, ρ_{bulk} is the density of the bulk phase at the conditions of interest calculated using the Peng-Robinson equation of state, and V_p is the pore volume. This is calculated using $V_p = L_x \times L_y \times (L_z - 6.1\,\text{Å})$, where L_x and L_y being the dimensions of the pore in the x and y directions, L_z is the width in the z direction, and 6.1 Å is the smallest width of the pore where adsorption is still possible. This calculation of the pore volume is consistent with the previous studies of adsorption in slit pores.[42]

4.3 Adsorption of Branched versus Linear Alkanes

This section addresses the following scientific question: is it linear or branched alkanes that adsorb more strongly in a carbonaceous slit pore, and how does this order depends on the width of the pore? For this we consider several alkane species adsorbing in pores of several representative widths. However, prior to presenting the results, it is important to introduce some additional scientific concepts required for the interpretation of the these results, namely capillary filling, condensation and hysteresis in slit pores. It is also important to review recent fundamental studies on adsorption and selectivity of alkanes in simple slit pores. These will be the subject of the next two sub-sections.

4.3.1 Capillary Condensation, Capillary Filling and Hysteresis in Slit Pores

An extensive review of the thermodynamics of confined fluids is provided by Gelb et al,[77] here we provide only a brief summary to introduce concepts required throughout

the chapter.

Consider adsorption of a subcritical fluid in a mesoporous (2 - 50 nm) slit pore. At low pressures there is little adsorption, but as pressure increases there is a steady increase in adsorption loading as species begins to layer on the pore walls. Molecules tend to layer themselves against the walls where the interactions between the walls and molecules are felt most strongly. At some point the threshold value of pressure is reached and the adsorbed species undergoes a phase transition. This is known as *capillary condensation* and is associated with a large and sudden increase in the adsorbed loading, a schematic of an isotherm undergoing such a transition is shown in Figure 4.2 (on the left). Now, to generate a desorption isotherm, we start with a high pressure point and gradually decrease pressure values. As shown in our schematic (Figure 4.2) there will be a region of pressure values where the desorption isotherm takes a different path from the adsorption isotherm, leading to so-called hysteresis.

Classical theories of adsorption are based on the Kelvin equation, and explain hysteresis in the following way. In our consideration we have a slit pore that is open at both ends. Capillary condensation is nucleated by the film of fluid that accumulates on the walls of the pore, shown in the schematic on the right of Figure 4.2 (left column). The relative pressure of this event is influenced by the distance between the two films (i.e. the width of the pore minus the combined thickness of the film), but is largely governed by the stability of the film on the surface of the wall.

The desorption processes begins with the pore being full. Evaporation takes place from the hemicylindrical menisci at either end of the liquid, as shown in Figure 4.2. The relative pressure of this event will correspond to the radius of the curvature of the menisci, according to the Kelvin equation. From the Figure 4.2 it is clear that during adsorption and desorption process the system goes through a different sequence of states. As a result, condensation and evaporation occur at different relative pressures, which gives rise to the hysteresis. From this treatment, the adsorption branch of hysteresis corresponds to the metastable state, while the desorption branch links two phases in the pore at the thermodynamic equilibrium.

In computer simulations, the adsorption branch behaves as described above, however the situation is somewhat different for desorption. As the system is placed in periodic boundary conditions, there is no hemicylindrical menisci between the confined liquid and vapour phases (this system can be viewed as an infinitely long slit pore). Instead, the formation of a vapour phase during desorption is also associated

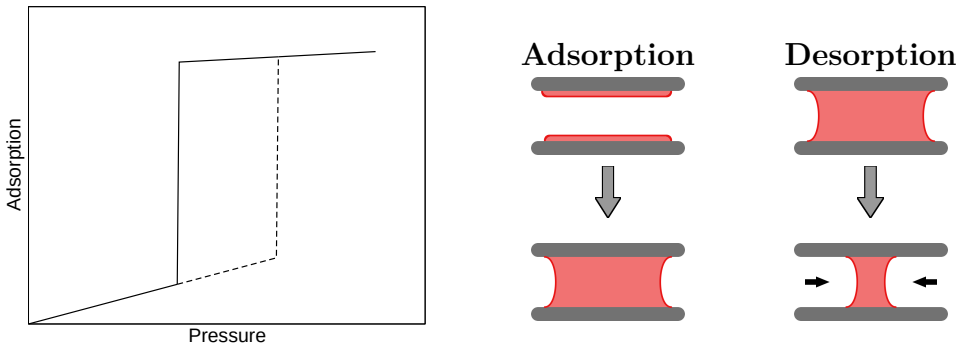

Figure 4.2: On the left: Schematic of an adsorption/desorption isotherm exhibiting hysteresis. The dashed and solid lines indicate the adsorption and desorption branches respectively. According to classical theories of adsorption, the adsorption branch extends into the meta-stable region while the desorption branch links the vapour and liquid phases at thermodynamic equilibrium. On the right: in the first column, a schematic showing the nucleation process during adsorption in a slit pore. In the second column, a schematic showing how the menisci move into the pore as evaporation occurs during the desorption process.

with a nucleation process (in this case a bubble of vapour must form). Thus, the desorption branch will also extend into the metastable region, prior to capillary evaporation. In between the adsorption and desorption steps on a simulation adsorption isotherm, there is a pressure value that corresponds to the true phase coexistence of the confined vapour and liquid phases, Figure 4.3.

Identification of this point requires thermodynamic integration to obtain a condition where:

$$\mu_L = \mu_V$$

and

$$\phi_L = \phi_V$$

where ϕ is the grand potential density and μ is the chemical potential. This process can be used to construct a phase diagram for the confined fluid by repeating this calculation for several values of temperature. This phase diagram will be similar in shape to the bulk phase diagram, but with a lower critical point, higher vapour densities, and lower liquid densities as shown in Figure 4.4. As the isotherms approach the confined fluid critical point (by increasing temperature) the hysteresis

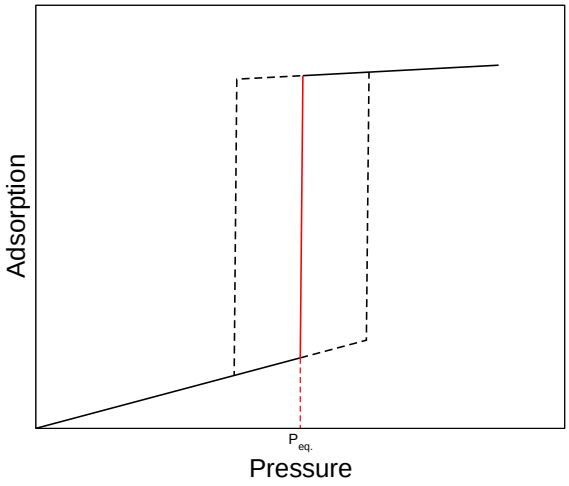

Figure 4.3: Schematic of an adsorption/desorption isotherm highlighting the meta-stable regions of hysteresis within molecular simulations of adsorption in an infinitely long slit pore. Both adsorption and desorption branches are associated with a nucleation process, and extend into a meta-stable region (shown by dashed lines). The red line indicates the location of the true phase coexistence at pressure P_{eq}.

loop will begin to shrink and eventually disappear:

Alternatively, a greater degree of confinement leads to a greater reduction in the size of the phase envelope. For a single value of temperature, a gradual decrease in the width of the pore will lead to the reduction of the hysteresis loop, while the values of the confined vapour and liquid densities will be closer to each other. For narrow pores (in the microporous range: less than 20 Å) the capillary condensation, hysteresis and vapour-liquid envelope disappear. The adsorption isotherm now corresponds to the *capillary filling* process, often characterised as Type I isotherm in the IUPAC classification.[60] Figure 4.5 shows how reducing the pore size changes the shape of the isotherm from capillary condensation towards capillary filling.

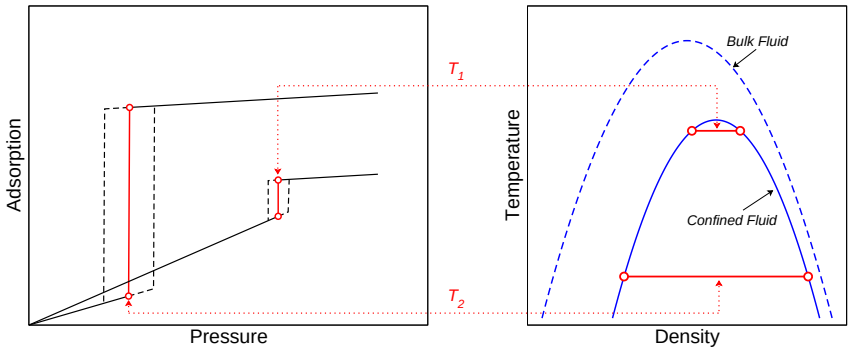

Figure 4.4: On the left: schematic showing hysteresis isotherms for two different temperatures, T_1 and T_2, in identical pores. Included are the meta-stable regions of the adsorption and desorption branches (black dashed lines) and the true phase coexistence pressure (red solid line). On the right: schematic showing the temperature - density phase diagram for the bulk (dashed blue line) and confined (solid blue line) fluid phase. The critical point of the confined fluid is suppressed compared to the bulk, gas - phase densities are higher, and liquid - phase densities are slightly lower compared to the bulk phase. Solid red lines indicate the two-phase coexistence, corresponding to the capillary condensation on the left, at two different temperature, T_1 and T_2. These are linked to the isotherms by the dotted red lines, and temperature T_1 is greater than T_2. As temperature is increased, the isotherm hysteresis loops on the left shrink as the coexistence curves move closer to the confined critical point.

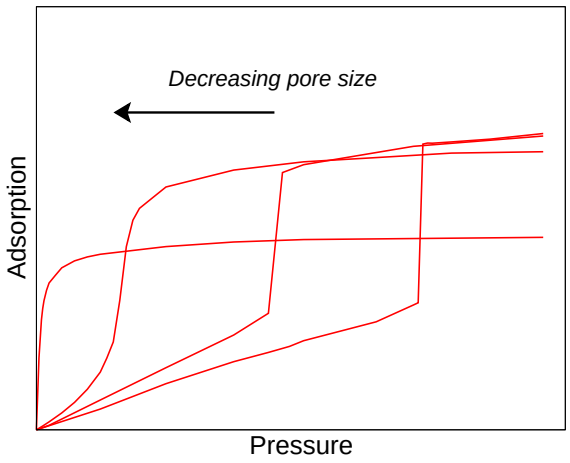

Figure 4.5: Schematic showing how isotherm shape changes from capillary condensation towards capillary filling as the extent of confinement increases.

4.3.2 Previous Studies of Adsorption of Branched and Linear Alkanes

Severson and Snurr have recently performed an extensive simulation study of single-component alkane adsorption in carbon slit pores.[78] Adsorption of linear alkanes (from ethane to pentadecane) has been explored as a function of chain length, pore width and temperature.[78] Vapour - liquid phase behaviour, critical properties and surface tension of linear alkanes (from methane to normal octane) under confinement in slit pores have been recently investigated by Singh et al.[79] In particular, similar to the confined phase behaviour of simple fluids, the authors observed depression of the vapour - liquid critical temperatures to lower values, compared to the bulk system, with the extent of depression enhanced by stronger confinement.[79]

Studies of binary and multicomponent mixtures of alkanes in slit pores are rare, and their behaviour has not been explored in any appreciable detail. However, the existing studies suggest that these systems may exhibit a number of interesting effects. Tan and Gubbins considered adsorption of binary mixtures of methane and ethane as a function of carbon slit pore width, temperature and mixture composition using non-local density functional theory.[80] They found that selectivity is strongly affected by pore size. In the zero pressure regime, selectivity of ethane exhibited a pronounced maximum as a function of pore width. At finite pressures and loadings several distinct types of selectivity isotherms have been identified, depending on the temperature relative to the critical temperature under confinement.[80] Cracknell et al. also investigated selectivity for methane - ethane mixtures in slit pores.[36] Using grand canonical Monte Carlo simulations, they observed a number of interesting phenomena associated with the geometric arrangements of diatomic molecules in narrow pores. This work was further extended to ethane - propane binary mixtures.[37] It was demonstrated that molecular species may exhibit an additional range of packing effects, leading to new types of selectivity isotherms, not observed by Tan and Gubbins.[37]

Studies of systems containing long-chained linear and branched alkanes on carbon slit pores are rare. More frequently, investigations of such systems focus on the adsorption onto zeolites or carbon nano-tubes. These studies agree on several trends in adsorption behaviour regarding mixtures of alkanes and their isomers. The classification of three distinct types of behaviour, or factors, that strongly influence the adsorption behaviour in these systems was outlined by Krishna and co-workers,

who looked at the adsorption of branched and linear alkanes in silicalite.[81] While we may build upon the details of these effects, it is convenient to use them as an initial foundation for describing alkane adsorption trends.

The first of these is a carbon number effect: molecules with a lower carbon number have more favourable adsorption at higher loadings due to an ability to pack more efficiently. On the other hand, at low loadings the higher carbon number causes more favourable adsorption as there is a higher interaction potential arising from the additional carbon group. The second factor is a configurational effect, where linear molecules are able to pack more efficiently than their branched isomers. The final effect discussed is a molecule length effect, arising between linear and branched molecules under high confinement. In this situation the molecule with the shortest length is able to pack more efficiently in the very narrow pores, and correspondingly shows more favourable adsorption.

An extensive body of work on alkane adsorption has been carried out in application to zeolites, and we begin by discussing single-component systems of linear and branched species. Vlugt et al., Calero et al. and Krishna et al. investigated adsorption of linear alkanes in silicalite.[48,81,82] There is a consensus regarding the behaviour of single-component isotherms for linear alkanes. They found a distinct increase in low-pressure loading as the length of the carbon chain is increased. At high pressure, this trend is reversed: attributed to the carbon number effect mentioned above. Severson and co-workers showed that this trend is also true for single-component adsorption in carbon slit pores.[78]

Single component isotherms of mono-branched alkanes also exhibit the carbon number effect: adsorption at low pressures favour the alkanes with higher carbon numbers, adsorption at high pressures favour those with lower carbon numbers. There are no systematic studies for the adsorption of pure branched alkanes on carbon slit pores, but various studies show that this trend holds for the adsorption on silicalite.[48,82]

Moving from single-component systems into mixtures, carbon number effects are still observed. Mixtures of purely linear, long-chain alkanes were shown to have favourable adsorption towards long chains at low pressure, and short chains at high pressure. This was separately shown to be true in zeolites by Calero et al.[82] and Krishna et al.,[81] in carbon nanotubes by Jiang and co-workers[83] and in metal organic frameworks, also by Jiang and co-workers.[84]

Mixtures of purely branched alkanes were also shown to exhibit the carbon num-

ber effect by Calero et al., who studied adsorption behaviour for the ternary mixture of 2-methylbutane, 2-methylpentane and 2-methylhexane at 300 K on silicalite.[82] It should be noted that Calero et al. found a sharp increase in the 2-methylbutane loading in silicalite, not seen for the other species, causing a favourable selectivity over 2-methylpentane. This is likely to be a special effect arising due to the intersecting pores found in the silicalite zeolite rather than a general trend for alkanes, and is unlikely to be found on carbon slit pores.

Systems involving different types of alkanes have also been studied and selectivity arising from the configurational effect has been observed. In some cases of very narrow confinement, molecular sieving can lead to the the exclusion of branched molecules. An early example is the experimental work by Santilli on hexane isomers in silicalite.[85] Santilli reported that the adsorption capacity of alkanes decreased as the level of molecule branching increased, down to a complete exclusion of 3-methylpentane from silicalite. More recently, Vlugt and co-workers used configurational bias Monte Carlo to study shape selectivity effects of alkane adsorption on silicalite.[48] They looked at binary, equimolar mixtures of the linear and 2-methyl isomers for different alkane sizes ranging from C_4 to C_7. At low pressures linear and branched isomers adsorbed in similar amounts. However, at some threshold loading the branched isomer was "squeezed out" of the zeolite in favour of the linear counterpart. This is an example of the configurational effect mentioned earlier, and has been observed in other studies, such as those by Calero, Smit and Krishna.[82] Using configurational bias Monte Carlo they studied mixtures of linear, mono-branched and di-branched alkanes from C_5 to C_7 on several zeolites. They observed that increased levels of branching suppressed adsorption of these molecules compared to the linear counterpart. From these studies they established an adsorption preference order for linear and branched alkane isomers $n\mathbf{C} > i\mathbf{C} > neo\mathbf{C}$, referring to normal alkanes, mono-branched alkanes and di-branched alkanes respectively. This same adsorption preference order was seen by Jiang et al. for both carbon nano-tubes[83,86] and metal organic frameworks.[84] This order in preference for alkane isomers is collectively called *shape selectivity* effect.

Contrary to this, adsorption in high confinement pores has been found to show selectivity in favour of branched over linear molecules. This is an example of the molecule length effect. Krishna et al.[81] found that, in cylindrical pores of specific size, the doubled-branched isomers were more favourably adsorbed, followed by single-branched and finally linear alkanes. The pores examined were large enough

to accommodate the bulkiest, di-branched isomer without steric penalties. In this situation, the more compact chain is shorter than other isomers, and so can pack more efficiently in the cylindrical pore. The resulting adsorption preference order for these cylindrical pores is $neo\mathbf{C} > i\mathbf{C} > n\mathbf{C}$, the complete reverse of that described previously. This trend is known as *inverse shape selectivity*, and was also reported by others, including Jiang and Sandler.[86] While investigating adsorption of mixtures of pentane isomers in carbon nano-tubes of three specific sizes, Jiang and Sandler found inverse shape selectivity was highly dependent on pore size. Only the smallest nano-tube examined (pore size of approximately 6.39 Å) exhibited inverse shape selectivity, larger nano-tubes (10.46 and 24.03 Å pores) instead favoured linear alkanes and showed regular shape selectivity. If the pore size becomes too low, shape-selectivity gives way to molecular sieving, and the branched molecules are fully excluded from the pore. Such effects were found by Santilli and co-workers[87] for adsorption in zeolites. They found that in cylindrical zeolite pores between 6.5 and 8 Å, inverse shape selectivity occurred. However, pores smaller than 6.5 Å excluded the branched molecules (molecular sieving effects), while above 8 Å they showed regular shape selectivity (i.e. favouring linear molecules).

One of the few studies of shape selectivity in carbon slit pores was undertaken by Jiang,[88] who looked at adsorption of pentane isomers in carbon slit pores using configurational bias Monte Carlo. It was found that for equimolar ternary mixtures of n-pentane, 2-methylbutane and 2,2-methylpropane, carbon slit pores of 24.03 and 10.46 Å showed shape selectivity with the selectivity preference $n\mathbf{C} > i\mathbf{C} > neo\mathbf{C}$ over all pressures studied. However, for the narrower pore of 6.39 Å, inverse shape selectivity was found, with the selectivity preference $neo\mathbf{C} > i\mathbf{C} > n\mathbf{C}$. From the pure-component density profiles it was seen that each isomer could form only a single layer within the 6.39 Å pore, leading to molecule length effect. Jiang argues that as the degree of branching increases, the molecule becomes bulkier in the z-direction (across the pore), but its area in the xy-plane is reduced. This molecule length effect had previously only been reported in cylindrical channels found in certain zeolites[48,81] and carbon nano-tubes.[83] The conclusion that shape selectivity versus inverse shape selectivity is dependent on pore size, rather than pore geometry, has important ramifications for the work of this thesis. It implies that the same effects should be seen in carbonaceous slit pores in this study. This in turn suggests that, depending on the PSD, the branched alkane composition of the fuel can be increased or decreased, with the corresponding consequences for engine operation.

From the studies of branched and linear zeolite adsorption, one particular investigation by Calero et al.[82] stands out as especially interesting in relation to this thesis. A binary mixture of n-pentane (C_5) and 2-methylpentane (C_6) shows that at low pressure the branched C_6 adsorbs more strongly than the linear C_5 due to carbon number effects. As pressure is increased, molecule configuration effects override the carbon number effects, and the linear C_5 loading exceeds that of the branched C_6.[82] This is particularly relevant as the linear C_5 versus branched C_6 is analogous to the adsorption of n-heptane versus iso-octane, which is a key focus of this thesis. While the C_6 here is only mono-branched, iso-octane used in gasoline fuel is the 2,2,4-trimethylpentane isomer containing three "degrees" of branching (i.e. three additional methyl groups, each causing a "branch"). As such, there is likely to be a fine balance regarding i-octane - n-heptane selectivity where the extra carbon group (promoting selectivity of i-octane) is balanced against the increased branching, which is likely to suppress i-octane selectivity at higher pressures. To de-couple the effect associated with an extra alkane group in i-octane from the effect of branched structure, we will further consider n-octane and adsorption of both i-octane and n-octane will be compared to each other and to that of n-heptane.

4.3.3 Single Component Results

We begin our analysis with the single adsorption isotherms for linear and branched butanes. Here selectivity, or affinity of a slit pore towards particular species, is defined by simply higher loading of this species compared to other adsorbates at a given value of pressure. A more rigorous definition of selectivity is introduced later in the chapter in the context of mixture adsorption. At 390 K, the bulk condensation pressures are about 2,000 and 2,600 kPa for n-butane and i-butane, respectively. The adsorption isotherms shown in Figure 4.6 and 4.7, span the pressure range up to the saturation pressure of the species. Figure 4.6 shows the adsorption isotherms for a 10 Å pore using normal and logarithmic pressure scales. Adsorption isotherms have Type I shape and the loading of butanes (shown as number of molecules per simulation cell) is very similar for the two isomers. A slightly higher affinity towards i-butane, compared to n-butane, across all pressure ranges is in-line with the findings of Jiang,[88] who observed a preference of i-pentane compared to n-pentane at all pressures in 6.39 Å carbon slit-pores. Therefore in a 10 Å pore we observe inverse shape selectivity, although the effect is very weak.

In the larger 20 Å pores the shape of the butane isotherm changes and becomes more linear, shown in Figure 4.7. In both 20 and 40 Å pores, there is a slightly higher loading of n-butane over i-butane in the whole pressure range. This is a general reflection of the relative bulk properties of the isomers, with n-butane being generally closer to the bulk condensation pressure on the presented pressure scale. The change from inverse shape selective behaviour (preference for branched molecules) in the narrow 10 Å pore to shape selective behaviour (preference for linear molecules) in wider pores is in-line with the findings reported by Jiang.[88]

However, there are also some interesting differences with the work of Jiang. In a pore of 24.04 Å, Jiang observed complete shape selectivity (i.e. a preference for linear alkanes at *all* pressure values on the isotherm). In a 6.39 Å pore, complete inverse shape selectivity was observed (i.e. a preference for branched species at *all* pressures on the isotherm). In a 10.46 Å pore Jiang found shape selectivity at low pressure that switched to inverse shape selectivity at higher pressures.[88] It seems in our systems complete inverse shape selectivity behaviour remains in larger pores compared to that of Jiang. We note here however that, in addition to nature of the species, width of the pores and parameters of the solid fluid interactions, these effects will also be a function of temperature, with the studies of Jiang conducted at 300 K.

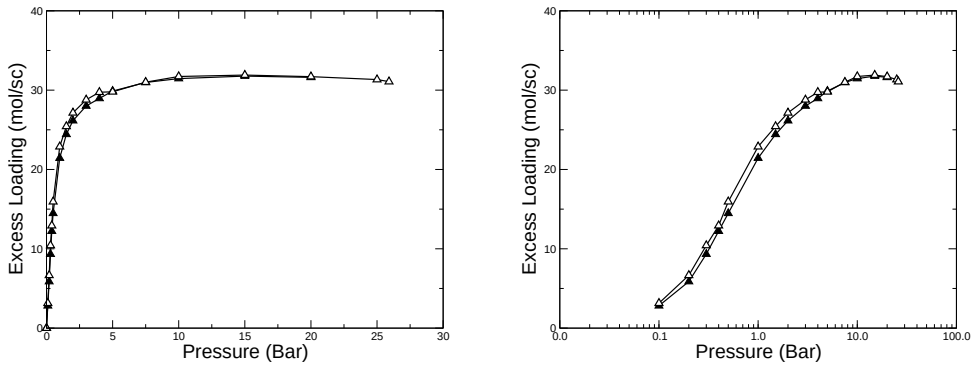

Figure 4.6: Adsorption isotherms (number of molecules per simulation cell as a function of pressure) for n-butane (black triangles and black lines) and i-butane (white triangles and black lines) in 10 Å slit pore at 390 K. Right panel uses the logarithmic scale for pressure.

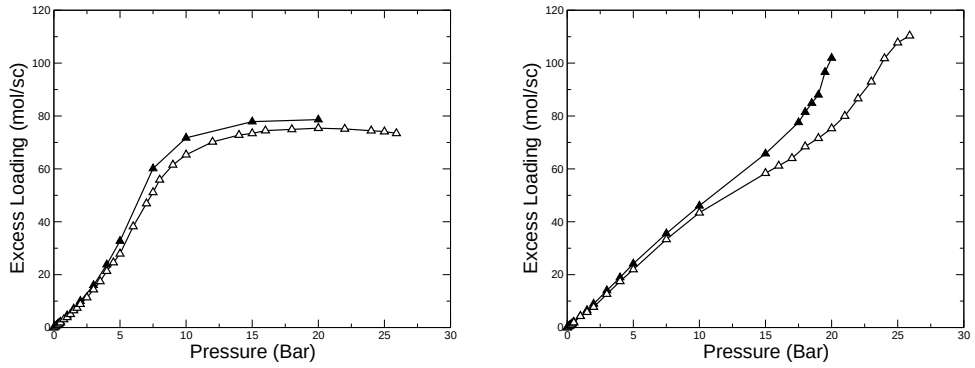

Figure 4.7: Adsorption isotherms (number of molecules per simulation cell as a function of pressure) for n-butane (black triangles and black lines) and i-butane (white triangles and black lines) in 20 Å slit pore (left panel) and 40 Å slit pore (right panel) at 390 K.

Higher alkanes exhibit a more complex landscape of behaviour. In Figure 4.8 adsorption isotherms for n-heptane, n-octane and i-octane in 10 Å slit pore are shown. All three species exhibit Type I isotherms at these conditions. In these systems the carbon chain length has increased from C_4 to C_7 and C_8, and as a result we see a shift of the isotherms towards lower pressures. This is as expected: as additional carbon groups are added, the interaction strength with the pore increases. Such trends were noted by Severson and Snurr.[78]

The system temperature is 390 K, and so the higher alkanes are further from their critical points than for the butane systems. This is evidenced by the stronger sub-critical characteristics of the confined fluids, such as capillary condensation behaviour in larger pores (see Figure 4.10). In this regime, higher loading of n-octane compared to n-heptane is an enthalpic effect associated with the presence of an additional alkane group in the octane molecule. As pressure is increased the loading of n-heptane exceeds that of n-octane. This is a result of the "molecule length effect", as defined by Krishna et al:[81] n-heptane has a shorter chain length, and so is able to pack more efficiently than the n-octane. For normal alkanes this trend is in agreement with the previous observations from various authors.[48,78,82]

From Figure 4.8, the loading of i-octane is similar to the loading of n-octane. Shape selectivity behaviour is known to depend on pore size.[88] For the majority of the pressure range we see inverse shape selectivity, where i-octane loading exceeds

that of n-octane. This must be a result of a more efficient packing of i-octane in a pore of this particular size. As illustrated in Figure 4.9, 10 Å can not accommodate formation of two layers of linear alkanes, and so the shortened length of the i-octane allows superior packing. This superior packing of branched isomers over linear agrees with previous observations of inverse shape selectivity by various authors.[81,82,88,89] At very low pressure, however, n-octane has a higher loading (first two points on the isotherm, see the plot on the logarithmic scale on the right in Figure 4.8). This reversal in trends with increasing pressure is characteristic for pores of this size, as seen in the work of Jiang[88] and discussed above. For the octane isomers at 390 K, it seems 10 Å is the pore size corresponding to this transition. It it is expected that as pore size is increased, the n-octane loading will exceed that of i-octane on a more extended pressure range (and indeed this is what is observed, as we will see later). Finally, just to verbalise the results in Figure 4.8, loading of i-octane is higher than than for n-heptane at all pressures, and at high pressures loading of n-heptane is higher than n-octane due to more efficient packing of shorter chains.

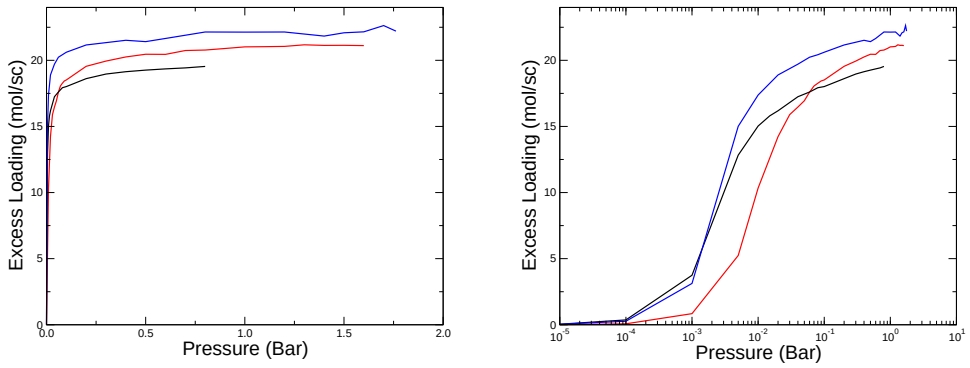

Figure 4.8: Adsorption isotherms (number of molecules per simulation cell as a function of pressure) for n-heptane (red lines) and n-octane (black lines) and i-octane (blue lines) in 10 Å slit pore at 390 K. Right panel shows the data using the logarithmic pressure scale.

Figure 4.10 shows adsorption isotherms for n-heptane, n-octane and i-octane in 20 and 40 Å pores at 390 K. In the 40 Å pore, the initial slope of the isotherms indicates decreasing affinity from n-octane to i-octane to n-heptane. This trend is also seen in the 20 Å pore for n-octane with respect to the other species, however the initial slopes for i-octane and n-heptane are essentially the same (see Figure 4.10

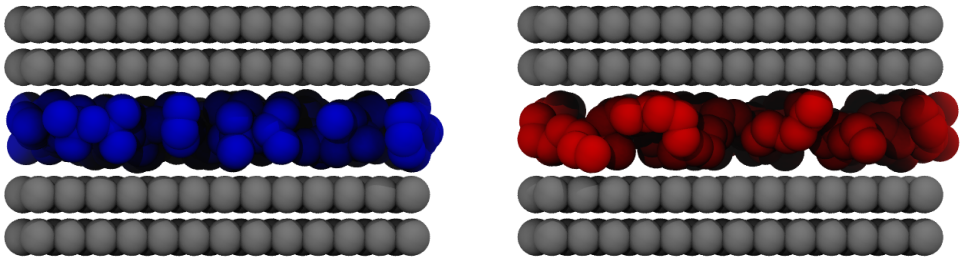

Figure 4.9: Visualisation snapshots of i-octane (left) and n-heptane (right) at high loadings in a 10 Å pore. Two layers of graphene out of six constituting the walls of the pore are shown. In both panels the size of the pore atoms are scaled down from the original σ by ~30 % for better visualisations. Species atoms remain unscaled.

inset). From this figure, it is also clear that alkanes in carbonaceous slit pores follow general trends for confined fluid phase behaviour.

Specifically, in both 20 and 40 Å pores all three species undergo capillary condensation, with n-octane condensing first followed by i-octane and then n-heptane. In the 20 Å pore the location of the capillary condensation is shifted further towards lower values of pressure, compared to 40 Å. In both pores capillary condensation occurs at lower values of pressure, compared to the bulk condensation (1.7, 0.79, 1.63 bar at 390 K for bulk n-heptane, n-octane and i-octane, respectively). In a larger pore, all three species also exhibit substantial desorption hysteresis, whereas in the 20 Å pore the transition has no visible hysteresis. It is important to emphasize here that both adsorption and desorption transitions observed here for 40 Å pore are hysteresis transitions and neither of the branches corresponds to the true location of the confined vapour - liquid equilibrium.

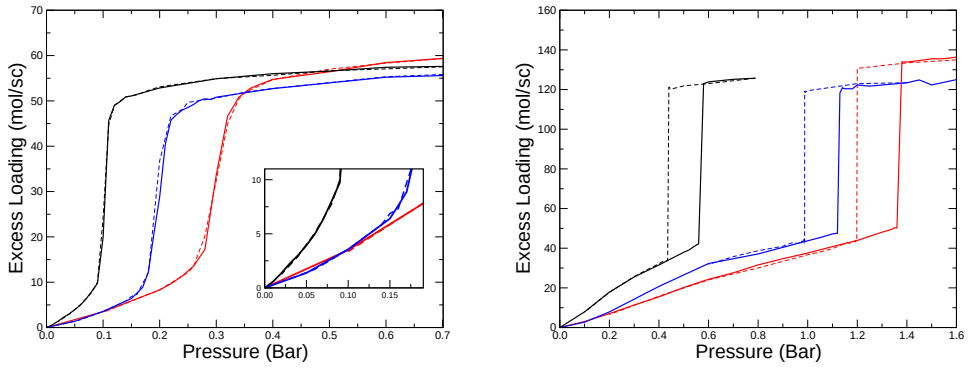

Figure 4.10: Adsorption and desorption isotherms (number of molecules per simulation cell as a function of pressure) for n-heptane (red solid line for adsorption, red dashed line for desorption), n-octane (black solid line for adsorption, black dashed line for desorption) and i-octane (blue solid line for adsorption, blue dashed line for desorption) in a 20 Å slit pore (left panel) and a 40 Å slit pore (right panel) at 390 K. On the left, the initial adsorption in 20 Å pore is expanded in the inset.

Following the description of the confined fluid phase behaviour provided earlier, in 20 Å pores the temperature of interest (390 K) is much closer to the corresponding critical points of the confined alkanes and the envelopes of metastability are expected to become smaller, compared to wider pores. We also highlight here that although i-octane initially adsorbs more strongly compared to n-heptane (as seen from the lower values of pressure for capillary condensation), at higher pressures both linear alkanes tend to compact more effectively compared to i-octane, and the density of linear alkanes is slightly higher than that of the branched one. This behaviour in 20 and 40 Å pores is qualitatively different from that for the 10 Å pore. In terms of n-octane vs i-octane adsorption, 20 and 40 Å pores show direct shape selectivity over the whole pressure range as expected. Figure 4.11 shows the same adsorption isotherms for n-heptane, n-octane and i-octane in a 40 Å pore plotted as a function of relative pressure at 390 K. It is interesting to note the reversal in condensation trends between the octane isomers: i-octane condenses at a lower relative pressure than n-octane. This indicates that branched isomers are more influenced by confinement effects than the linear counterparts.

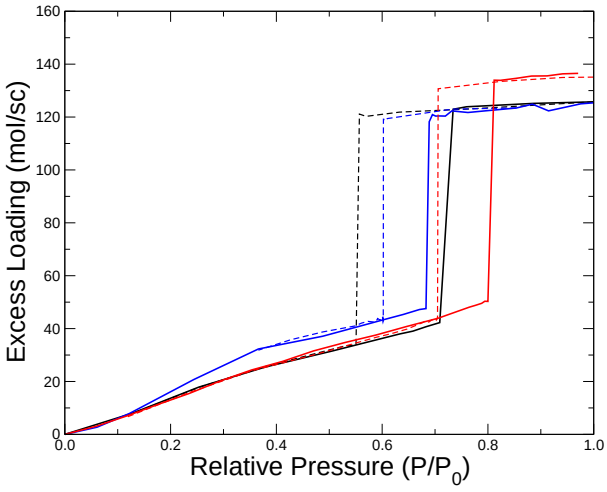

Figure 4.11: Adsorption and desorption isotherms (number of molecules per simulation cell as a function of relative pressure) for n-heptane (red solid line for adsorption, red dashed line for desorption), n-octane (black solid line for adsorption, black dashed line for desorption) and i-octane (blue solid line for adsorption, blue dashed line for desorption) in a 40 Å slit pore at 390 K.

4.3.4 Binary Mixture Results

Binary mixtures of i-octane and n-heptane are often used as primary reference fuels. Here we begin with the adsorption behaviour of just one particular, commonly used composition, with 90 % i-octane 10 % n-heptane on a liquid volume basis. The mixture corresponds to 0.89 mol fraction of i-octane. Before we consider the outcomes of the simulations, it is important again to briefly summarise what we might expect to observe.

Phase behaviour of confined mixtures has been investigated to a substantially less extent than that for single components.[77] In the simplest scenario, one would expect the confined fluid phase diagram to reflect at least some features of the bulk phase behaviour. For example, experimental studies on the liquid-liquid phase coexistence of nitrobenzene and n-hexane mixtures reveal a confined phase diagram similar in shape to the bulk one but with smaller phase envelope.[77] Gibbs ensemble studies of phase behaviour of binary mixtures of CO_2, CH_4, and N_2 suggest that confinement in slit pores leads to the depressed critical point and smaller vapour - liquid envelope compared to the bulk system.[90]

Consider now a bulk mixture of i-octane and n-heptane. For simplicity we can

treat this mixture as ideal, following Raoult's law. In the bulk phase, on the P-x-y diagram, components of an ideal binary mixture form a two-phase envelope between the liquid phase and the vapour phase. In the isothermal compression process, which starts from a location in the vapour region of the diagram, the first drop of liquid forms at the pressure dew point. As further compression proceeds, a two-phase system is observed for a range of pressures, until condensation completes and only liquid phase is present. In the grand canonical simulation of mixture adsorption, we specify the total pressure of the gas phase and its composition in coexistence with the adsorbent. Using these parameters and an appropriate binary equation of state, fugacities of species in the mixture are obtained, and this is what is used as input in the simulations, formally corresponding to the (μ_1, μ_2, V, T) ensemble, where μ_1 and μ_2 are the chemical potentials of the two co-adsorbing species. As the total pressure of the bulk phase increases, the system undergoes a capillary condensation, similarly to a single component scenario. However, the equilibrium composition of the confined liquid-like phase may be different from the composition of the corresponding vapour-like phase, with this difference directly related to the width of the two-phase envelope. Both in bulk and under confinement, the width of the two-phase envelope should reflect the differences in thermodynamic properties of the fluids in the mixture, and species with a high relative volatility should form a wide two-phase region. For species of similar relative volatility (or, in other words close boiling points) this vapour - liquid envelope becomes narrow, and the differences in the compositions of the equilibrium vapour and liquid phases are small.

We note here that under conditions of interest the relative n-heptane - i-octane volatility barely deviates from one (1.04). The dew and bubble points of the bulk binary mixture with 0.89 mol fraction of i-octane are very close to each other at about 1.64 bar**,** and the composition of the gas phase is essentially the same as the composition of the liquid phase at these points. Given that confinement tends to shrink phase envelopes even further we should not expect any strong manifestations of the existence of the two-phase envelope for this system.

We now turn to the adsorption isotherms for this binary mixture at 390 K and pressures up 2 bar, which are shown in Figures 4.12 and 4.13.

There are several interesting trends to observe. Similar to the single component case, adsorption in a 10 Å pore corresponds to the capillary filling regime. In larger pores capillary condensation occurs in these systems at pressures close to the single

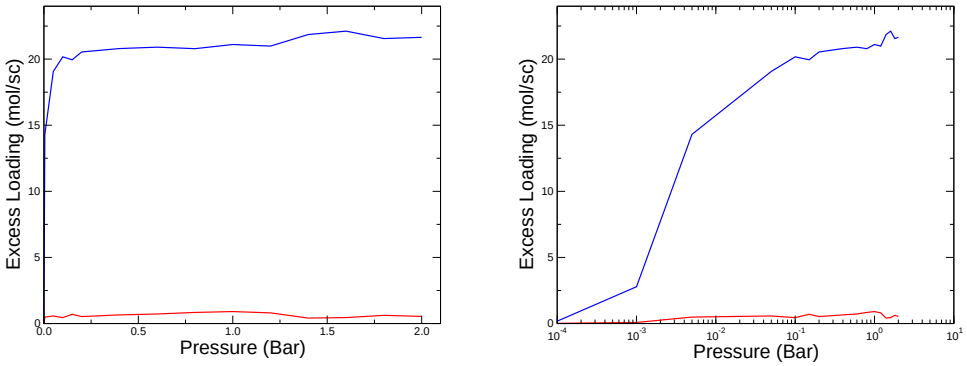

Figure 4.12: Adsorption isotherms for a binary mixture of n-heptane (red line) and i-octane (blue line) in a 10 Å slit pore at 390 K. The mixture corresponds to a 0.89 mol fraction of i-octane. Right panel shows the data using the logarithmic pressure scale.

component i-octane capillary condensation. This is particularly evident for the 40 Å pore, where capillary condensation occurs at a total pressure of 1.10 bar (1.13 bar for single component i-octane). For 40 Å, we also explore desorption hysteresis by reversing the adsorption process at high loading point. The hysteresis loop is observed for both species and the location of the desorption transition (0.89 bar) is somewhat lower than that for the single component i-octane desorption (0.988 bar). Again, we emphasise here that both adsorption and desorption transitions observed here for 40 Å pore are hysteresis transitions and neither of the branches corresponds to the true location of the confined vapour - liquid equilibrium.

Finally, we turn our attention to the main question posed in this section, which is whether there is a possible preferential adsorption of branched alkanes versus linear alkanes in carbonaceous slit pores. This behaviour is best characterised by adsorption selectivity:

$$S_{i/j} = \frac{x_i/x_j}{y_i/y_j} \tag{4.2}$$

where $S_{i/j}$ is the selectivity of species i (in this case, i-octane) over species j (in this case, n-heptane), and x and y indicate the mole fractions of the appropriate component in the adsorbed and gas phase, respectively. As has been already discussed, selectivity isotherms, even for simpler species such as methane and ethane, can exhibit a number of non-trivial effects associated with how molecules arrange

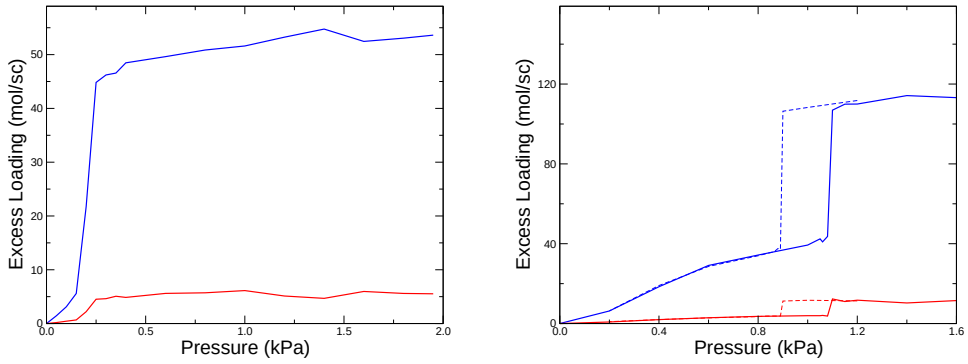

Figure 4.13: Adsorption isotherms for a binary mixture of n-heptane (solid red lines) and i-octane (solid blue lines) in a 20 Å pore (left panel) and a 40 Å pore (right panel) at 390 K. The mixture corresponds to a 0.89 mol fraction of i-octane. For 40 Å pore desorption, hysteresis is also shown via dashed red lines for n-heptane, and dashed blue lines for i-octane.

themselves in narrow slit pores. For the mixture considered here, this property is plotted in Figure 4.14. We also note here, that in order to improve statistics we consider $3 \times 3 \times 1$ replicas of the simulation system in the periodic boundary conditions for the 10 Å pore.

In larger pores, weak selectivity towards i-octane can be observed (despite some scattering of data, in 20 Å, it is 1.15 ± 0.13 and in 40 Å pore, it is 1.20 ± 0.10, averaged over the whole pressure range). However, in the smaller 10 Å pore there is a strong preferential adsorption of i-octane with selectivity more than three at lower pressures, and diminishing to about two at higher pressures. This is not unexpected given the single-component results shown in Figure 4.8: low pressures show stronger adsorption for i-octane (due to the additional carbon group) than n-heptane. At higher pressures i-octane is still more strongly adsorbed, but the difference between i-octane and n-heptane is reduced. The dramatic increase in selectivity in narrow pores of a certain range, compared to larger pores, is in agreement with the previous observations by Cracknell et al.[37] and Tan and Gubbins,[80] and our single component results for the 10 Å, pore.

Furthermore, the selectivity isotherm for 10 Å shows some features (maximum and then diminishing tail) of a Type I selectivity isotherm according to the Tan and Gubbins classification, but given the degree of scattering of the data, this requires

further investigation. This scattering arises due to poor statistics from very low loadings in the narrow 10 Å pore, despite the increased system size. Statistics could be improved by further increasing the system size and extending the simulation length considerably, however such simulations are beyond the scope of this research. It was not possible to apply the same root mean squared error analysis to the 10 Å pore due to the shape of the Type I selectivity isotherm. Alternative error analysis could include the analysis of individual pressure points on the isotherm, however further simulation would likely be required and is beyond the scope of this research.

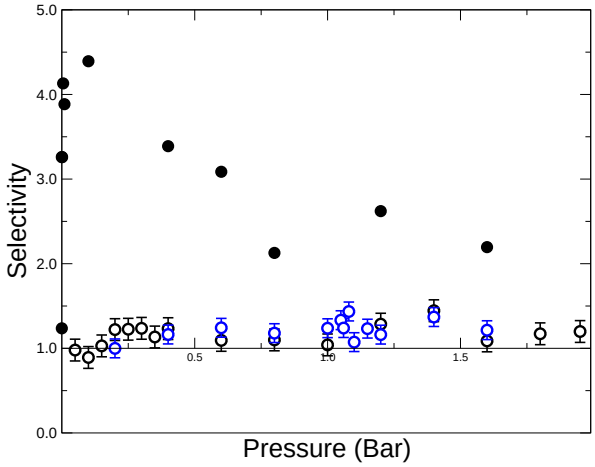

Figure 4.14: Selectivity adsorption isotherms for i-octane : n-heptane mixture at 390 K (composition of the mixture corresponds to 0.89 mol fraction of i-octane). Closed black circles are for a 10 Å pore, open black circles are for a 20 Å pore, and open blue circles are for a 40 Å pore. Root mean squared error bars are shown for 20 and 40 Å pores as black and blue lines respectively.

Let us link these observations to the previous studies in the field, in particular to the work by Calero et al.[82] on binary mixtures of n-pentane : i-hexane in silicalite, which is analogous to the n-heptane : i-octane mixture investigated here. Calero found a higher loading of i-hexane at low pressure, which was replaced with n-pentane as pressure was increased. In general, the high selectivity of i-octane over n-heptane in 10 Å pores is in agreement with these results, however in our studies we observe that even at higher pressures the 10 Å pores remain selective towards branched i-octane. This can be associated with several differences in the systems between the two studies. First, the i-octane used in our studies (2,4,4-trimethylpentane) has

three branched methyl groups, while the isomer used by Calero was only a mono-branched isomer of hexane. Second, in their work, Calero and co-workers studied the adsorption of alkanes on silicalite, which is different from the slit pore geometry studied here. Silicalite has been repeatedly shown to exhibit strong selective preference towards linear alkanes after a certain threshold loading (this occurs when the channel intersections are fully occupied; it is these intersections that favour the branched isomers). Finally, Calero studied the system at a temperature of 300 K, as opposed to our system which is at 390 K. The higher temperature will reduce the extent of adsorption, but we may speculate it should impact linear molecules more than branched due to the higher entropy change that flexible molecules undergo upon confinement.

In larger 20 Å and 40 Å pores it was expected from the previous studies and from single component isotherms that the n-heptane would replace i-octane at higher pressures due to more efficient packing. However, as seen in the figure above it is clearly not the case in the binary mixture system. This suggests that selectivity behaviour of the mixtures is a function of composition and the packing efficiency may not provide sufficient impact to reverse selectivity, at least when the linear alkane component is present in much lower concentrations, compared to the branched component.

Unfortunately, it is difficult to develop a fully conclusive picture from figure 4.12 due to the substantial scattering of the results, which arises from the nature of the system. Let us briefly elaborate on this. The 90 % i-octane 10 % n-heptane mixture presents a technical challenge for simulations. Since the number of n-heptane molecules in the system tends to be small, the selectivity calculated according to Equation 4.2 is prone to large statistical errors. Specifically, we estimate that for this 10 Å pore, the error in selectivity at lower pressures may reach up to 52 %. To explore the robustness of the selectivity trends and at the same time to secure a better statistics in estimation of the selectivity values, we extend these studies to 75 % : 25 % (by liquid volume at ambient temperature) mixtures of i-octane and n-heptane. Figure 4.15 (left) shows selectivity as a function of pore size for two different values of pressure on the isotherm at 420 K. A similar result at 390 K is shown on the right. Again, these results show a substantial degree of scattering (due to the sensitive nature of the property in question) and therefore we will attempt to summarise those trends that appear to be quite definite, while leaving more subtle features of the graphs below for further studies.

It is clear that there is a band of pores exhibiting very high selectivity towards i-octane (9 - 11 Å). It seems i-octane becomes geometrically incompatible with smaller pores and selectivity quickly drops to zero for pores smaller than 8 Å. In larger pores, there are two trends. At low pressure, the majority of larger pores seem to exhibit very weak selectivity towards n-heptane, however the degree of scattering does not allow us to assert this statement; at higher pressure very weak selectivity towards i-octane is observed (with selectivity only slightly above one), this effect is sufficiently pronounced for all pores and allows us to have some confidence in it. These trends are generally in agreement with Figure 4.14. One trend that is different from the previous observations is the decrease in selectivity in 10 Å pore as the pressure is increased at 390 K. This may require further investigation, using larger systems.

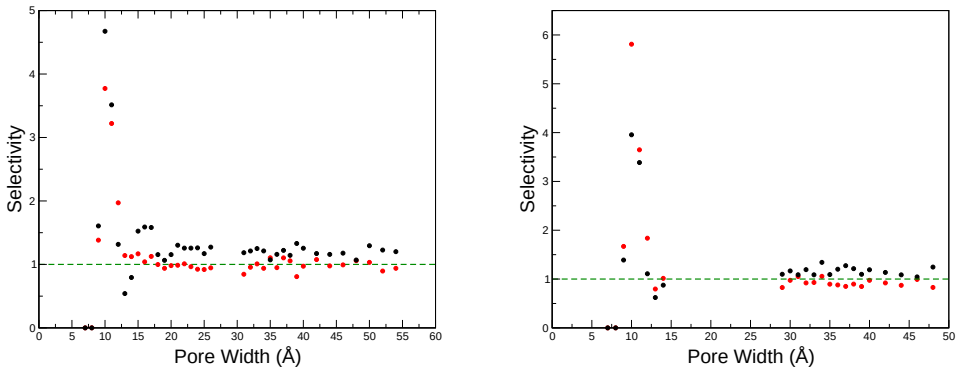

Figure 4.15: Selectivity of i-octane over n-heptane in a 75 : 25 (by liquid volume at ambient temperature) mixture at both 420 K (left) and 390 K (right) as a function of pore width for available pore sizes. Both high (3.6 bar for 420 K, 1.7 bar for 390 K) and low pressures (0.1 bar in both cases) are shown as black and red circles respectively. A selectivity value of one is shown as the green dashed line. Selectivity values above one indicate a preference for i-octane, selectivity values below one indicate a preference for n-heptane.

Finally, one result that seems peculiar is the sudden drop in selectivity towards i-octane at higher pressures in pores around 12.5 Å. This is associated with yet another type of packing effects. In the 9 to 11 Å range, both i-octane and n-heptane are able to form a single layer of molecules in the centre of the pore. As we have already discussed, on the interaction and packing grounds i-octane is preferred. At 12 Å, and for a small range above, n-heptane can form two layers, while the geometrically bulkier i-octane can still only form one layer in the pore centre. This is illustrated

using density profiles of the i-octane : n-heptane system, shown for 12 Å at 3.6 bar in Figure 4.16. The majority of i-octane molecules are confined to the centre of the pore, while a large proportion of the n-heptane are able to lie at the surface of each wall. This explains why a small band of pores slightly above 12 Å show a selectivity towards n-heptane.

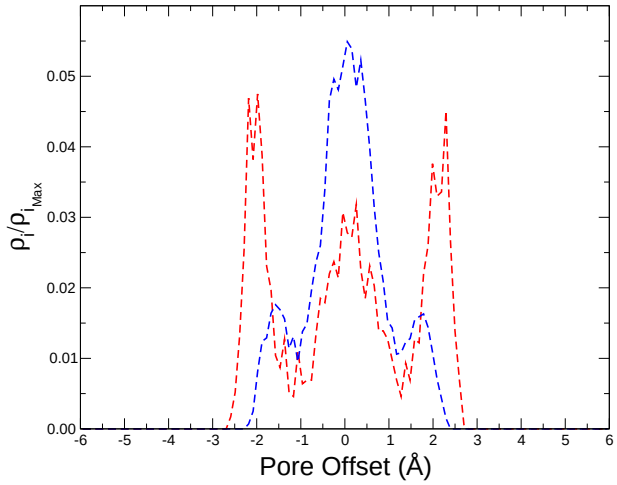

Figure 4.16: Density profiles for the binary mixture of i-octane (blue dashed line) and n-heptane (red dashed line) in a 12 Å pore at 3.6 bar. Iso-octane molecules mainly form a single layer in the centre of the pore, while n-heptane is able to form a double layer.

4.4 Isosteric Heat and Henry's Coefficients of Adsorption

In the previous section we broadly use the term "affinity" to describe the strength of the solid-fluid interaction. In this section the objective is to provide a more systematic quantification of this property. One option would be to calculate the average energy of interaction between the adsorbed molecules and the walls of the pore as a function of pore width. A property directly measured in the experiments is, however, isosteric heat of adsorption:

$$q_{st} = h_g - \bar{h_a} \tag{4.3}$$

where $\bar{h_a}$ is the differential enthalpy of adsorption, and h_g is the molar enthalpy of the gas phase. Without detailed derivations (for this, see Myers and Monson[91]), this general expression can be reduced into the following set of useful formula for calculating the isosteric heat of adsorption for zero loading of rigid molecules (Eqn. 4.4) and zero loading of flexible molecules (Eqn. 4.5)

$$q_{st} = RT - \langle U_{\text{solid-fluid}} \rangle \tag{4.4}$$

$$q_{st} = RT - \langle U_{\text{solid-fluid}} \rangle - \left\langle U^{\text{ads}}_{\text{intramolecular}} \right\rangle + \left\langle U^{\text{ideal}}_{\text{intramolecular}} \right\rangle \tag{4.5}$$

where $\langle U_{\text{solid-fluid}} \rangle$ is the average interaction energy between the pore and the adsorbing species, $\left\langle U^{\text{ads}}_{\text{intramolecular}} \right\rangle$ is the average intramolecular energy of the species under confinement, and $\left\langle U^{\text{ideal}}_{\text{intramolecular}} \right\rangle$ is the average intramolecular energy of the species in the ideal gas phase.

For non-zero loading it is common (and convenient in simulations) to replace the differential heat of adsorption with an expression based on the fluctuation theorem, which for rigid molecules (Eqn. 4.6), and flexible molecules (Eqn. 4.7) takes the following forms:

$$q_{st} = RT - \langle Fluctuation \rangle \tag{4.6}$$

$$q_{st} = RT - \langle Fluctuation \rangle + \left\langle U^{\text{ideal}}_{\text{intramolecular}} \right\rangle \tag{4.7}$$

where the fluctuation term is given by:

$$\langle Fluctuation \rangle = \frac{\langle UN \rangle - \langle U \rangle \langle N \rangle}{\langle N^2 \rangle - \langle N \rangle^2}$$

In this equation, U is an energy term comprising of all the solid - solid, solid - fluid and fluid - fluid interactions the adsorbed phase, as well as the internal interaction energy terms. The N term indicates the number of molecules, and the angled brackets indicate the ensemble average from the simulation.

Alternatively, the isosteric heat of adsorption could be calculated using the well known Clausius - Clapeyron equation:

$$q_{st} = -RT^2 \left[\frac{\partial \ln P}{\partial T} \right]_n \tag{4.8}$$

This approach requires several isotherms taken at different temperatures, which in the context of the present project proved to be very computationally intensive. A property closely related to the isosteric heat of adsorption is the Henry's coefficient of adsorption, defined as the initial slope of the adsorption isotherm:

$$\begin{aligned} K_H &= \frac{\rho}{P} \\ &= \frac{\ln(-\Delta g_{ads}/RT)}{RT} \end{aligned} \tag{4.9}$$

where ρ is adsorbed density ($^{\text{mol}}/_{\text{cm}^3}$ or $^{\text{mol}}/_{\text{g}}$) and Δg_{ads} is the Gibbs free energy of adsorption. An expression analogous to the Clausius - Clapeyron equation can be used to obtain zero loading isosteric heat of adsorption from the slope by plotting $\ln K_H$ vs $^1/_T$:

$$q_{st} = -RT^2 \left(\frac{\partial \ln K_H}{\partial T} \right) \tag{4.10}$$

The Gibbs free energy of adsorption and the isosteric heat of adsorption are also linked to each other via

$$\begin{aligned} \Delta g_{ads} &= \Delta h_{ads} - T \cdot \Delta s_{ads} \\ &= -q_{st} - T \cdot \Delta s_{ads} \end{aligned} \tag{4.11}$$

Using this equation in combination with Equation 4.9 allows us to write:

$$\Delta s = -\frac{q_{st}}{T} + R \cdot ln(RT \cdot K_H) \tag{4.12}$$

which is commonly used to calculate the standard entropy of adsorption.[83,91] This detour into thermodynamics of adsorption defined the necessary relations between the properties explored in this section.

Before presenting the results, we take this opportunity to introduce a third family of alkanes by using toluene to represent aromatic compounds. Aromatics make up a significant portion of standard gasoline fuels, and so a thorough investigation of adsorption effects on fuel composition requires their inclusion in these studies.

Studies for the adsorption of toluene on carbonaceous slit pores are scarce. More common are studies of other cyclic or aromatic species, such as benzene.[92,93] This

is motivated by the large interest in the removal of volatile organic compounds from emissions streams in industrial processes.[94,95] Many of these are studies on adsorption in other porous materials, such as zeolites[96,97] and activated carbons.[98,99] The lack of fundamental studies in the adsorption of linear, branched and cyclic species in slit pores provides an additional motivation for this section.

From these limited studies that are available, we can extract some general trends that are, to some degree, applicable to our problem. Klomkliang, Do and Nicholson compared the affinity and packing of benzene, toluene and *p*-xylene on graphitic surfaces and pores using computer simulations.[100] They found an order for the strengths of interaction, with xylene being higher than toluene, which was in turn higher than benzene. This was attributed to molecule side chains causing additional interactions. At higher loadings they found that the packing effects of the smaller molecules caused a reversal in this order. This is analogous to the trends found for linear alkanes[48,81,82] of different lengths, mentioned previously in this chapter.

A publication that is particularly relevant to our research is that of Fox and Bates, who looked at the adsorption of binary and ternary mixtures comprised of linear, branched and cyclic isomers of hexane.[101] This is one of the very few studies that directly compare linear, branched and cyclic alkanes, however this work was for the adsorption onto various zeolites. As such, interpretation of their results in the context of carbonaceous slit pores is difficult, as several trends in the adsorption behaviour were attributed to the interlacing of pores at particular pore junctions (i.e. geometry specific to a particular zeolite). However, one of the zeolites studied, $AlPO_4$-5, consists of straight unconnected channels, and so is arguably similar to the independent slit pore model we use. Fox and Bates found that in $AlPO_4$-5 the cyclohexane molecules are preferentially adsorbed over the normal and branched isomers on account of superior packing enabled by the more compact structure. This suggests that the structure of toluene could cause similar selectivity effects at higher loadings.

Below we present the results for the Henry's constants of adsorption and isosteric heat of adsorption for toluene, i-octane and n-heptane as a function of pore width, collected from the isotherms at 420 K.

4.4.1 Results

4.4.1.1 Henry's Constants of Adsorption

We begin the results section with the analysis of the Henry's constants of adsorption, which require only the initial slope of the corresponding isotherms and in that sense can be seen as a simpler property to obtain compared to the isosteric heat of adsorption. In Figure 4.17 Henry's constants of adsorption for single component systems of i-octane, n-heptane and toluene for both the micro and (lower) mesopore range are presented. The units of the constants are $\left[{}^{\mathrm{mmol}}/_{\mathrm{cm}^3\cdot\mathrm{Bar}}\right]$, consistent with the units of the adsorption isotherms in the kernel that we use by following the convention of Davies and Seaton.[71] Alternatively, units of $\left[{}^{\mathrm{mmol}}/_{\mathrm{cm}^2\cdot\mathrm{Bar}}\right]$ could be used. In general for pores greater than 11 Å, Henry's constants are larger for i-octane followed by n-heptane and toluene, although we note some scattering around 20 Å, which could be due to poor statistics and in principle should be investigated further. We note that, as we will see in the next chapters, deposits tend to feature bands of pores around 10 Å and 40 Å, so data for 20 Å is not as vital for the main objectives of the thesis. Behaviour in the narrow micropores is more complicated due to size exclusion effects of the larger molecules. Only toluene is able to comfortably fit in pores of 7 Å, n-heptane can fit in 7 Å pores, but this comes with an energetic penalty due to steric overlaps, so that the Henry's constant is very low. Iso-octane is unable to fit in any pores of 8 Å and below. We further note that in 10 and 11 Å pores, i-octane has substantially higher Henry's coefficients compared to toluene and n-heptane. This is consistent with the results in the previous section (i-octane vs n-heptane) and will have important repercussions in the context of the next chapters of the thesis. The general shape of the graphs below is consistent with the literature studies on the Henry's coefficients in slit pores.[102]

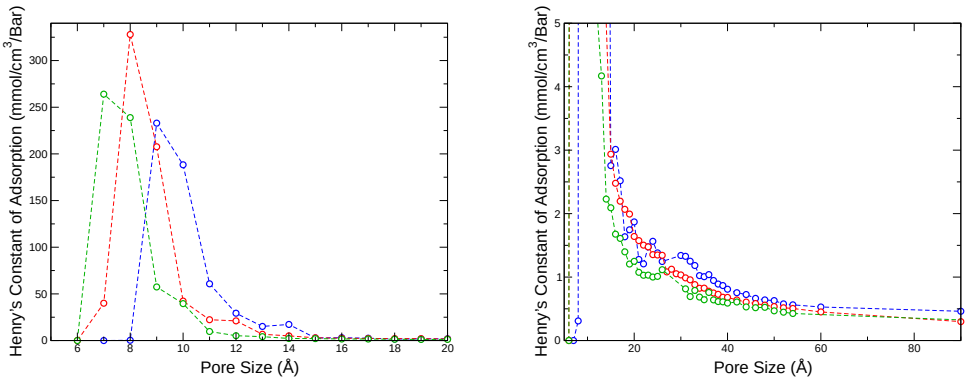

Figure 4.17: Henry's constants of adsorption as a function of pore width for the microporous range on the left, and mesoporous range on the right, both at 420 K. Blue dashed line with open blue circles shows i-octane, red dashed line with open red circles shows n-heptane and green dashed line with open green circles shows toluene.

4.4.1.2 Isosteric Heats of Adsorption

Figure 4.18 shows the isosteric heats of adsorption for single-component systems of n-heptane, i-octane and toluene as a function of pore width at four representative levels of loading. These include zero loading (a single molecule in a slit pore), low loading (0.1 bar), medium loading (0.5 bar) and high loading (~2 bar).

The first panel of Figure 4.18 shows the zero loading isosteric heat of adsorption, which corresponds to a single ideal gas molecule of adsorbate interacting with the walls of the pore. In this figure the blue dashed line shows the strength for i-octane, the red for n-heptane and the green for toluene, this colour scheme is adopted throughout the thesis. At larger pore widths (20 Å and above), the average interaction energy corresponds to the energy of a molecule interacting with a single wall. In this situation, toluene has the weakest interaction with the isosteric heat equal to 24 kJ/mol, i-octane has a value of 25 kJ/mol and n-heptane is the most strongly attracted with the isosteric heat of adsorption equal to 27 kJ/mol.

It is interesting to note that Figure 4.17 shows that in larger pores, the Henry's constants of i-octane are higher than those of n-heptane. However, the zero-loading isosteric heats of adsorption in Figure 4.18 show n-heptane is more strongly attracted in this region of pore size. To understand this, consider the following. From Equation 4.9 we see that the Henry's constant is dependent on the Gibbs free energy

of adsorption, Equation 4.11. From this equation, we can see that the Gibbs free energy of adsorption is not only dependent on the isosteric heat of adsorption, but also the entropy change upon adsorption. Upon confinement, the linear n-heptane molecules experience a greater reduction in degrees of freedom than the rigid i-octane molecules, causing the Henry's constants for i-octane to exceed those for n-heptane. The entropy of adsorption can be calculated using Equation 4.12, and these results are shown in Figure 4.19 for i-octane, n-heptane and toluene as a function of pore-width. The entropy of adsorption was calculated using the accessible volume, as defined earlier in the chapter. From these results, it can be seen that while the change in entropy for i-octane and toluene are similar, that of n-heptane is greater due to the flexibility of the molecules. This effect is observed even for larger pores where the entropy reduction must be associated with the molecules located in the vicinity of the wall. The reduction of entropy penalty for all three species from very small pores to 10 - 15 Å pores is fairly intuitive to understand. What one may find puzzling is the continuous slow reduction of the entropy penalty as the pore width increases. This is associated with the definition of the standard state. In the calculations above, this was implicitly taken as a bulk system with a volume equal to the accessible volume of the simulation system, containing 1 mole of ideal gas. As the system increases in volume, the isosteric heat associated with the interaction with the walls remains almost constant, while the molar entropy of the standard state constantly increases. This leads to gradual increase in the absolute value of the standard entropy of adsorption which manifests itself in the diminishing value of the Henry's constants of adsorption as the pore width increases.

The differences in behaviour between linear and branched alkanes are in line with previous publications from the literature,[83] and provide evidence for the previously noted hierarchy difference between isosteric heats and Henry's constants.

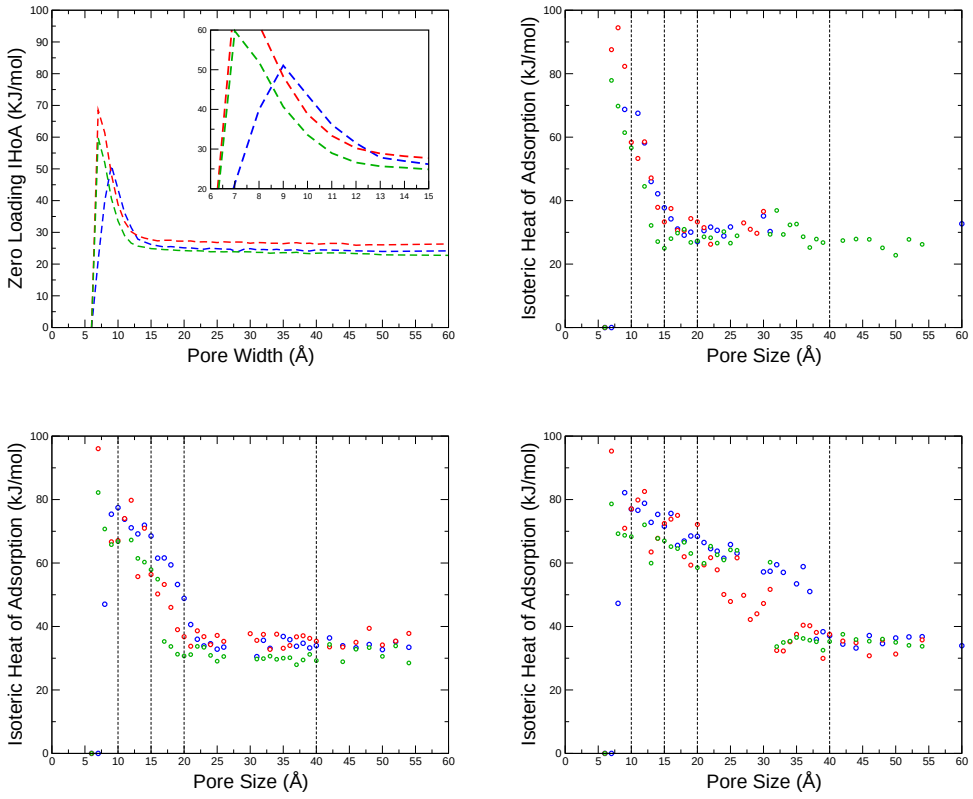

Figure 4.18: Isosteric heats of adsorption for single-component systems as a function of pore width at 420 K. Each panel represents a different degree of loading, and in each case i-octane is represented in blue, n-heptane in red and toluene in green. The top-left panel shows energies at zero loading; the energy of a single molecule is considered in each pore. In this panel isosteric heats of adsorption for each species are represented as dashed lines. Panels in the top-right, bottom-left and bottom-right show isosteric heats of adsorption at 0.1 bar, 0.5 bar and ~2 bar respectively (2.12 bar for n-heptane, 2.0 bar for toluene and 2.13 bar for i-octane). Data points for these three panels are represented by open circles. The dashed vertical lines (dark green) indicate example pores for which pressure profiles are shown in Figures 4.20 and 4.21.

For pores that are narrower than 13 Å the situation is more complex. Consider i-octane, the interaction energy becomes stronger as the pore size becomes smaller, with the i-octane now interacting with both walls of the pore. However, again at around 9 Å it becomes difficult for i-octane to fit in the pore and the interaction energy quickly becomes less favourable with the isosteric heat of adsorption exhibiting a sharp drop. In contrast to this, both n-heptane and toluene also experience

the increasing attraction strength as the pore narrows, however they can both fit in pores of 7 Å with no energy penalties. In the region between 8.5 Å and 13 Å, i-octane interactions are stronger (more favourable) than n-heptane interactions with the slit pores, and n-heptane interactions are stronger than toluene. We will return to the realism of this situation later in the section.

The remaining panels of Figure 4.18 show the isosteric heats of adsorption at different loadings, calculated using fluctuation theory. Naturally, in agreement with the previous studies these results show a much greater degree of scattering and only general observations can be made. The case of low loading (0.1 bar) strongly resembles that of zero loading. As the pressure is increased the curve of isosteric heat, as a function of pore size, shifts to the right (at higher pressures wider pores have higher heats of adsorption than at low pressures) and becomes more linear in the decrease. The trends shown in the figures below are expected: as the pressure is increased, an additional contribution to the interaction energy comes from the fluid-fluid interactions, leading to an increased isosteric heat of adsorption throughout the pore range. This effect is not significant for very narrow pores, which reach adsorption capacity at very low pressures, while molecules do not benefit as much from fluid-fluid interactions due to geometrical constraints, however it is substantial for mesopores undergoing capillary condensation.

To take a closer look at how isosteric heats of adsorption vary with pressure, values for each species in individual pores (represented as the dashed dark green lines in Figure 4.18) are shown in Figure 4.20 and 4.21. Profiles in selected micropores (10 Å and 15 Å) are shown in Figure 4.20. At zero loading, the 10 Å pore is within the range where i-octane is more strongly attracted to the pore walls than n-heptane (see Figure 4.18, first panel). This is reflected by i-octane having a higher isosteric heat of adsorption, and is also true at higher pressures (and so higher loading). Toluene has the lowest values for all pressure ranges considered, and n-heptane lies between i-octane and toluene.

An interesting feature found in Figure 4.20 is the minimum in i-octane heat of adsorption around 10^{-4} bar. As this effect was discovered rather late in the project, the data is not available for toluene at these low pressures, and the data for n-heptane is insufficient to determine if these species also follow the trend in 10 Å pores (most likely they will and this is to be further investigated). However, in a 15 Å pore n-heptane shows a similar minimum and sharp rise in isosteric heats of adsorption, and the limited data for toluene suggests similar behaviour. We know

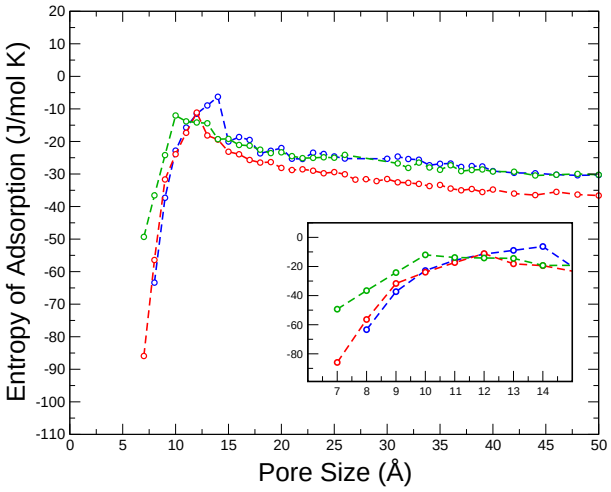

Figure 4.19: Standard entropy of adsorption as a function of pore width for i-octane (blue line, open circles) n-heptane (red line, open circles) and toluene (green line, open circles). Results were calculated using the accessible pore volume.

that at zero loading (Figure 4.18) n-heptane should have higher heat of adsorption than i-octane in pores larger than 13 Å. Trends shown in Figure 4.18 indicate this is not the case for higher loading, most likely due to stronger i-octane fluid-fluid interaction. However the high degree of scattering makes this conclusion uncertain.

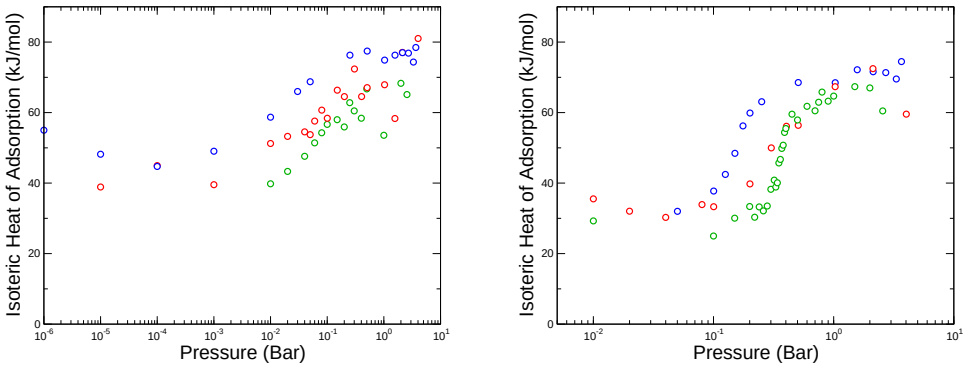

Figure 4.20: Isosteric heats of adsorption for single-component systems in a 10 Å (left) and 15 Å (right) pore as a function of pressure at 420 K. Species shown include i-octane (blue open circles), n-heptane (red open circles) and toluene (green open circles).

Figure 4.21 shows how isosteric heats of adsorption vary in selected mesopores as pressure is increased. The two pores selected are 20 Å (on the left) and 40 Å (on the right) pores. Also included are the excess loadings of each species in the appropriate pores, shown in arbitrary units. By comparing the excess loading to isosteric heats it is immediately clear that as the loading increases, the isosteric heats of adsorption for each species increases. In both cases it can be seen that capillary condensation of a species causes an associated step-increase in adsorption energy.

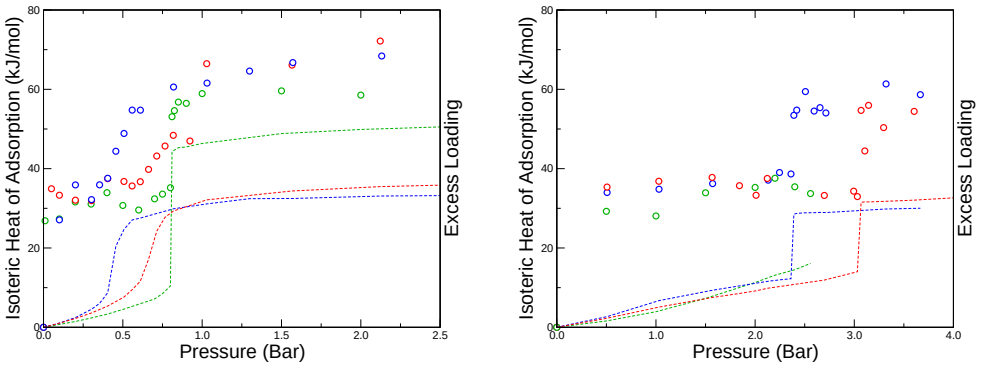

Figure 4.21: Isosteric heats of adsorption for single-component systems in a 20 Å (left) and 40 Å (right) pore as a function of pressure at 420 K. Isosteric heats of adsorption for species shown include i-octane (blue open circles), n-heptane (red open circles) and toluene (green open circles). Excess adsorption isotherms are also included for i-octane (dashed blue line), n-heptane (dashed red line) and toluene (dashed green line) to highlight association between capillary condensation and step-increases in isosteric heats of adsorption. Units for the excess adsorption loading are arbitrary.

4.5 Discussion and Conclusions

In this chapter we investigated adsorption of linear, branched and aromatic alkanes in slit pores from two different perspectives. Firstly, we wanted to compare adsorption of branched alkanes with linear alkanes to understand the effect of branching. For this we compared single component adsorption isotherms for n-butane and i-butane; and n-heptane, n-octane and i-octane in slit pores of 10, 20 and 40 Å. A particularly novel aspect of this study is a direct simulation of mixtures of branched and linear alkanes related to the objectives of the thesis. Specifically, adsorption isotherms

for the binary mixtures of n-heptane and i-octane in slit pores of 10, 20 and 40 Å were analysed. Secondly, we wanted to characterise the strength of interaction of the alkane species with the slit pores of different size. For this, Henry's constants of adsorption and isosteric heats of adsorption for single-component systems of n-heptane, i-octane and toluene were presented. The results can be summarised as follows.

Depending on the pore size, capillary filling and capillary condensation mechanisms of adsorption take place for n-heptane, n-octane and i-octane. Capillary filling was also observed for n-butane and i-butane, however no clear capillary condensation was observed for these species. This is likely because the temperature of the system was close to the critical temperatures of the adsorbing species. In contrast, adsorption isotherms for larger alkanes in 40 Å pores exhibit a pronounced hysteresis loop. The adsorption preference of normal and iso-butane showed inverse shape selective behaviour in the small pore (10 Å) and shape selective behaviour in the larger (20 and 40 Å) pores. The transition between inverse shape selectivity and shape selectivity was observed for n-octane and i-octane in the 10 Å pore, suggesting that pores smaller than 10 Å should exhibit inverse shape selection, and pores larger than 10 Å should exhibit shape selection between the octane isomers, and this indeed was observed for 20 and 40 Å pores. These trends, and their high dependence on pore width, have been previously reported in the literature.

Binary mixture adsorption studies revealed a preference for the adsorption of i-octane over n-heptane in narrow pores at all pressures considered, and larger pores at higher pressure. Larger pores at low pressure showed a weak selectivity towards n-heptane. This contradicts both single component results *and* Henry's constants of adsorption for single components and must be associated with effects associated specifically with mixtures. In smaller 9 - 11 Å pores, the selectivity of i-octane over n-heptane is dramatically enhanced due to the overlapping interaction projected by the pore walls. However, in 7 and 8 Å pores the system becomes infinitely selective towards n-heptane simply because i-octane does not fit any more due to steric overlaps. This suggests that accurate characterisation of engine deposit structure (the porosity and PSD) is important in assessing their overall impact on the performance of the engine via selective adsorption mechanism.

Results associated with the energy of adsorption in slit pores show a substantial degree of scattering and therefore here we will try to derive conclusions on the trends that are fairly certain, while admitting that some aspects of this study may require

further research and better statistics. The Henry's constants for adsorption, at a representative temperature of 420 K, were calculated as a function of pore width for n-heptane, i-octane and toluene. Generally speaking, i-octane was found to have the highest values across all pores, followed by normal heptane, while toluene was consistently the lowest. There are two exceptions to this trend: very narrow pores of 8 Å and below show a significant drop in the Henry's constants of adsorption for i-octane. Values around 20 Å also show a small range of pores where i-octane has lower values than n-heptane. The latter of these is suspected to be an artefact of poor statistics rather than a change in trend, however the former is due to size exclusions effects severely reducing the adsorption of i-octane in pores of 8 Å and below. The Henry's constant for n-heptane in 7 Å pores also show a significant decrease, indicating that there could be some size exclusion effects here too.

At low loadings, isosteric heats of adsorption show varying orders of adsorption strength as pore width decreases. Larger mesopores show the order of adsorption strength to be n-heptane > i-octane > toluene. For micropores in the range 8.5-13 Å, i-octane was found to have the highest interaction energy. As the pore width decreases further, size exclusion effects come into play and the interaction energy for i-octane drops significantly. Normal heptane and toluene are unaffected by size exclusion effects until the very narrow 6 Å pore. For n-heptane, this is contrary to the Henry's constants for adsorption, which show a significant drop for 7 Å pores. This is due to a greater change in entropy for the more flexible n-heptane molecule, compared to the rigid toluene. This manifests, via the Gibbs free energy, in the Henry's constant of adsorption, but not in the isosteric heat of adsorption. At higher pressures, trends in the order of adsorption strengths are harder to measure due to scattering in the statistics.

An interesting observation is a lower adsorption energy for toluene compared to n-heptane. One might speculatively expect a favourable contribution from pi-pi interactions between aromatic toluene and graphene layers, leading to an enhanced interaction of aromatic species compared to their linear analogues. Here this is not the case, with toluene exhibiting the weakest interactions with the slit pores out of all three species. This asks the question: is this result an artefact of the force field or a true reflection of the relative interaction strengths?

Firstly, from the literature it seems unclear whether the affinity of aromatic compounds is greater than linear compounds, or vice versa. While direct comparisons of toluene to linear hydrocarbons are rare, benzene has been regularly investigated,

and Klomkliang and co-workers have shown that adsorption between toluene and benzene is similar[100] and so consideration of benzene versus linear alkanes is a useful substitute. Matsumoto et al. investigated adsorption behaviours of linear, branched, cyclic and aromatic hydrocarbons on activated carbon fibers containing slit-shaped micropores. They estimated the isosteric heats of adsorption from the Dubinin - Radushkevich plots and found the isosteric heat of adsorption for benzene to be lower than both n-hexane and n-octane for pores less than 10 Å. On the other hand, the same study showed calorimetric measurements of the differential heats of adsorption which show benzene has lower heats of adsorption than both n-octane and n-hexane in the smallest pores considered (7 Å), but in wider pores it seems benzene has higher heats of adsorption compared to linear alkanes. Other experimental results come from Sato and co-workers,[103] who investigated the surface fractal dimension of activated carbon fibers. They looked at adsorption of n-heptane and benzene, as well as other species, on two particular activated carbon fibers. From their unpublished results we were able to plot the experimental isotherms, and consequently determine the Henry's constant of adsorption and found that of benzene to surpass n-heptane in both cases. These experimental isotherms, as well as details on the activated carbon fiber formation, are provided in Appendix D. These results are contrary to the findings of Isirikyan and Kiselev,[104] who compared adsorption isotherms and differential heats for benzene and n-hexane. A comparison of differential heats at low loadings show higher values for hexane ($\sim$12 $^{\text{cal.}}/_{\text{mole}}$) than benzene ($\sim$10 $^{\text{cal.}}/_{\text{mole}}$) on various graphitised carbon blacks.

Secondly, a more accurate picture could probably be obtained from quantum-mechanical analysis of the interactions between different types of hydrocarbon species and graphene layers. This is however beyond the scope of the thesis. For the practical purposes we simply keep in mind that adsorption of aromatics can be stronger and more favourable than what is seen with the current model. This argument will be used in the analysis of the effect of engine deposits on the function of the engine.

The next chapter, Chapter 5, provides the link between adsorption in individual slit pores, and adsorption in a porous material of variable pore size by considering the application of the Adsorption Integral Equation. The characterisation process is revisited with the systematic improvement of input simulations, leading to the changes in pore size distributions from those originally reported by Costa et al. The effects of these changes are also explored in detail.

Chapter 5

From Single Pore to Collective Behaviour: Systematic Generation of Adsorption Kernels and Pore Size Distributions for a Predictive Adsorption Model

5.1 Introduction

This thesis is the latest contribution in the ongoing investigation of engine deposits and their adsorption interactions with gasoline fuel components. In Chapter 3 we outlined the initial advances made by Costa and co-workers in this field. The cornerstone of their work was the development of a molecular model able to capture the adsorption behaviour in engine deposits. The model was used to demonstrate, for the first time, that in the equilibrium limit deposits should adsorb substantial amounts of fuel components under temperature conditions relevant for engine operation.

The extent of this adsorption is largely influenced by the internal structure of the porous material. A significant achievement of Costa's model was the ability to characterise the internal structure of engine deposits using only one experimental adsorption isotherm and a kernel of simulated isotherms. A large proportion of the early efforts was invested in overcoming various challenges associated with this

characterisation, including the range of pores to be considered and a description of solid-fluid interactions. The sensitivity of the model to other parameters was invariably left outside of the original scope. In particular, there was some concern that the simulated kernels were too coarse in terms of the number of points within a single isotherm and the number of isotherms within the kernel. It was not clear how increasing the resolution of the kernels would affect the PSD or the predictions for adsorbate species of interest.

An early objective of the current project was to identify where these kernels could be improved, how increasing their resolution changes estimates for the pore size distribution, and how this in turn alters the predicted adsorption isotherms. As the resolution of the kernel is intimately linked to other aspects of the protocol involved in the inversion of the AIE, this effectively led to revisiting the parameters of the whole protocol on a more systematic basis. Tackling this objective, and other issues associated with the robustness of the model, is the focus of the current chapter and can be seen as a necessary and logical step between adsorption in individual slit pores, addressed in Chapter 4, and investigating the adsorption of fuel component mixtures in porous engine deposits, addressed in Chapter 6.

5.2 Concerns with the Original Kernel of Adsorption Isotherms

To begin, we first explore concerns associated with the original kernel of adsorption isotherms by Costa et al. The adsorption kernels are used in two areas of the predictive model. The first is in the generation of the pore size distribution during the characterisation step. Here a kernel of simulated adsorption isotherms is used in conjunction with the experimental data to invert the Adsorption Integral Equation and obtain a PSD which produces the best fit (as probed by several alternative methods) to the reference experimental points. The second area is in predicting the adsorption of more complex species and mixtures. Here, the behaviour of species in individual slit pores is captured in the adsorption kernel, which is then used in conjunction with the developed PSD to predict the overall adsorption isotherm. We address the concerns associated with each use of the kernel separately.

5.2.1 Kernels used in Pore Size Distribution Generation

To understand why we believe the resolution of the kernels must be improved (compared to the original study) and how these improvements can be made, let us first briefly review how the adsorption kernels used in the AIE are constructed. As mentioned in Chapter 2 (Section 2.4), solving the AIE uses a matrix approach in line with the methods of Davies and Seaton.[41,42] Specifically, the protocol for the generation of the most reliable PSD requires that the number of quadrature intervals (or equivalently, number of the isotherms in the kernel separated from each other by a fixed increment in pore width) m must be equal to the number of pressure points in the experimental and simulated isotherms, n. Thus, it seems that the limiting and decisive factor in the resolution of the kernel and simulation isotherms is the number of experimental points, which is typically small, due to the time-consuming nature of experimental measurements. Attempting to obtain a PSD using a larger number of quadrature intervals than the number of experimental points available (i.e. $m > n$) would be equivalent to increasing the number of free parameters in solving an optimisation problem: this leads to multiple alternative solutions, each of which fit the original data. This leads to the question: is our pursuit of more detailed adsorption kernels technically incompatible with the requirements of the protocol (i.e. $n = m$)? In practice this problem is circumvented by interpolating between the experimental points, using for example cubic spline functions as has been done in the work of Costa and co-workers, or other methods that have been used in the literature.[105] It cannot be over-emphasised that as a result we develop a simulation model to fit a *hypothetical* isotherm with artificially increased number of points, rather than the true experimental data; and the accuracy of the model can only be asserted by predictive studies of other conditions and species.

Now, with a lifted restriction on the number of quadrature intervals available, let us return to the generation of the isotherms in the kernel. Although not to the same extent as the experimental efforts, simulations can also be limited in how detailed they are due to constraints on resources, and in particular the available computational time and researcher's time to collate the data. In practice only a limited number of isotherms are simulated, and on each isotherm only a limited number of points can be considered, although both of these tend to be much higher than in experimental procedures.

In order to obtain the number of points on the isotherms matching the interpol-

ated "experimental" isotherm, simulation results are also interpolated (using linear interpolation, if we follow the approach adopted previously in Seaton's group). In order to obtain the required number of isotherms in the kernel (also matching the number of points in the isotherms), linear interpolation in density is applied for the quadratures between the available isotherms. Hence, the technical question arises: how do we select the set of isotherms to be used to generate the kernel of interpolated isotherms, and how do we select the pressure points for these isotherms?

For the first part of this question, we naturally want to consider pores where adsorption takes place via either capillary filling or capillary condensation. Very large pores experience accumulation of the molecules near the walls only and therefore, it is impossible to differentiate between two large pores - their contribution to the overall adsorption is the same. In the terminology of Gusev and O'Brien these pores are beyond the window of reliability.[32] For the pores in the region associated with capillary filling and condensation, we may want to have more isotherms where transition from capillary filling to capillary condensation regimes takes place to ensure smooth interpolation between two distinct shapes of the isotherm. Similarly, for the values of the pressure on the adsorption isotherm we are interested in correctly capturing the essential features of the isotherm. From this perspective, having more points in the plateau region of the isotherm following capillary filling process is not essential. On the other hand, the step on the isotherm associated with capillary condensation may benefit from a better resolution.

Consider now the adsorption isotherms for ethane at 278 K, used to construct the kernel in the original studies of Costa and co-workers. For these, they simulated the following set of isotherms: from 6 to 20 Å in intervals of 1 Å; from 20 to 100 Å in intervals of 10 Å; from 100 to 200 Å in intervals of 20 Å; additional isotherms at 240, 280, 300, 340, 380, 400, 440 and 480 Å; and finally from 500 to 800 Å in intervals of 100 Å. These isotherms are shown in the top graphic of Figure 5.1. For the construction of the kernel, 500 quadratures and 255 pressure points were used. The upper bound of pore size was set as $w_{upper} = 700$ Å. The resulting kernel (obtained through both interpolation between the isotherms and pressure points) is shown in the bottom graphic of Figure 5.1. The actual points on the isotherms are not shown: as the interpolation is linear they simply sit on line segments, connecting points that are interpolated from the upper graph.

Comparison of the two graphs in Figure 5.1 reveals some interesting points that should be noted. It seems that, in the capillary filling regime, the resolution of the

interpolated isotherms is actually worse (there are fewer isotherms) than the original data. This is because interpolation forces the isotherm quadratures to take regulated intervals, which is determined by the total pore range divided by the number of quadratures required. As a result, two simulated isotherms in the capillary filling separated by 1 Å may fall into the same quadrature leading to just one isotherm in the actual interpolated kernel. So a consequence of having such a large pore range is a loss of interpolated resolution at very low pressures. Another oddity in the lower graph is the adsorption isotherm that plateaus between 5 and 6 $^{\mathrm{mmol}}/_{\mathrm{cm}^3}$. The first quadrature has a width of $\frac{700-6}{500-1} = 1.39$ Å. This means the isotherm accounts for all the adsorption that occurs in pores between the sizes of 6 Å and 7.39 Å, and this is approximated by a single isotherm in the centre of this range, 6.7 Å. The isotherm plateauing $\sim 5.5^{\mathrm{mmol}}/_{\mathrm{cm}^3}$ is an interpolation between the 6 Å pore, which has zero loading at all pressures, and 7 Å pore.

A careful analysis of the original results pointed to the following issues. Firstly, from the ethane adsorption isotherms (Figure 5.1, upper), it is evident that there are substantial gaps of data that cause problems when constructing the adsorption kernel. A lack of simulated isotherms for pores in the lower mesoporous range cause interpolation between isotherms in this region to be invariably crude. Furthermore, individual adsorption isotherms feature a limited number of points (in fact only seven at the same seven values of pressure regardless of the type of isotherm), making interpolation along the isotherm also crude. This is particularly evident for isotherms in 20, 30 and 40 Å pores, shown in red, featuring large steps in density associated with capillary condensation.

Finally, the originally proposed pore range between 6 and 800 Å seems excessive, as the majority of the pores in this region should lie beyond the window of reliability. In Figure 5.1 we use blue colour for the isotherm of 80 Å. It already has essentially a linear shape, characteristic for the pores beyond the window of reliability, and all pores of larger size are therefore beyond this window and their consideration is not needed. All the issues outlined above provide a motivation to revisit the process of going from adsorption in single pores to adsorption in the whole material sample on a more systematic basis with a view to establishing consistent parameters for the protocol.

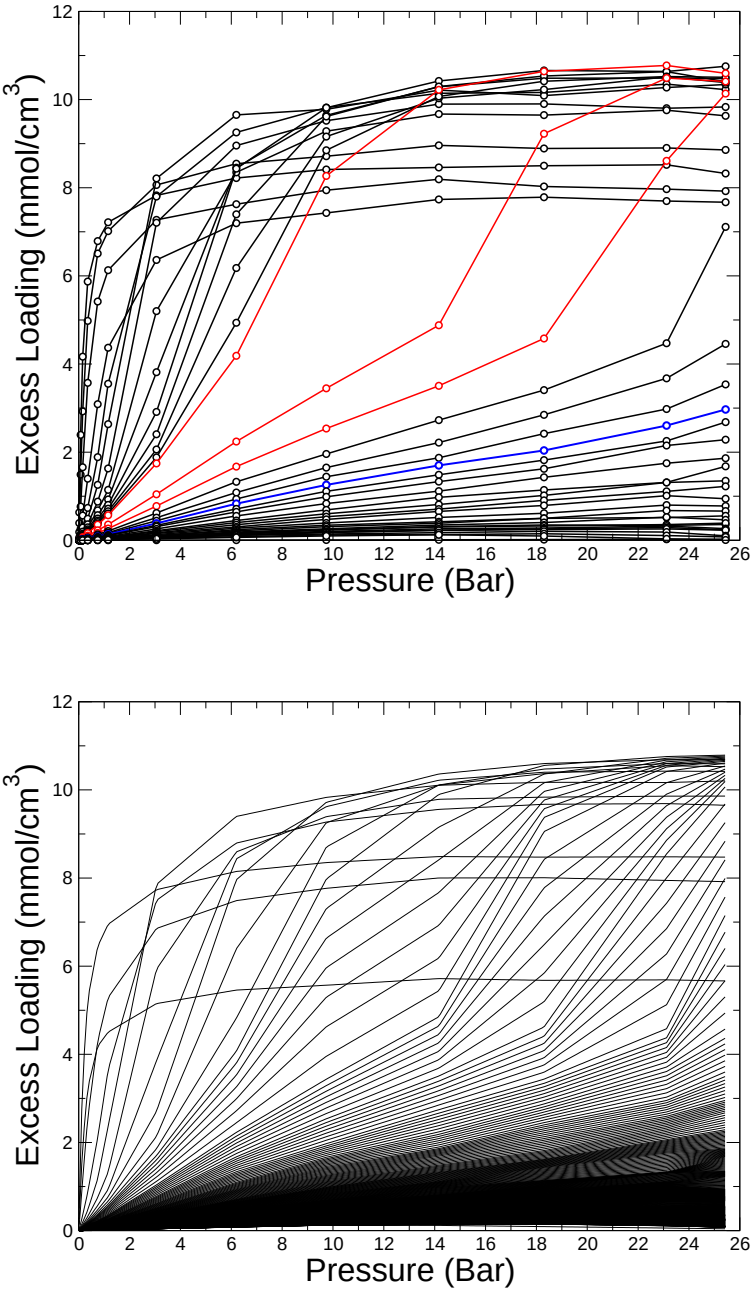

Figure 5.1: The graph at the top shows the set of adsorption isotherms used for the construction of the original ethane kernel at 278 K. Open circles depict simulated pressure points, lines are to guide the eye. Pores highlighted in red are, from left to right, pore widths of 20, 30 and 40 Å. The isotherm highlighted in blue is the 80 Å pore, and shows a reasonable threshold above which adsorption isotherms become linear within this pressure range. Interpolation between the simulated isotherms allows the construction of the ethane kernel, which is shown on the bottom. Interpolated pressure points are not shown. This kernel was used by Costa et al. in the original characterisation of both CCD and IVD.

5.2.2 Kernels used in Adsorption Prediction

When predicting adsorption in systems, the adsorption kernel is treated slightly differently than during PSD characterisation. Although technically each isotherm is required to form the matrix, detailed behaviour of each quadrature isotherm is not strictly necessary. The nature of the AIE process collates the adsorption contribution of individual pores, weighted by the presence of those pores on the PSD. If a specific pore is not found on the PSD, then the isotherm of that quadrature will have no impact on the overall adsorption. With this in mind, it is possible to increase efficiency when generating adsorption isotherm sets by prioritising simulations for pores that are known to be present in the chosen PSD. Of course, this approach of prioritising certain pores is not possible during characterisation as the pores present on the PSD are not known *a priori*.

Let us now focus on the predictive aspects of the model, the construction of the kernel, and how the original isotherms sets could be improved. As an example, we explore the original adsorption isotherms used by Costa and co-workers in the the prediction of n-heptane on CCD at 420 K, shown i the top graphic of Figure 5.2. Again, to reiterate the definition of the adsorption kernel, each isotherm represents the excess loading of n-heptane in a pore of a particular width. The kernel is constructed from the available set of isotherms using the same two-stage process. The required number of isotherms is generated by splitting the region of pore widths into N quadratures and interpolating between the available simulated isotherms in Figure 5.2. The accuracy of this process depends on the number and distribution of the simulated adsorption isotherms. The second step is to standardise the number of pressure points on each isotherm; again using interpolation between pressure points on the same isotherm. The accuracy of this process depends on the original number of points within the isotherm.

In Figure 5.2, the isotherms highlighted in blue correspond to those pores which are found on the original PSD for the CCD structure. Similar to the concerns with the ethane isotherms, both the number and quality of individual isotherms is lacking. For example, a substantial proportion of pores in the isotherm set are not present in the original PSD for CCD. This is more clearly emphasised by the lower graph of Figure 5.2 showing the PSD for CCD overlayed with the set of n-heptane isotherms, indicated by vertical green lines. For the reasons mentioned above, information from many of these isotherms has no impact on the adsorption

of the porous material. Conversely, pore sizes between 40 and 50 Å, a range that contains a substantial proportion of pores in the CCD structure, are not present in the isotherm set. Instead, isotherms for these pores need to be interpolated from the 40, 50 and 60 Å pores, a process which is bound to provide only a crude approximation of the intermediate isotherms. Our understanding of the adsorption processes in this structure would benefit from a more detailed picture of behaviour in pores between 40 and 50 Å.

Examination of Figure 5.2 shows the second problem with the isotherm set: each isotherm consists of the same seven pressure points, regardless of the pore region they are associated with. Furthermore, four of these seven points are at pressures below 0.5 bar. For pores in the mesoporous range (20 to 500 Å) these chosen pressures are not appropriate to correctly capture the capillary condensation shape of isotherms in this pore range. From Figure 5.2, we can see that pores of 40, 50 and 60 Å undergo the capillary condensation transition somewhere between the pressure points at 1.2 bar and 3 bar, but exact locations are not known. The pressure at which capillary condensation occurs decreases as the width of the pore decreases. This is due to interaction forces between the adsorbing species and the walls being felt more strongly due to the decreased distance. With an insufficient number of pressure points, it is impossible to accurately capture this behaviour, transition in density, and shape of the isotherm. From the current set of adsorption isotherms, the model has no way to individually differentiate the position of the condensation points for the 40, 50 and 60 Å pores. A more systematic approach would tailor the values of pressure points examined to the pore in question, recognising the differences between the mesoporous range and pores undergoing capillary condensation, and the microporous range and pores exhibiting capillary filling.

These are the main concerns that emerged upon re-examination of the results by Costa et al. How these problems were addressed is outlined in the next sections, where we discuss generation of new sets of adsorption isotherms and kernels, as well as the PSDs associated with them.

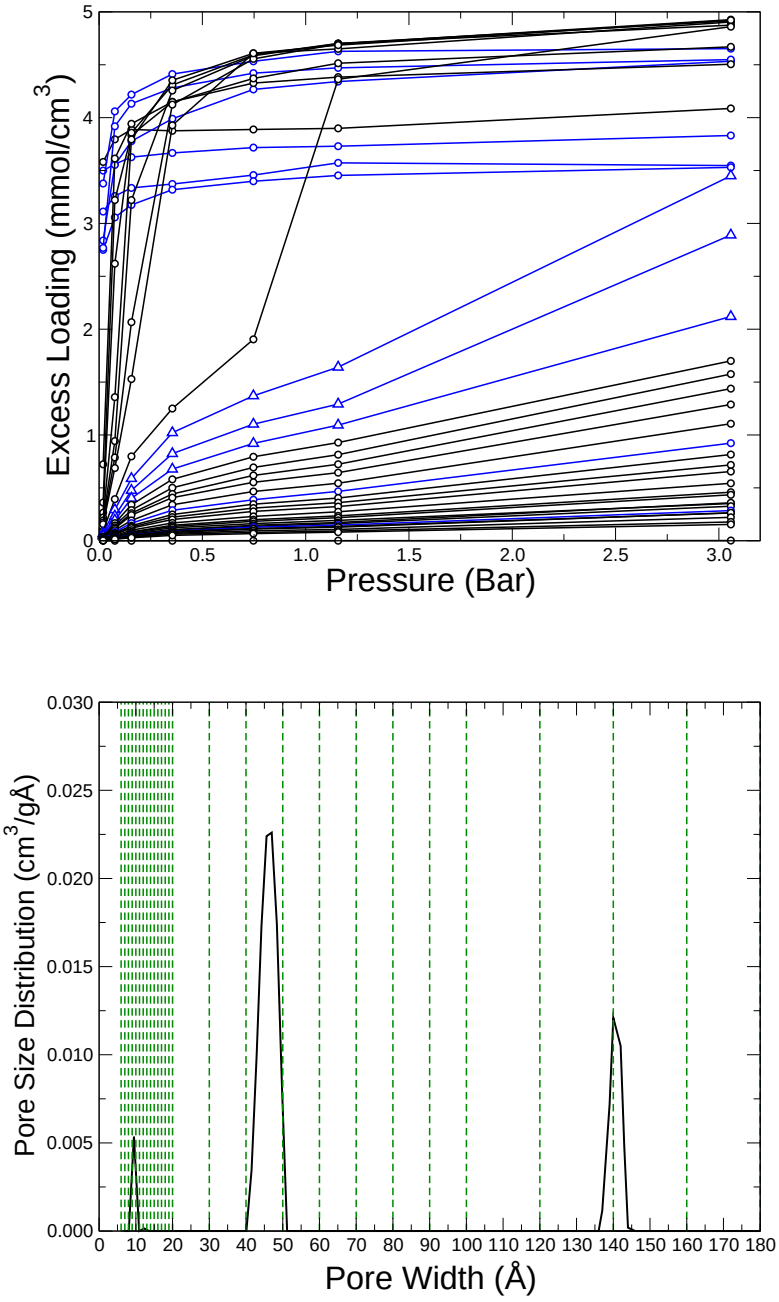

Figure 5.2: Top: Original set of simulated isotherms used for the prediction of n-heptane at 420 K, by Costa and co-workers.[39] Adsorption isotherms in slit pores of widths present in the PSD for CCD are shown in blue. Isotherms in black represent pores not present in the CCD PSD. Isotherms shown as blue lines with open blue triangles represent, from higher loading to lowest, adsorption in pores of 40, 50 and 60 Å respectively. Bottom: Original PSD (black line) for CCD structure. Pores present in the set of simulated n-heptane isotherms are shown in green dashed lines.

5.3 Second Generation of Pore Size Distributions

Below we present the parameters and details of the protocol to generate adsorption isotherms and kernels adopted in this work. They are different from those used by Costa and co-workers and obviously one might expect it should lead to PSDs different from those obtained in the original studies. At this stage we do not know how significant these differences are and whether they have a profound effect on the predicted adsorption behaviour. As we present a number of results, it is useful to introduce a terminology to delineate the results of this work and of previous studies. In this work we consider two types of engine deposit, CCD and IVD. The original PSDs developed by Costa and co-workers will be referred to as CCD-I and IVD-I, while the new PSDs (presented in this section) will be referred to as CCD-II and IVD-II, in order to indicate the first and second generation of models. To be clear, CCD-I and CCD-II refer to the same deposit sample, they are only characterised using different adsorption kernels (the same is true for the IVD sample).

In the next section we outline the parameters and technical procedure of the characterisation process, also revisiting the window of reliability concept. We present both the simulated sets of isotherms used for kernel construction, and the structures for CCD-II and IVD-II.

5.3.1 Parameters for Characterisation and Improved sets of Adsorption Isotherms

The experimental isotherms originally used by Costa and co-workers were also used to obtain CCD-II and IVD-II. Details on the experimental set-up can be found in the relevant previous publications,[39,40] while the experimental isotherms have been reproduced in Figures 3.4 and 3.6. Following the methods of Davies and Seaton,[41,42,71] the pore range of interest is discretised, the appropriate matrix is formed, and the AIE is inverted and solved to obtain the PSD. The pore range is discretised by first selecting values for the lower bound (w_{lower}), the upper bound (w_{upper}) and the maximum pore size (w_{max}).

The relationship between w_{upper} and w_{max} was introduced by Gusev and co-workers.[32] They suggested that there is a limiting threshold pore size (w_{upper}) above which the adsorption in a pore is essentially just the adsorption on two independent surfaces and pores above this value contain no additional information of adsorption

within pores.[32] When considering excess adsorption, isotherms for pores above w_{upper} are typically flat and the relationship between loading and pore size becomes linear.

The range of pores is split into N quadratures; a single quadrature spans from w_{upper} to w_{max} to account for the adsorption in all pores greater than w_{upper}, the remaining pore range (from w_{lower} to w_{upper}) is split into $N-1$ equally sized quadratures. In this work we used $N = 255$, $w_{lower} = 6\,\text{Å}$, $w_{upper} = 60\,\text{Å}$ and $w_{max} = 800\,\text{Å}$. Formally, including pores that do not contain additional information on the adsorption within the pores increases the condition number of the $\mathbf{N} = \mathbf{AWf}$ matrix, increasing the ill-conditioned nature of the problem. Gusev et al. noticed that this coincided with pores that have a linear shape, and so we adopt the simple approach of visual inspection to determine our upper bound of pore size, w_{upper}. A value of 60 Å was chosen as isotherms above this are found to be linear, as shown in Figure 5.3, and so it can be concluded that these pores add no additional information to the characterisation process, and can instead be linearly interpolated with confidence.

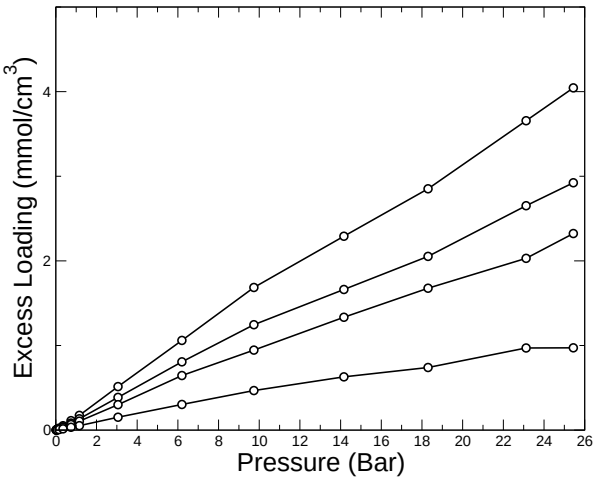

Figure 5.3: Simulated adsorption isotherms for ethane at 278 K in, from highest loading to lowest, 60, 80, 100 and 200 Å pores. The linear nature of pores above 60 Å is the justification for using it as the upper bound for the window or reliability.

This imposes a condition on the number of pressure points within each isotherm; therefore both experimental and simulation isotherms have been interpolated to feature 255 pressure points. Each quadrature requires an isotherm to represent the excess loading of pores within that range, and so the adsorption for the average

pore size of each range is interpolated from the new set of simulated isotherms, thus forming the adsorption kernel.

Figure 5.4 shows how the set of adsorption isotherms for ethane at 278 K were improved in the areas described in Section 5.2. The graph on the top shows again the original set used for the characterisation of both CCD-I and IVD-I. The blue highlighted isotherms are those within the range of 30 to 60 Å, a pore range known to contain a major peak in the PSD for both CCD-I and IVD-I. The graph on the bottom of Figure 5.4 shows the new set of isotherms, with those in blue again highlighting pores in the 30 to 60 Å range. It is important to note that changes were made to the majority of pores, not just those highlighted in blue. Differences between the two sets of isotherms include significantly more detail regarding the mesopore range through both a higher number of isotherms and a larger number of points, leading to smoother isotherms. In addition, the adsorption isotherms from 60 Å to 800 Å (i.e. the upper bound and the maximum pore size) have been removed, as they are no longer necessary for the interpolation process. Supplying these isotherms will, in theory, have no effect as this range is considered beyond the window of reliability, and adsorption loading is assumed to increase in a linear fashion. Within the characterisation model, adsorption within this range is accounted for in the kernel by a single isotherm in the centre of this range (420 Å) which can be interpolated from the 60 Å and 800 Å adsorption isotherms. Altogether, interpolation between the pressure values and between the whole isotherms is now based on much smaller interpolation intervals between the neighbouring values, which should increase robustness of the process.

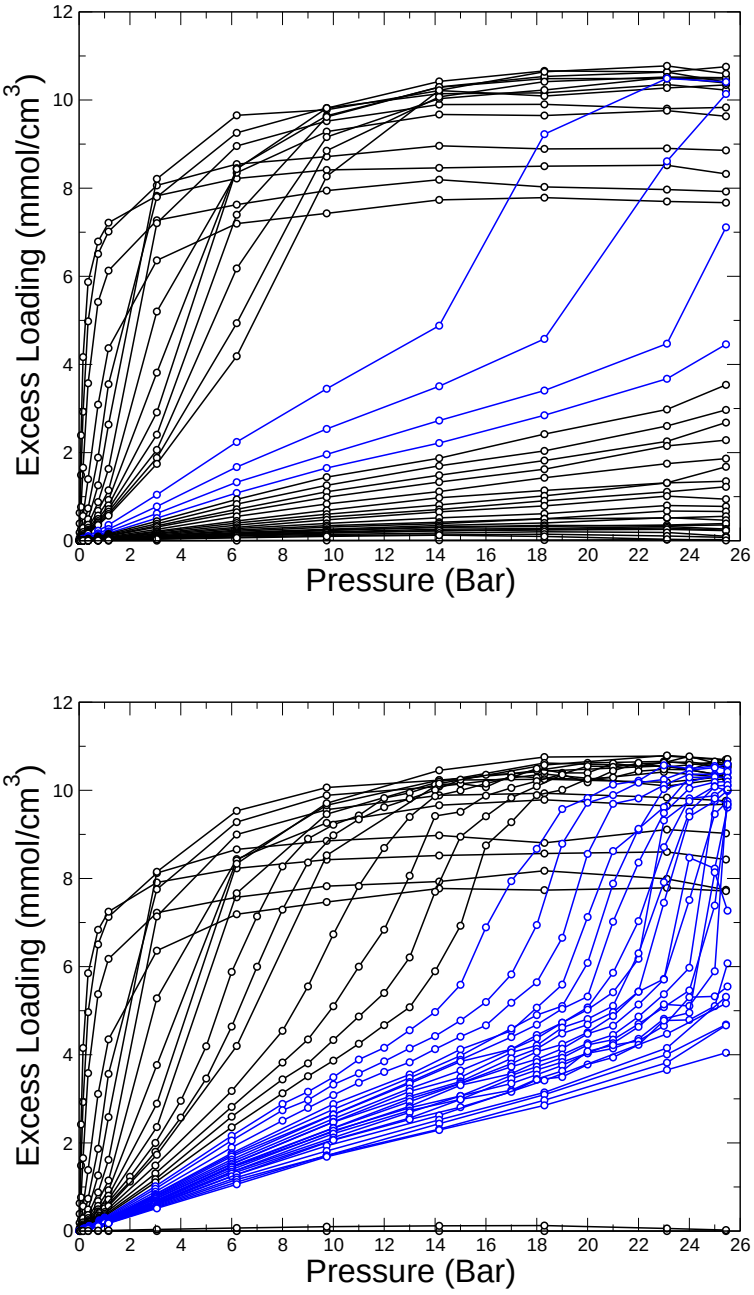

Figure 5.4: Sets of simulated adsorption isotherms for ethane at 278 K used for calculating the pore size distributions. The original set from the work of Costa and co-workers is shown in the upper graphic, the more detailed set, with the described improvements, is shown in the bottom graphic. Isotherms shown in blue correspond to pores in the range between 30 Å and 60 Å, a range of pores now known to be present on the PSDs. Pores between w_{upper} (60 Å) and w_{max} (800 Å) were removed as they lie beyond the window of reliability.

5.3.2 Combustion Chamber Deposit

Figure 5.5 shows the PSDs for both CCD-I and CCD-II. Note that the full pore range is not shown, and CCD-I contains additional peaks showing pores around the 140 Å and 430 Å range (see Figure 3.5). CCD-II contains no peaks above 60 Å, a consequence of implementing an upper window of reliability of 60 Å.

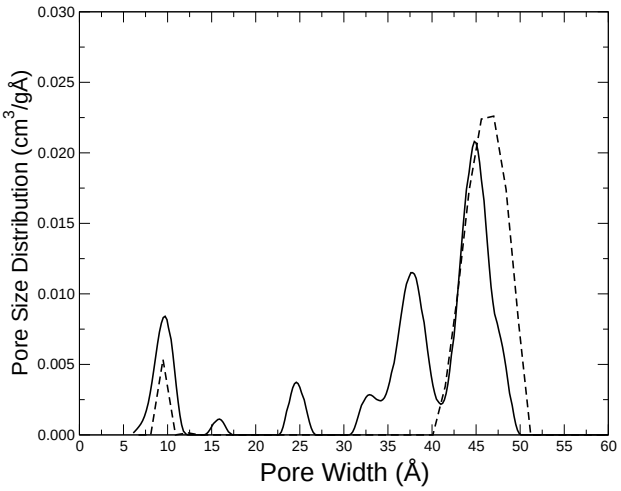

Figure 5.5: Pore size distributions for CCD-I (dashed line) and CCD-II (solid line).

From Figure 5.5 we can see that CCD-I showed a single, smooth peak in the lower mesoporous region, spanning from 40 - 52 Å. In general, this pore range has been broadened to include all pores between 30 and 50 Å, the main features of which include two peaks at 38 Å and 45 Å. Additional minor peaks have appeared at 16 and 25 Å and the peak around 10 Å in CCD-I has been enlarged to cover a wider range.

To explain this, we begin with a comparison between the experimental and simulated isotherms using the original data from Costa et al.[39] Figure 5.6 shows the experimental data (blue line with open blue diamonds) obtained for the adsorption of ethane on CCD at 273 K; this data was used to obtain the corresponding PSD. Overlayed onto this graph are original adsorption isotherms for selected pores from the simulated adsorption kernel. These include isotherms for 10 (closed circles), 20 (closed squares), 30 (closed triangles), 40 (open circles), 50 (open squares) and 60 Å (open triangles) pore widths. Note that for all isotherms, simulated and experi-

mental, the symbols represent actual data points and the lines are for eye guide only. Also note that the y-axis in this graph is showing loading in arbitrary units, as the quantitative values are not important in this example, it is only the shape of the isotherm that is required.

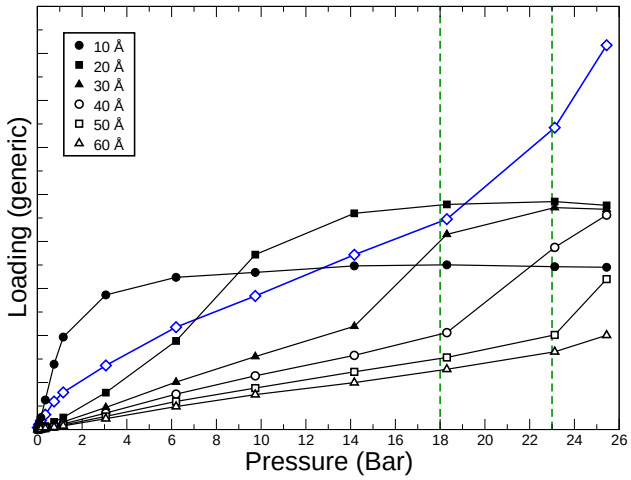

Figure 5.6: Experimental adsorption isotherm for ethane at 273 K on CCD by Costa and co-workers[39] shown by open blue diamonds and blue line. Adsorption isotherms of slit pores including 10, 20, 30, 40, 50 and 60 Å pores are shown as closed circles, closed squares, closed triangles, open circles, open squares and open triangles respectively. A pressure range of interest is highlighted by dashed green lines, details of which can be found in the text.

In a somewhat simplified way, we can relate the shape of the individual isotherms in slit pores and the extent to which they are present in the PSD to the resulting shape of the cumulative (experimental) isotherm. For example, the 30 Å pore shows a rise in loading between 14 and 18 bar. However the experimental isotherm shows no similar distinct increase in loading between these pressures. From this data, one can speculate that it is likely that pores of 30 Å are not present on the CCD structure. This is reflected by the absence of peaks around 30 Å in CCD-I (see Figure 5.5). On the other hand, the experimental isotherm shows that between 18 and ~23 bar (this range is shown in Figure 5.6 by green dashed lines) there is a distinct rise in loading. While all the isotherms (except the very narrow 10 and 20 Å pores, which reach plateau at these pressures) increase slightly, only the simulated isotherm in 40 Å pores shows a corresponding increase in the adsorption loading. As the 30 and 50 Å pores show a loading increase before and after this pressure range, the

rise in experimental loading must be due to the 40 Å pore *according to the limited information available in this isotherm set*. In reality, we can only exclude the 30 Å and 50 Å pores, all pores between these, from 31 Å to 49 Å, could feasibly contribute to this loading increase.

Compare the above analysis to a similar one for the new model, based on the more resolved adsorption kernel. Figure 5.7 shows a similar graph of the experimental data for ethane on CCD at 273 K, but the isotherms overlayed are now taken from the second generation of the adsorption kernel. The isotherms shown are for 30, 32, 34, 36, 38 and 40 Å pores. The figure includes a pressure range from 18 to 23 bar, bounded by dashed green lines. The two experimental points, at ~18 bar and 23 bar, show there is a distinct rise in the experimentally determined loading across this range.

At the start of the range, it can be seen that the capillary condensation effects in the 30 Å pore have only just occurred. As condensation occurs at lower pressures with increased confinement, all the pores slightly larger than 30 Å are going to have some contribution to the loading increase within the highlighted pressure range. In the first (generation I) set of isotherms, this loading increase was attributed solely to the 40 Å pore, it is clear to see that all pores from 32 Å to 40 Å have condensation to some degree between these pressures. In fact, the 40 Å pore is only just contained within this range, with the condensation occurring around 22 bar. The importance of the smaller pores in this loading increase is captured by a shift in the distribution to pores around 33 and 37 Å in the new PSD.

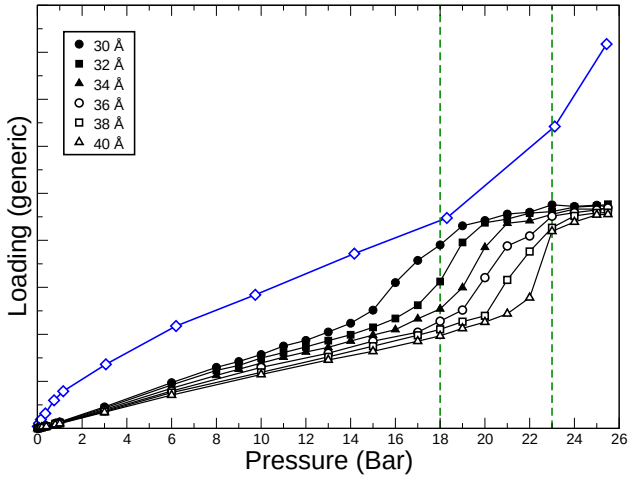

Figure 5.7: Experimental adsorption isotherm for ethane at 273 K on CCD by Costa and co-workers[39] shown by open blue diamonds and blue line. Adsorption isotherms of ethane in slit pores of widths 30, 32, 34, 36, 38 and 40 Å are shown as closed circles, closed squares, closed triangles, open circles, open squares and open triangles respectively. A pressure range of interest is highlighted by dashed green lines, details of which can be found in the text.

5.3.3 Intake Valve Deposit

Using the improved resolved adsorption kernel, a second generation of IVD pore size distribution was obtained, shown in Figure 5.8. Similar to the CCD-II structure, the single peak spanning the 35 to 50 Å range has been broadened to encompass a wider range of pores, with two distinct peaks at 37 and 40 Å. The microporous peak around 10 Å is essentially unchanged between IVD-I and IVD-II. The explanation for the shift in mesopores in the CCD sample also applies to the IVD. Better resolution of the kernel in the 30 - 50 Å range allows the identification of pores present in this region.

The developed pore size distributions show possible structures for different engine deposits. While there is some discrepancy over the exact details in the structure, there is a clear common trend. Both CCD and IVD materials feature micropores around 10 Å and mesopores, broadly between 30 Å and 55 Å. Using simulation techniques the adsorption of more complex species and mixtures onto these deposits can now be investigated.

Due to the complexity of factors that affect deposit formation, differences in

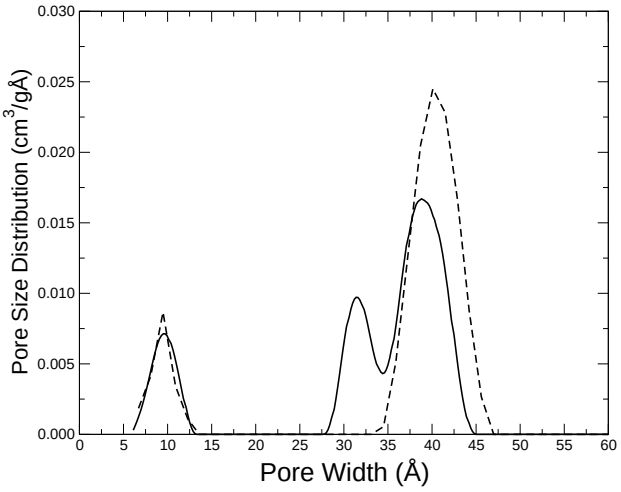

Figure 5.8: Pore size distributions for IVD-I (dashed line) and IVD-II (solid line).

deposit structure between different types of deposits and from different engines is expected. The extent of these differences is still unclear. For example, here we found that the IVD and CCD samples are similar in structure. However the CCD sample examined by Zerda and co-workers (see chapter 1) was reported to be exclusively comprised of mesopores.[2] With the large variation in reported structures, it is unlikely the any two samples of engine deposit will be identical. As such, the research in this thesis also includes a detailed analysis of adsorption behaviour in pores of different sizes. By investigating how changes in the PSDs influence predicted adsorption isotherms, valuable insights can be made into how other deposit structures interact with fuel components and also on the robustness of the whole approach. Some preliminary investigations of this issue are provided in the next section.

5.4 Impact of Model Modifications on the Predicted Adsorption Behaviour

In this section we discuss the general effects that the improved adsorption kernels have on predicted isotherms, as well as exploring the specific impact of such changes by revisiting the systems considered in Chapter 3. To reiterate, within the overall AIE process there are two areas where the kernels are used: characterisation of the

porous material to obtain a PSD, and for the prediction of adsorption in a new system, in terms of either the conditions or adsorbing species (or both) using this PSD. The new generation adsorption kernels and PSDs presents us with several possible scenarios for analysis. The first obvious choice is to compare the original results from Costa and co-workers to the new results obtained with the new kernels and PSDs (new simulations on new PSD). However, we can also investigate the effect of the higher kernel resolution alone by comparing adsorption isotherms obtained from the new kernel integrated over the original PSDs (new kernel on the old PSD) to those obtained by integrating over new PSDs (new kernel on the new PSD). The remainder of this section will explore both of these angles, beginning with an overall look at how kernel improvements changed the adsorption prediction.

5.4.1 General Impact

In order to show the general changes, we use adsorption of n-heptane on CCD-II at 420 K as a case-study. Figure 5.9 shows the updated version of the isotherm set used for this prediction (shown on the left), this can be compared to the original set shown in Figure 5.2. The same improvements were made as outlined at the start of the chapter: the number of isotherms was increased and the detail of each isotherm was fine-tuned to capture the capillary condensation process. The upper bound and maximum pore range was also set at 60 and 800 Å respectively, and isotherms between these are removed. These improvements allow a more resolved kernel to be constructed. The right-hand side of Figure 5.9 shows predicted isotherms for both the original results (old kernel integrated over CCD-I, dashed line) and the new results (new kernel integrated over CCD-II, solid line).

The original predictions over CCD-I tend to consist of sections of linear increases in loading, an artefact of the interpolation over limited number of points on the isotherms. In contrast, predictions of the new kernel over CCD-II show a much more varied isotherm. The most notable change is the presence of steps in the isotherm, characterised by a sudden increase in adsorbed density. These steps are a result of the capillary condensation of n-heptane within individual pores of a given size. The height, or size, of the step-increase is proportional to the frequency at which the pore is found in the structure. These isotherm steps can be linked to the adsorption behaviour in individual pores, identifying which pores the condensation is occurring in. Figure 5.10 shows the prediction of n-heptane on CCD-II at 420 K overlayed with

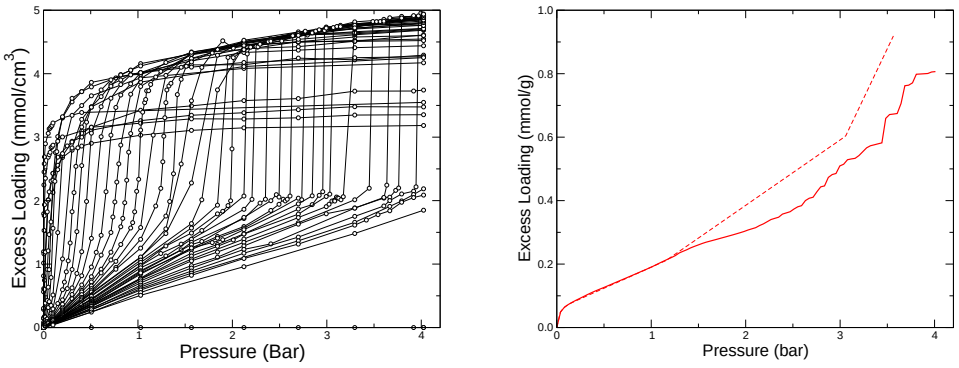

Figure 5.9: Panel on the left shows the improved adsorption kernel for n-heptane at 420 K. Panel on the right shows predictions of n-heptane adsorption on CCD. The dashed line shows original results from Costa and co-workers (original kernel integrated over CCD-I), and the solid line shows new results (new kernel integrated over CCD-II).

the adsorption isotherm for n-heptane in both 44 and 46 Å pores. By plotting the prediction and pore-specific isotherms on the same pressure-range, it is interesting to see that the condensation in both pores causes a step increase in the prediction isotherm. This feature is due to the higher resolution of the isotherms allowing the individual effects of each pore size to be seen.

The new kernel, however, is not perfect. From examination of Figure 5.5, it can be seen that the CCD-II PSD contains a significant peak at 45 Å pores. We might expect, from the previous explanation, a corresponding increase in the n-heptane prediction between those accounted for by the 44 and 46 Å pores. However, examination of Figure 5.10 reveals that this is not the case. This arises from the lack of simulated isotherm at 45 Å in the set used for kernel construction. The required data for this pore size is obtained via linear interpolation between the the isotherms for 44 and 46 Å pores. Consider, for example, a pressure of 3.5 bar. At this pressure, the 44 Å pore has already gone through capillary condensation (loading slightly below $5\,{}^{\mathrm{mmol}}/_{\mathrm{cm}^3}$) while the 46 Å pore has not (loading around $2\,{}^{\mathrm{mmol}}/_{\mathrm{cm}^3}$) with the density for the 45 Å pore linearly interpolated between these two densities. Thus the plateau between two steps is an artefact and serves as an example of how the adsorption kernel and the protocol can still be improved. Indeed, with no restriction on computer processing a perfect kernel could be constructed by simulating all of the required

quadrature widths, eliminating the need for interpolation entirely. Alternatively, a different interpolation protocol which would correctly predict the location of the capillary condensation step from two neighbouring isotherms should be devised.

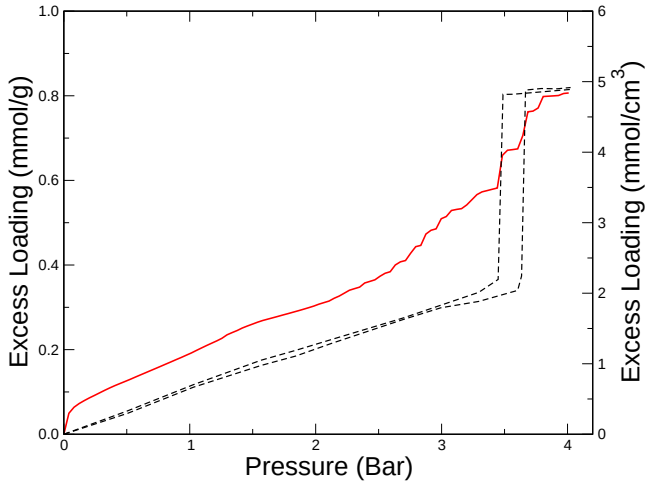

Figure 5.10: Prediction of n-heptane adsorption at 420 K on CCD-II, overlayed with isotherms for slit-pore adsorption in 44 and 46 Å pores (left and right black dashed lines, respectively). Steps in excess loading can be accounted for by condensation in the associated pore.

As a final look at the types of effects the new generation of PSDs have, Figure 5.11 shows isotherms for the prediction of n-heptane adsorption on both CCD-I (dashed line), and CCD-II (solid line) at 420 K, using new, more resolved kernels in both cases. Both isotherms feature step changes in density. This implies that the steps in the adsorption isotherm seen in Figure 5.9 are not due to the change in the PSD, but are a result of the increase in resolution in the adsorption kernel used for this particular prediction. The prediction over CCD-II shows a gradual increase in adsorption loading, spread over a much larger pressure range beginning at around 2 bar. This is because the pores found on the structure are distributed over a wider spread of pore sizes. In contrast, the prediction over CCD-I sees little increase in loading until around 3 bar as the pores in this structure are distributed over a smaller range of wider pores. Condensation in these wider pores occurs at higher pressures, so the loading increase occurs at higher pressures.

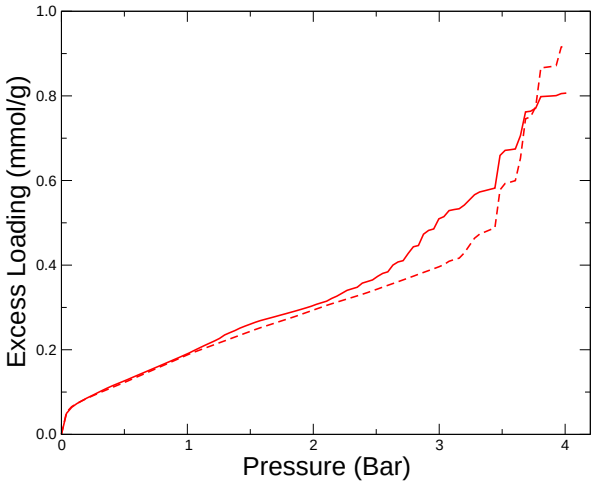

Figure 5.11: Predictions of n-heptane adsorption at 420 K on CCD-I (dashed line) and CCD-II (solid line). All predictions were made using the updated adsorption kernel for n-heptane.

5.4.2 Comparison to Original Simulation and Experimental Results

In order to investigate the accuracy of the new model, we revisit the validation steps of the original work by Costa and co-workers (see Chapter 3) by comparing experimental isotherms to new predictions over the second generation of PSDs. Figure 5.12 shows experimental results for the adsorption of ethane on CCD at both 278 K (left) and 298 K (right) along with simulated isotherms for both CCD-I (dashed line) and CCD-II (solid line). Figure 5.13 shows the same set-up for IVD at 278 K (left) and 293 K (right). In all cases the similarities between the simulated isotherms makes it difficult to differentiate between the predictions, which indicates in these situations the improved kernel and changes in the PSDs have a minimal effect.

For the final comparison to experimental data, Figure 5.14 shows a comparison of experimental to simulated isotherms for the adsorption of n-butane on CCD at 293 K. The dashed line shows the original results of Costa and co-workers[40] (original kernel integrated over CCD-I) and the solid line shows the improved kernel integrated over CCD-II. From this figure we can see the presence of previously described steps in the adsorption loading, associated with capillary condensation in specific pores. Aside from these small differences, the overall shape of the prediction is unchanged,

and the two predictions are very similar.

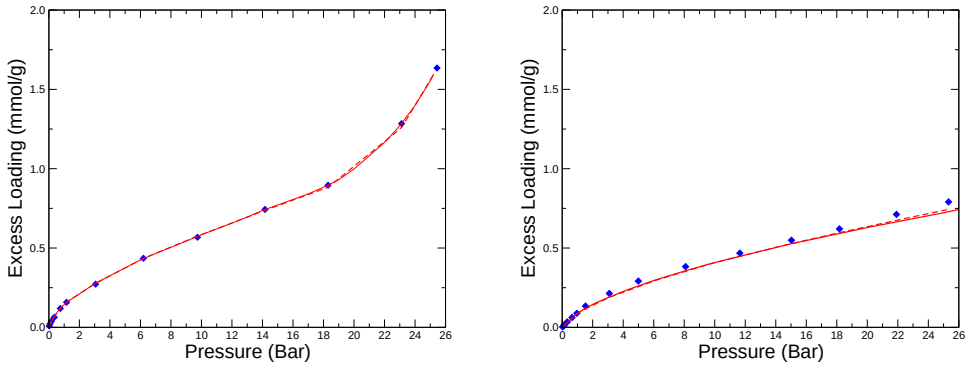

Figure 5.12: Comparison of simulated adsorption isotherms for different PSD generations versus experimental isotherms for ethane on CCD. Dashed red line shows the original kernel integrated over CCD-I, solid line shows the improved kernel integrated over CCD-II. Blue diamonds show experimental measurements. Left graph shows results at 278 K, right graph shows results at 298 K.

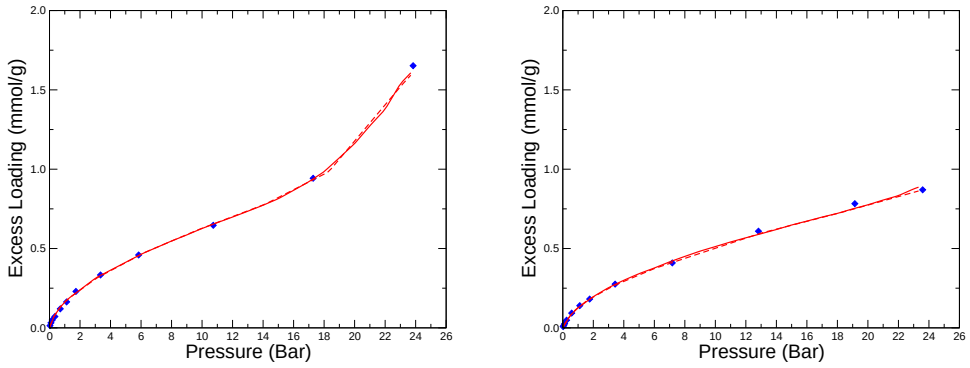

Figure 5.13: Comparison of simulated adsorption isotherms for different PSD generations versus experimental isotherms for ethane on IVD. Dashed red line shows the original kernel integrated over IVD-I, solid line shows the improved kernel integrated over IVD-II. Blue diamonds show experimental measurements. Left graph shows results at 278 K, right graph shows results at 293 K.

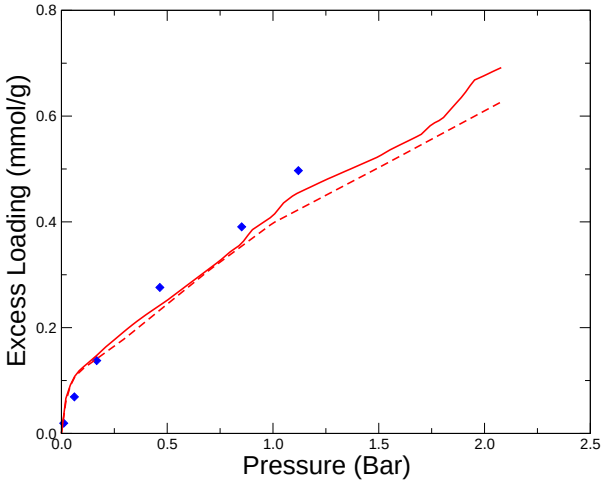

Figure 5.14: Comparison of simulated adsorption predictions for different PSD generations versus experimental data for n-butane on CCD at 293 K. Dashed red line shows the original kernel integrated over CCD-I, solid line shows the improved kernel integrated over CCD-II. Blue diamonds show experimental measurements.

5.4.3 Adsorption of Fuel Components

Finally we explore how the modifications to the adsorption model affect predictions of fuel components by comparing the original and new results for the adsorption of n-heptane and i-octane onto both CCD and IVD. Figure 5.15 shows comparisons of predicted isotherms for the adsorption of n-heptane (left) and i-octane (right) on CCD-I (dashed lines) and CCD-II (solid lines) at 420 K. Figure 5.16 shows similar predictions for IVD-I (left) and IVD-II (right).

Overall, the adsorption trends between the generations of PSD do not change significantly. The new isotherms now display the step-increases in loading associated with capillary condensation in individual pores. As explained, this is a consequence of the adsorption kernel holding more detailed information on the adsorption in individual pores. In each case, both isotherms contain the initial sharp loading "knee" at very low pressures, as well as the more substantial increase in loading at higher pressures as mesopores begin to condense.

In the case of IVD, the similarity of the predictions between generations is not very surprising given the similarities between the IVD-I and IVD-II PSDs. In the case of CCD, however, the two generations were more significantly different. This is not particularly reflected in Figures 5.15 and 5.16, indicating that although increasing the resolution of the kernel leads to different PSDs, the overall predictions are somewhat insensitive to these changes. Adsorption trends are instead more dependent on what range of pores are found in the structure; the presence of micropores causes the initial "knee" in the isotherms, seen at very low pressures; while the mesopore range is responsible for the loading increase seen at higher pressures (for example, the increase beginning around 2.5 and 2.0 bar for n-heptane and i-octane on CCD-II, respectively).

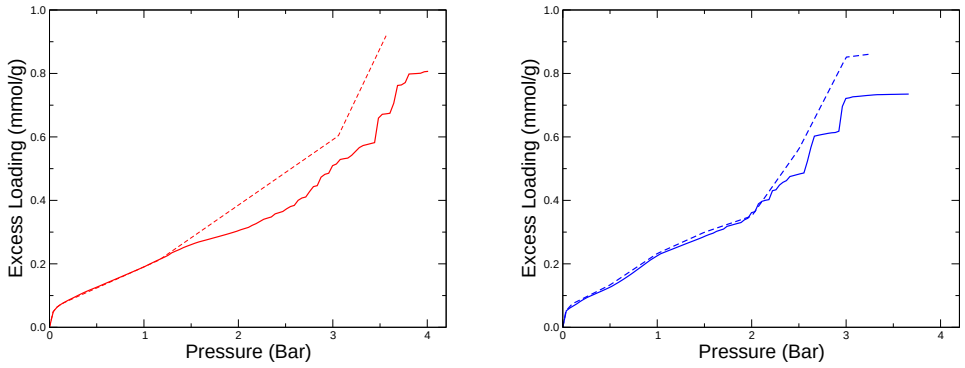

Figure 5.15: Comparison of simulated adsorption isotherms for different PSD generations for n-heptane (left graph, red lines) and i-octane (right graph, blue lines) on CCD at 420 K. Dashed lines show the original kernel integrated over CCD-I, solid lines shows the improved kernel integrated over CCD-II.

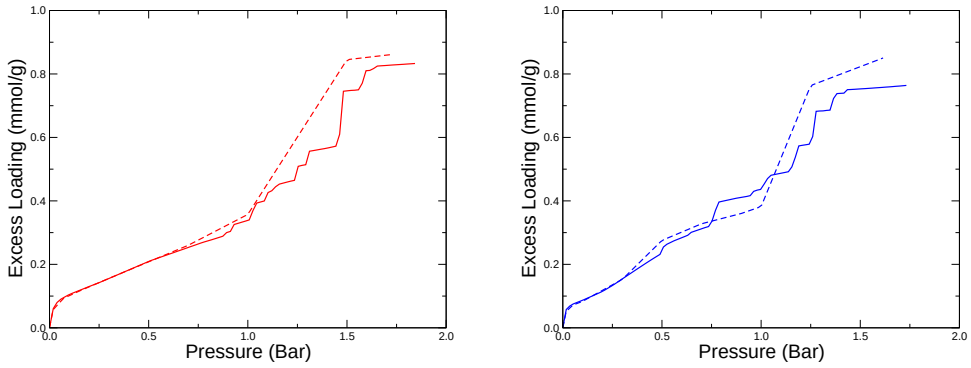

Figure 5.16: Comparison of simulated adsorption isotherms for different PSD generations for n-heptane (left graph, red lines) and i-octane (right graph, blue lines) on IVD at 390 K. Dashed lines show the original kernel integrated over IVD-I, solid lines shows the improved kernel integrated over IVD-II.

5.5 Conclusions

The resolution of the adsorption kernels was improved by creating more detailed simulated isotherm sets, from which the kernels are constructed. The isotherm sets were improved in two areas: the number of isotherms per set was increased to include significantly more pore widths, and the number of pressure points of each isotherm was increased to obtain more accurate information on the adsorption characteristics of each pore size. Applying these improved kernels to the characterisation process generated new PSD structures, with some differences from the previous results. Exact details on the differences varied with deposit type, but in general PSD peaks in the mesopore range were resolved over a broader range, revealing a more complex (compared to the previous studies) PSD in the mesoporous range for both types of deposits.

The improvements to the adsorption kernel had a minor impact on the predicted isotherms. A more accurate view of adsorption behaviour in slit pores manifests itself in prediction of small steps in the adsorption loading, associated with the capillary condensation phenomena in individual pores. These steps are found in predictions based on both the original and new PSDs, and is shown to be an effect of the increased resolution of adsorption isotherms in the capillary condensation region of pressure values for individual pore sizes.

New generations of PSDs were obtained for both CCD and IVD, giving a second generation of possible models for deposit structures. By revisiting the adsorption of fuel components in IVD and CCD, it was shown that the original conclusions of Costa and co-workers (outlined in Chapter 3) remain unchanged, and adsorption of both n-heptane and i-octane is significant. The characterisation procedure for the new generation of PSDs has been shown to be more accurate. Due to the intrinsic link between the characterised solid and adsorption predictions it can be argued that the predictions using these new PSDs are also improved, even if overall adsorption trends appear to be unchanged.

Chapter 6

Predictive Studies of Adsorption of Gasoline Components and their Binary and Ternary Mixtures in Engine Deposits

In this chapter we address the main research objective of the thesis, associated with adsorption of mixtures of fuel components in engine deposits. Previous work, outlined in Chapter 3, focused on the characterisation of engine deposit structures and the adsorption of single component systems of i-octane and n-heptane. The key advantage of molecular simulations over experimental techniques is that the adsorption of multi-component mixtures can be considered almost as easily as single component systems. In addition, one family of components that has not been considered in previous predictive studies is aromatic hydrocarbons, and yet they are typically present in fuels in volumes above 30 %[73] as a high octane component of the gasoline.

We extend the current picture of engine deposit adsorption in several important aspects. First, we revisit the original adsorption studies using a more refined PSD model, as well as a greater resolution of the kernel isotherms. In addition to iso-octane and normal heptane, considered previously as components of the fuel with extreme values of octane number, we also consider adsorption of toluene as a representative of aromatic species. We investigate, for the first time, the adsorption of the binary and ternary mixtures of these species, and explore any selectivity effects

that arise.

The structure for the chapter is as follows. We present single-component adsorption isotherms for i-octane, n-heptane and toluene on both CCD and IVD, and comment on the Henry's constants of adsorption of these species on both CCD and IVD. We expand the studies by investigating adsorption isotherms for the binary mixtures of the three species in pairwise combinations, and complement these with an in-depth selectivity analysis. Due to similarities in behaviour of the CCD and IVD systems, this selectivity analysis is limited to CCD alone, however isotherms and selectivities for IVD are also shown. Due to the similarities in the adsorption behaviour, the selectivity analysis of CCD can also be applied to IVD. We present adsorption isotherms for the ternary mixture of i-octane, n-heptane and toluene on both CCD and IVD. We also speculate on possible selectivity effects by combining i-octane and toluene together to form a single "high-octane" group, and look at selectivity of this group over n-heptane. Finally, we perform some uptake studies to assess the extent to which engine deposits could adsorb fuel components under typical conditions found within the engine. These calculations, while subject to several assumptions, provide a coarse guide to the levels of adsorption we might expect.

6.1 Single Component Systems

We begin with the single component results. Figure 6.1 (left panel) shows predicted adsorption isotherms for i-octane, n-heptane and toluene in IVD at 390 K, while the right panel of this figure shows these isotherms in CCD at 420 K. We note that all three species exhibit similar trends and adsorb in comparable amounts, regardless of structure. At higher pressures the isotherms also feature steps in adsorbed densities, which are particularly pronounced for i-octane and n-heptane isotherms on both samples. These steps are associated with capillary condensation of adsorbing species in pores of particular width. As we have already discussed in Chapter 5, the particular roughness of the isotherms is partially due to the way how the isotherms exhibiting a capillary condensation are interpolated between the two pore widths and therefore we may want to downplay the importance of the location of the specific steps: in principle, under a different interpolation method the isotherms integrated over the new PSDs shown in Chapter 5 should be reasonably smooth. In fact, as we will show below for the analysis of the loading in engine deposits, we need only

low pressure data and the pressure range where these steps take place is not directly relevant for the objectives of this chapter, however we consider the full range (up to the bulk saturation pressure for the system) for completeness.

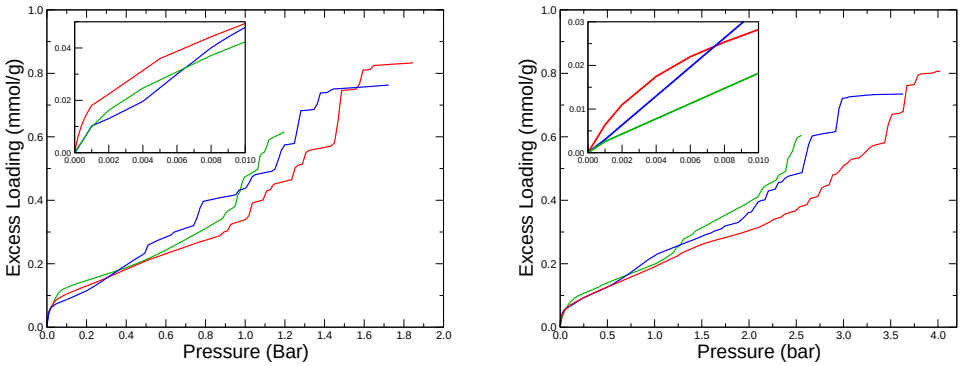

Figure 6.1: Predictions of single-component adsorption on IVD at 390 K (left) and CCD at 420 K (right). Predictions are shown for i-octane (blue), n-heptane (red) and toluene (green) adsorption. Insets are zoomed in on the low pressure region where initial adsorption takes place.

Leaving the low-pressure insets for now, an interesting feature of these isotherms is the higher loading of toluene at lower pressures. This is more pronounced in the case of IVD, and occurs from around 0.05 to 0.35 bar. For CCD, toluene shows higher loading between 0.1 and 0.7 bar. In addition, IVD shows that n-heptane also shows higher loading than i-octane for a similar pressure range. This is a result of a molecular sieving effect, where narrow 7 and 8 Å pores are accessible to the toluene and n-heptane, but not the i-octane molecules. From the PSDs (see Figures 5.8 and 5.11 in Chapter 5) we see that the micropore peak for IVD is wider than that of CCD, meaning the proportion of narrow (7 and 8 Å) pores is slightly higher in IVD, explaining the larger difference in loadings between the two samples. Toluene is able to adsorb more than n-heptane in these pores due to superior packing effects. Note that, even at these low pressures, pores of this size are already completely filled with molecules and so no longer in the "low loading" regime.

From the low-pressure insets in Figure 6.1, we are able to obtain estimations of the Henry's Constants of adsorption for each species in both CCD and IVD, which are shown in Figure 6.2. We see that, in both CCD and IVD, the Henry's constants for n-heptane exceed both toluene and i-octane and that values for the IVD sample are

lower than those of CCD. This last effect is a consequence of the lower temperature of the IVD system (390 K in IVD compared to 420 K for the CCD). It is also interesting to compare the Henry's constants of adsorption for the different species. Here, the molecular sieving discussed above causes the Henry's constants for both n-heptane and toluene to be higher than expected, when compared to i-octane. This effect is reduced in the CCD sample, again because the PSD contains fewer 7 and 8 Å pores, where i-octane cannot fit.

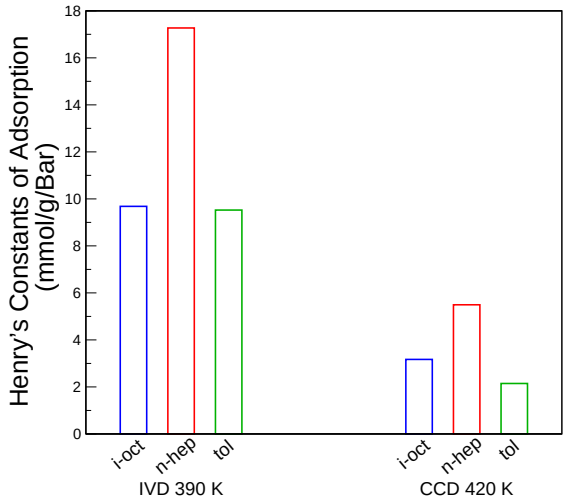

Figure 6.2: Henry's constants of adsorption for integrated isotherms on IVD at 390 K (left) and CCD at 420 K (right).

6.2 Binary Systems

Next we consider results for binary mixtures. In this section we first present adsorption isotherms for each binary system on both CCD and IVD. The CCD systems are used as case studies to provide an in-depth analysis of selectivity behaviour. Because of the similarities in adsorption behaviour between CCD and IVD, selectivity analysis is limited to CCD alone, however selectivity isotherms for IVD are provided at the end of the section. Binary systems in this study correspond to volume ratios between linear, branched and aromatic compounds that were calculated from a fuel specification, provided by Shell Global Solutions.[73] While the total content of each alkane type is not limited to only one species, we use n-heptane, i-octane and toluene as representative species of the three hydrocarbon groups. Mixtures of i-octane : n-

heptane and toluene : n-heptane use a 75 : 25 ratio, on a liquid volumetric basis. In the case of i-octane : toluene, the ratio is 50 : 50.

6.2.1 Adsorption Isotherms

We begin examination of the binary systems with the adsorption isotherms on CCD and IVD, shown in Figure 6.3. The three systems shown are mixtures of i-octane : n-heptane (top panels), i-octane : toluene (middle panels) and toluene : n-heptane (bottom panels). For ease of reference, adsorption isotherms for components follow a consistent colour scheme: i-octane is indicated in blue, n-heptane in red and toluene in green. This scheme, unless otherwise stated, will be used throughout this chapter. The adsorption isotherms for the individual components (within the binary systems) resemble, in both shape and general trends, single component isotherms presented in Figure 6.1. The isotherms also feature steps in the adsorbed density associated with the condensation of the mixture in pores of a particular size. These steps occur at the same values of pressure for both components, the physical reason for this has been discussed in Chapter 4.

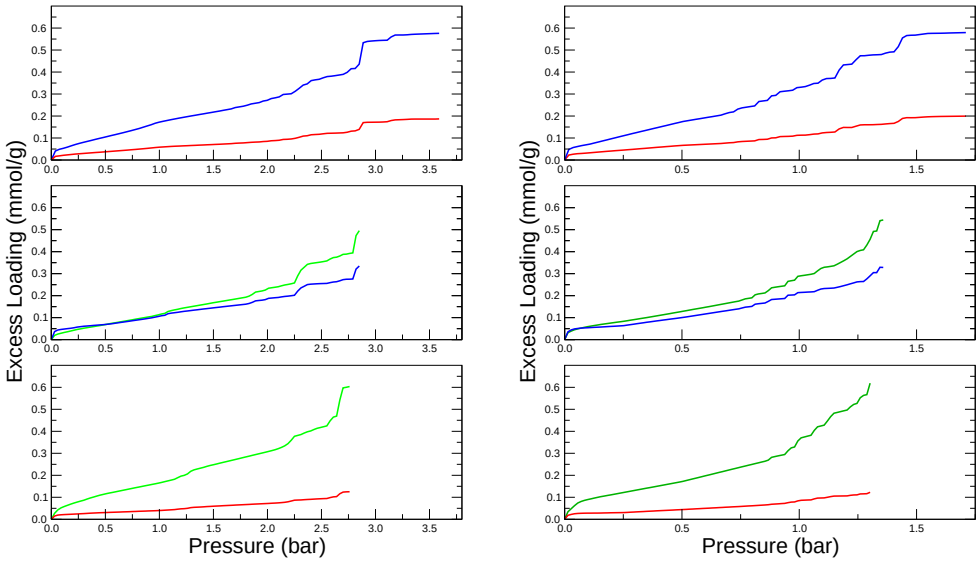

Figure 6.3: Predicted adsorption isotherms for binary mixtures on CCD at 420 K (left) and IVD at 390 K (right). From top to bottom binary mixtures are: i-octane(75 %) / n-heptane (25 %); i-octane(50 %) / toluene(50 %); and n-heptane (25 %) / toluene(75%); i-octane is shown in blue, n-heptane in red and toluene in green, respectively.

6.2.2 Selectivity in Binary Systems on CCD

From Figure 6.3 we can see the amount of i-octane and toluene adsorbed substantially exceeds the amount of n-heptane adsorbed. This is of course largely because of the dominant presence of these components in the binary mixtures with n-heptane. What is important to understand is whether the composition of the adsorbed mixture is different from the composition of the bulk phase. This would signify selective adsorption of one of the components in the mixture and this may have some important consequences for the operation of the engine. Here we use the selectivity, defined by Equation 4.2 in Chapter 4, to explore and quantify this effect.

In Chapter 4 we explored a number of properties of alkanes and their mixtures adsorbed in slit pores, as a function of pore width. As we have seen, selectivity even in a single pore can be quite a complex phenomenon, where enthalpic, entropic and packing effects are all important and strongly coupled with each other. The philosophy of this chapter is to look at the amalgamated behaviour of slit pores, through the prism of a PSD. Indeed, in Figure 6.4 we revisit the graphs for the

Henry's constants of adsorption and the isosteric heat of adsorption at zero loading, but now with the PSD for CCD superimposed on the graphs. As can be seen from this figure, the most important differences in the behaviour emerge in small pores (below 15 Å); and this is also where the CCD PSD features a strongly pronounced peak. We can anticipate that the behaviour of the material as a whole, including selectivity, will be governed by this range of pores. However, we shall see that although the graphs shown in Figure 6.4 generally help to explain selectivity phenomena, they are not sufficient to make predictions, and other factors associated with particular behaviour of mixtures must be considered.

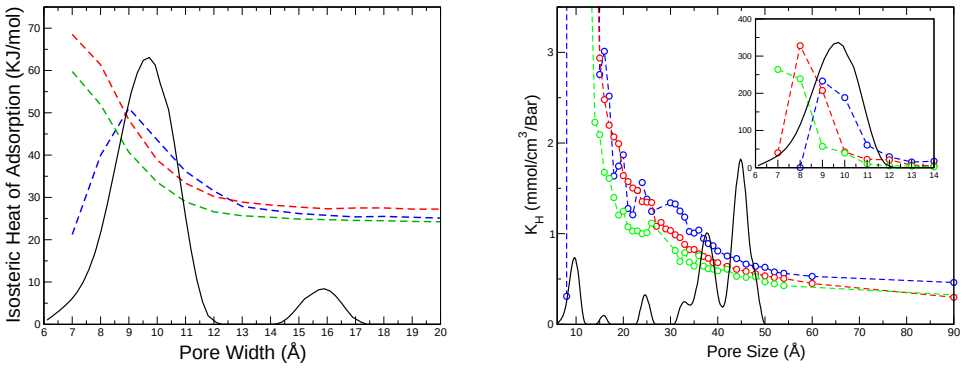

Figure 6.4: On the left: Isosteric heat of adsorption of a single molecule of adsorbing species with slit pore as a function of pore width at 420 K. Iso-octane is shown as a blue dashed line, n-heptane as a red dashed line and toluene as a green dashed line respectively. The CCD PSD is shown by a black line, in arbitrary units. On the right: Henry's constants of adsorption as a function of pore width for i-octane (blue dashed line, open blue circles), n-heptane (red dashed line, open red circles) and toluene (green dashed line, open green circles) at 420 K. CCD PSD is shown by a black line, in arbitrary units. The inset shows the full range of K_H for the narrow pore range from 6 - 14 Å, while the main graph shows the K_H range of interest for the larger mesopores.

In the next section we use the example systems of CCD to investigate selectivity effects of the binary systems. We present each section by starting with the adsorption and selectivity isotherms for the system and comment on particular trends. In order to understand these trends, in each case we look at selectivity effects as a function of pore width. Behaviour in individual isotherms is discussed and related back to the original behaviour of the system by comparing behaviour in individual pores to the PSD of the sample.

6.2.2.1 Binary System I: i-Octane and n-Heptane

The graph on the left in Figure 6.5 shows adsorption isotherms for the 75 : 25 binary mixture of i-octane : n-heptane on CCD at 420 K. The graph on the right in this figure shows the selectivity of i-octane over n-heptane. IVD shows a very similar behaviour both in terms of the adsorption isotherms and selectivity. From this figure it can be seen that at low pressure there is a very slight selectivity towards n-heptane, but as pressure is increased there is a slight, but definite, selectivity towards i-octane. It is interesting to consider what factors cause these selectivity trends and their dependence on pressure, and these are explored below.

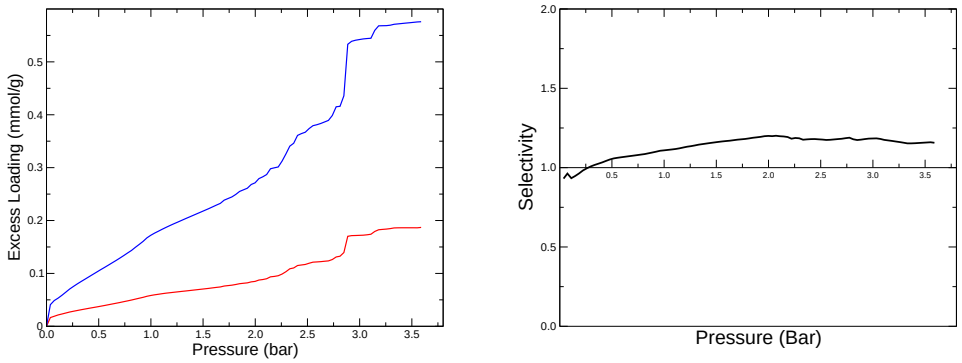

Figure 6.5: On the left: Predicted adsorption isotherms for binary i-octane (75 %, blue line) and n-heptane (25 %, red line) mixture in CCD at 420 K. On the right: selectivity of i-octane over n-heptane in the binary system as a function of pressure for CCD at 420 K.

The CCD sample in this model is considered to be built up of slit pores of varying widths, the frequency of which is governed by the PSD. While selectivity trends between i-octane and n-heptane were explored in Chapter 4, we revisit the selectivity as a function of pore-width in Figure 6.6 with an overlay of the PSD for CCD. This allows us to assess how slit-pore behaviour impacts the overall adsorption of the material. Towards this goal, we briefly summarise the trends mentioned in Chapter 4, but also include an interpretation on how these trends interact with the PSD to provide the selectivity seen in Figure 6.5.

Figure 6.6 can be summarised by four main trends for the different regions of interest. First, in the most narrow pores of the spectrum (less than 8.5 Å) selectivity towards i-octane is zero because in these pores it is geometrically difficult for i-octane

to fit. Presence of these very narrow pores is the reason behind the overall i-octane selectivity slightly below one at very low pressures. Second, a band of pores in the range 9 - 12 Å exhibit sharply peaked selectivity towards i-octane at both high and low pressures. As there is also a well pronounced PSD peak covering the same range, the overall selectivity of the material shifts towards i-octane (at 0.25 bar and above). The third region is a narrow band of pores between 13 and 14 Å, where selectivity is found to be in favour of n-heptane. This was shown to be associated with packing effects, with n-heptane able to form two layers within the pore, while i-octane is still confined to just one. From the PSD shown above, this band does not influence the overall behaviour of the sample.

The fourth and final region is that for the mesoporous range (less than 20 Å). While in Chapter 4 we were unable to explore these trends in sufficient depth, we revisit them now with a greater understanding of trends in the interaction strength for each species, allowing a more detailed analysis. From Figure 6.6 we see that at low pressure there is no definite selectivity towards either species, which is somewhat surprising given the higher Henry's constants for i-octane in these pores (see Figure 6.4). Given the amount of scattering and very low loadings, it may simply be due to poor statistics that no specific trend is revealed. As pressure increases, the selectivity shifts slightly in favour of i-octane in larger pores. This is again surprising: we might expect that at higher pressures, adsorption selectivity favours molecules that can pack more efficiently in a limited space. In this system, we might speculate that the linear n-heptane would be preferred over the branched i-octane, however this is not the case. It seems that the packing of molecules in dense binary mixtures may involve some additional effects not expected from single component scenarios, and the only conclusion remaining is that the selectivity process becomes dependent on the composition of the mixture. Exploration of this is, unfortunately, beyond the scope of this thesis and left for future investigation. From the PSD we see that mesopores are quite prevalent in the CCD structure, and so we would expect that as pressure increases, the selectivity behaviour tends towards a slight preference for i-octane: this trend is exactly what is seen in Figure 6.5.

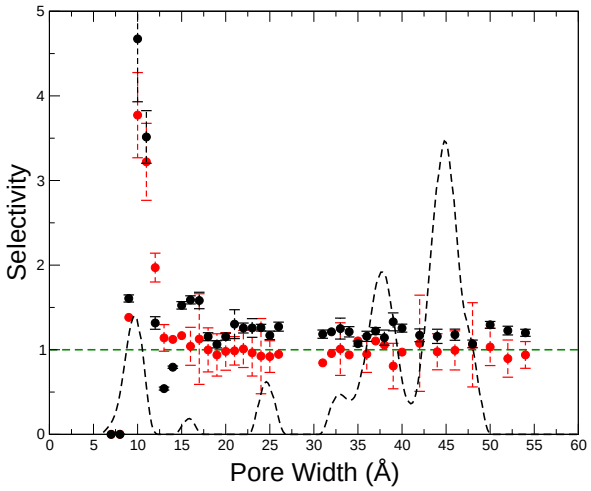

Figure 6.6: Selectivity of i-octane over n-heptane in a 75 : 25 mixture at 420 K as a function of pore width for high (3.6 bar, black circles) and low pressure (0.1 bar, red circles). A selectivity value of 1 is shown as a green dashed line. Estimations for available errors in selectivity are shown by the appropriate error bars, calculated using the root mean squared method. The PSD for CCD is shown as a black dashed line in arbitrary units.

Thus, as a preliminary conclusion, CCD shows slight selectivity towards i-octane at 420 K throughout the whole pressure range considered, aside from a low pressure region (less than 0.25 bar). This behaviour can be seen as a cumulative result across the PSD, where we see high selectivity in the 9 to 11 Å pore range and essentially no selectivity in larger pores. Similar trends are observed for IVD, indicating some universality of these effects across different classes of deposits. It is interesting to speculate on the strong sensitivity that selectivity trends have on the microporous structure of the sample. For example, if the main micropore-peak of the PSD for CCD was shifted slightly to the right and so excluding the narrow pores that i-octane is unable to fit in, the sample selectivity at low pressures would likely be reversed, showing strong selectivity for i-octane that reduced with pressure. Conversely, a larger shift to the right might include the 13 - 14 Å range where n-heptane is again favourable adsorbed, changing the selectivity again. We will return to the consequence of this high sensitivity of selectivity properties for the whole study later in the chapter.

6.2.2.2 Binary System II: i-Octane and Toluene

Figure 6.7 shows the adsorption and selectivity isotherms for the 50 : 50 (by liquid volume at ambient temperature) binary mixture of i-octane : toluene on CCD at 420 K. Again we focus only on CCD results, with the IVD showing very similar trends, qualitatively. The figure shows a higher loading for i-octane at low pressures, indicated by the "knee" on the isotherm for i-octane, before the adsorption of toluene exceeds this at around 0.5 bar. This mixture is not equimolar (mole fraction ratios are 0.31 : 0.69, for i-octane : toluene), and so to obtain a true understanding of any preferential adsorption we look to the selectivity of the system, shown on the right of Figure 6.7. In contrast to the i-octane : n-heptane system, we see a pronounced selectivity towards i-octane which reduces with pressure. The lack of plateau in the selectivity indicates that pressure plays a more important role in the selectivity between i-octane and toluene, and the packing effects of toluene cause it to be more favourably adsorbed at higher pressures.

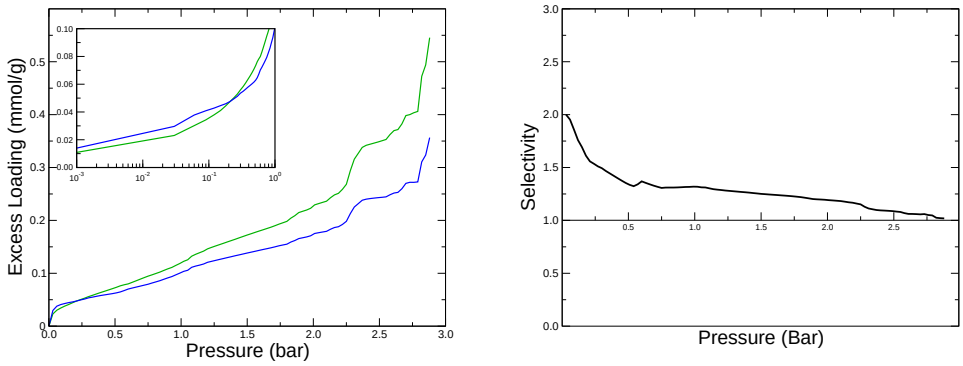

Figure 6.7: On the left: Predicted adsorption isotherms for binary i-octane (50 %, blue line) and toluene (50 %, green line) mixture in CCD at 420 K. Low pressure region with a logarithmic scale for pressure is shown in the inset. On the right: Selectivity in the binary i-octane : toluene system as a function of pressure for CCD at 420 K.

In order to explore these trends, we provide a similar analysis of selectivities as a function of pore width, super-imposed with the PSD for the CCD sample. Figure 6.8 shows this selectivity for the binary i-octane : toluene system for CCD at 420 K. In the same manner as that for i-octane : n-heptane system, both high (black circles, 2.9 bar) and low (red circles, 0.1 bar) are shown. The green dashed line indicates the

neutral selectivity threshold and the CCD PSD is overlayed as a black dashed line. Several interesting trends can be identified for analysis. At low pressure, selectivity towards i-octane is again very strong in the narrow micropore range. This decreases with pore width, but remains slightly favourable towards i-octane in the wider pores shown. At higher pressures selectivity across all pore sizes drops. This is particularly evident in narrow pores which become selective towards toluene at higher pressures due to packing effects. In larger pore widths, no selectivity is observed at higher pressures, however compared to low-pressure behaviour of mesopores, the region becomes less favourable towards i-octane at higher pressure leading to the overall diminished selectivity.

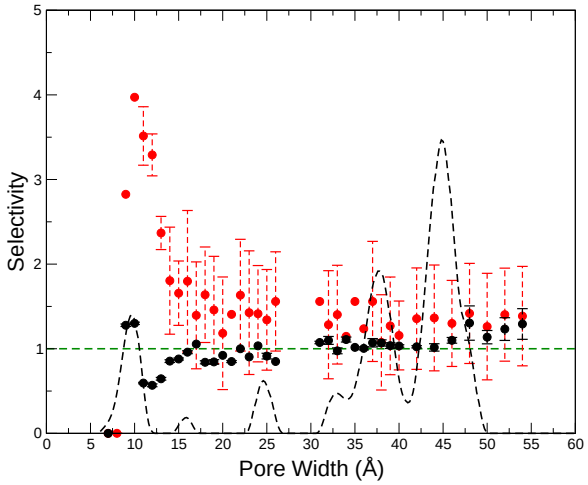

Figure 6.8: Selectivity of i-octane over toluene in a 50 :50 mixture (on a liquid volume basis) at 420 K as a function of pore width for high (2.9 bar, black circles) and low pressure (0.1 bar, red circles). Selectivity value of 1 is shown as a green dashed line. Estimations for available errors in selectivity are shown by the appropriate error bars, calculated using the root mean squared method. The PSD for CCD is shown as a black dashed line in arbitrary units

In Chapter 4 we have already spent some time on detailed analysis of the selectivity in binary mixtures of i-octane and n-heptane as a function of pore width. Results for toluene are, however, introduced in this chapter for the first time and therefore we would like to diverge for a moment from the main course of the section to explore effects in Figure 6.8 in more detail.

Let us start with low pressure set of points first. Consider the pore range between 9 and 11 Å. At low pressure we see that the system exhibits high selectivity towards

i-octane, again as a result of a particularly nice match between the size of i-octane and the width of the pore leading to very favourable interactions. As pore size increases slightly (from 10 - 20 Å), there is a decrease in selectivity, but the trend is more gradual than in the i-octane : n-heptane system.

In larger pores (but still at low pressure), selectivity remains slightly in favour of i-octane, with a value around 1.5. The noticeable selectivity of i-octane over toluene here is a result of the higher values in Henry's constants and generally stronger interaction of i-octane with the slit pores.

At high pressure we see an overall shift in selectivity towards toluene for all pore sizes shown. Narrow pores show several shifts in selectivities; 7 and 8 Å pores exhibit infinite selectivity towards toluene as i-octane is unable to fit in the narrow pores, we then see a slight preference for i-octane for the 9 and 10 Å pores before the remaining micropores show selectivity towards toluene. This is an interesting change in behaviour, and the preference towards i-octane in 9 and 10 Å pores could be an example of the "length entropy effect" reported by Krishna et al.[81] While we might expect toluene to exhibit more efficient packing, and so be favourably adsorbed at high pressure, in these pores, only a single layer of both i-octane and toluene is able to form. In such geometry, packing effects become more two dimensional, and the shorter molecules are able to pack more efficiently (see reference to Krishna et al.[81]). We speculate that the 2D foot print of i-octane is not much larger than that of toluene, and so the packing efficiency of toluene is lost. Adsorption is then swayed by the stronger interaction potentials (despite being in a high-loading regime) and so slight selectivity in favour of i-octane is observed for these two specific pores.

For the remaining micropore range (11 - 20 Å) we see the selectivity towards towards toluene decaying to no selectivity in larger pores. An argument can be constructed where, at high pressures, packing effects become more dominant and the rigid, compact toluene is able to form denser and more efficient molecular arrangements than the bulk, branched i-octane. This is particularly pronounced in the 11 Å pore where toluene is able to form a double layer of molecules, while i-octane is still confined to a single layer in the pore centre. This is shown in the density profiles in Figure 6.9. As the pore width increases further, the selectivity approaches one. This suggests that the strong selectivity towards toluene seen in narrow pores (at high pressures) is a result of i-octane being unable to form multiple layers in narrow pores, where as toluene can. This advantage for toluene is lost as the extent of confinement is reduced. This explains why in large mesopores there is again a slight preference

for i-octane at 2.9 bar.

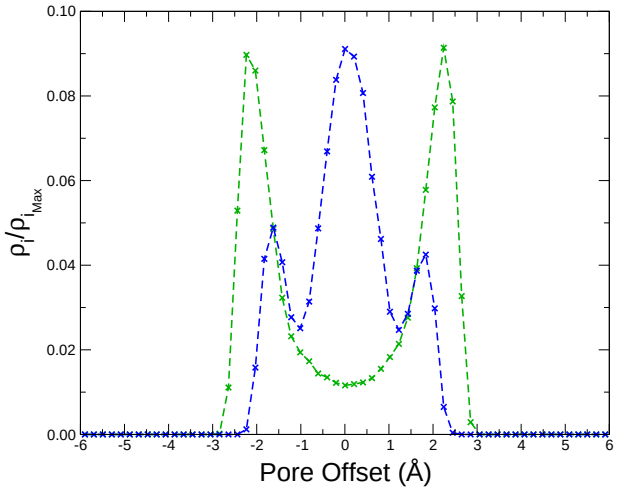

Figure 6.9: Density profile of a 12 Å pore for i-octane (blue dashed line with blue crosses) and toluene (green dashed-line with green crosses) at 2.88 bar. The majority of i-octane is found in the centre of the pore, although the profile features three peaks in density. Two distinct layers of toluene can be seen. Density is given in reduced units of $\rho/\rho_{\mathrm{i_{max}}}$, where $\rho_{i_{max}}$ is the total density of species i in the pore, the density profile essentially shows the chance of observing a molecule in a given cross-section of the pore.

We are able to relate the selectivity in pores (Figure 6.8) to the overall system selectivity seen in Figure 6.7. We can see that at low pressures, individual pores across all the pore range favour i-octane. In narrow pores this selectivity is exacerbated by the overlapping influence of the pore walls. As these pores tend to dominate behaviour at low pressure, we see a large initial selectivity towards i-octane in Figure 6.7. As pressure increases, two changes take place: the system behaviour becomes more influenced by larger pores as species condense, and the narrow pores (already having undergone complete filling) begin to switch their selectivity towards toluene due to packing effects. The result is a gradual decrease in the system selectivity. At maximum pressure, the mesopores influence the system behaviour the most, and so the system tends towards having no particular selectivity. While the micropores are selective towards toluene, their influence at higher pressure is diminished due to the adsorption processes taking place predominantly in the mesopores .

6.2.2.3 Binary System III: Toluene and n-Heptane

The remaining of the three binary systems in our analysis is that of toluene : n-heptane. The adsorption and selectivity isotherms for this system are shown in Figure 6.10. The isotherm on the right shows the selectivity of toluene over n-heptane. Selectivity below one at low pressure indicates a preference towards n-heptane, but this reverses and at high pressure a slight selectivity towards toluene is found.

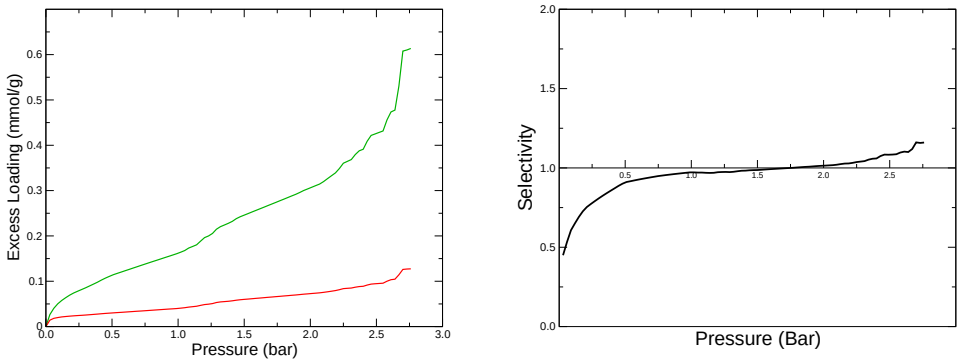

Figure 6.10: On the left: predicted adsorption isotherms for binary toluene (75 %, green line) and n-heptane (25 %, red line) mixture in CCD at 420 K. On the right: selectivity in the binary toluene : n-heptane system as a function of pressure for CCD at 420 K.

The selectivity of toluene over n-heptane as a function of pore width at both low (0.1 bar) and high (2.8 bar) pressures is shown in Figure 6.11. The green dashed line indicates selectivity equal to one and the PSD for CCD is overlayed as a black dashed line. At low pressure we see a selectivity towards n-heptane due to stronger interactions with the pore walls. This selectivity is fairly constant across all the pore sizes considered. At higher pressures, the band of narrow pores around 10 Å see a spike in selectivity towards toluene, while the remaining pore range shows only a slight preference for toluene for the remaining pore range. This is quite interesting, in previous systems we saw selectivity behaviour in this pore range associated with species being able to form double layers in pores of different sizes. In this case, toluene and n-heptane can form double layers at the same time, and so is not the cause of the selectivity effects. There must be some advantage that toluene holds over n-heptane in this narrow pore range, allowing a more efficient packing. We may

speculate that this could also be a result of the system composition, similar to what was suggested for the i-octane : n-heptane system, but in general, this issue requires further investigation.

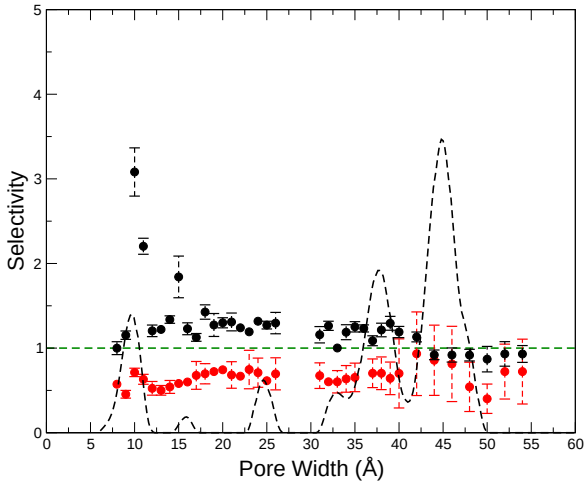

Figure 6.11: Selectivity of toluene over n-heptane in a 75 :25 mixture at 420 K as a function of pore width for high (2.8 bar, black circles) and low pressure (0.1 bar, red circles). Selectivity value of 1 is shown as a green dashed line. Estimations for available errors in selectivity are shown by the appropriate error bars, calculated using the root mean squared method. The PSD for CCD is shown as a black dashed line in arbitrary units.

In the same process as the previous two systems, we are able to relate the behaviour in individual pores to the overall behaviour in Figure 6.10 via PSD analysis. At low pressures we see n-heptane favourably adsorbed across all pores, and obviously the overall adsorption behaviour will favour n-heptane as well. As pressure increases we see a shift in the selectivity towards toluene in all pore sizes. As every pore exhibits a selectivity shift towards toluene, the system reflects this as a whole and the system becomes selective towards toluene. It is worth noting that the selectivity of toluene is particularly emphasised for narrow micropores, seen by the peak in selectivity around 10 Å in Figure 6.11. This peak coincides with the micropore peak in the PSDs, however the influence is lessened because at high pressures (where the selectivity peak is seen) adsorption is dominated by the behaviour in the mesopore range. Because of this, the engine deposit shows only slight selectivity towards toluene at high pressures, in-line with the trends shown for mesopores in Figure 6.11.

6.2.2.4 Binary System Conclusions

Some clear conclusions can be formed from analysis of these systems: i-octane has stronger interactions than both n-heptane and toluene, and so tends to be more selectively adsorbed in narrow pores when pressure is low, except for very narrow pores where it does not fit any more. In addition, higher pressures favour toluene due to superior packing effects over both i-octane and n-heptane.

To complete the hierarchy, n-heptane exhibits stronger interactions than toluene, and this is reflected by preferential selectivity of n-heptane over toluene at low pressure. It is difficult to comment on the packing order between n-heptane and i-octane as unexpected behaviour was observed for the i-octane : n-heptane in larger mesopores. In these pores, high pressure increases selectivity towards i-octane rather than n-heptane, contradicting previous observations in the literature. In addition, selectivity towards the more strongly interacting n-heptane was not found at low pressures. This suggests i-octane holds some packing advantage that negates the expected dominance of the linear n-heptane, or there is some unknown effect arising from the system composition. While this was investigated more extensively, no satisfactory conclusion could be obtained and this must be left as the subject of further research.

Other interesting selectivity effects were also observed. At high pressure, toluene shows high selectivity over i-octane in the micropore range, a range of pore sizes that are typically dominated by more strongly interacting species. In this case, toluene is able to form a double layer of molecules in narrow pores where i-octane can only fit a single layer of molecules. Toluene also showed a similar peak in selectivity over n-heptane for a similar range of micropores. This is unexpected and can not be explained on the grounds of toluene forming a double layer in narrow pores, as in this pores n-heptane is also able to form a double layer. Further investigation is required to explore packing effects in these systems, particularly arising from the two components co-adsorbing in the pore.

6.2.2.5 A note on Selectivity Errors

It is difficult to comment on the error in selectivity across the solid as a whole. While the error for individual pores is quite a simple affair, assessing the contribution in line with both the PSD, and the shift of importance between micro and mesopores creates a complex and delicate situation. The overall error of the system is now dependent

on the error in individual pores and the distribution of such pores across the solid (i.e. the PSD). The influence of certain pores, however, will change depending on which pressure regime is considered.

An indication of the reliability for each part of the selectivity isotherm can be gained by assessing under what conditions errors in pore regimes are large or small. While estimations of the errors in selectivities are shown in Figures 6.6, 6.8 and 6.11, here we focus on selectivities in two example pores to assess the impact of different pore regimes. The root mean squared errors in selectivity for each binary system at 420 K have been calculated in two pore sizes, 10 and 40 Å, (11 and 40 Å in the case of the i-octane : toluene system) at low and high pressure (see table for exact values). These errors are calculated from the variation in component loadings for each system. The results are presented in Tables 6.1, and further details on the methodology of calculation can be found in Appendix E.

	i-Octane : n-Heptane		Toluene : n-Heptane	
	0.1 Bar	3.6 Bar	0.1 Bar	2.8 Bar
10Å	11 %	10 %	6 %	9 %
40Å	25 %	4 %	60 %	6 %

	i-Octane : Toluene	
	0.1 Bar	2.9 Bar
11Å	8 %	10 %
40Å	36 %	1 %

Table 6.1: The table on the top shows errors in selectivity for 10 Å and 40 Å pores at low and high pressures for systems of i-octane : n-heptane and toluene : n-heptane. The table on the bottom shows errors in selectivity for the binary system of i-octane : toluene at 11 Å and 40 Å pores, at high and low pressure.

From Table 6.1 we can see that errors in selectivity tend to be constant across the narrower 10 Å pore, this is because the pore fills at low pressures, after which the loading does not deviate significantly. In larger pores we can see that the errors are initially quite large, much larger than those in the narrow pores. However, at higher pressures the error in mesopores is much lower, a result of better statistical certainty from having more molecules adsorbed. As mentioned, at low pressure it is usually the narrow micropores that dictate adsorption trends, and from Table 6.1 we can expect errors around 10 % in these conditions. As pressure increases, influence

shifts to the mesoporous range, which tend to exhibit lower errors, less than 5 %.

6.2.3 Selectivity in Binary Systems on IVD

For completeness, Figure 6.12 shows adsorption isotherms and associated selectivities for the binary systems on IVD at 390 K. The previous section showed that selectivity effects in CCD are more sensitive to the microporous region than the mesoporous, while Figures 5.5 and 5.8 (Chapter 5) show that the main differences between the IVD and CCD structures lie in the mesoporous range; the microporous regions are quite similar. Because of this, adsorption behaviour between the two structures are quantitatively similar. As a result, no further selectivity analysis will be done for the IVD systems, as the conclusions drawn from CCD are equally applicable here. It is somewhat interesting to consider the implications of the selectivity sensitivity; what effects would arise from a shift in the microporous region, and how does pore structure change from deposit to deposit? While our studies suggest that the variation between deposits is minimal, the pool of deposit samples is presently quite small, and expanding this to increase the confidence of such statements is worthy of future consideration.

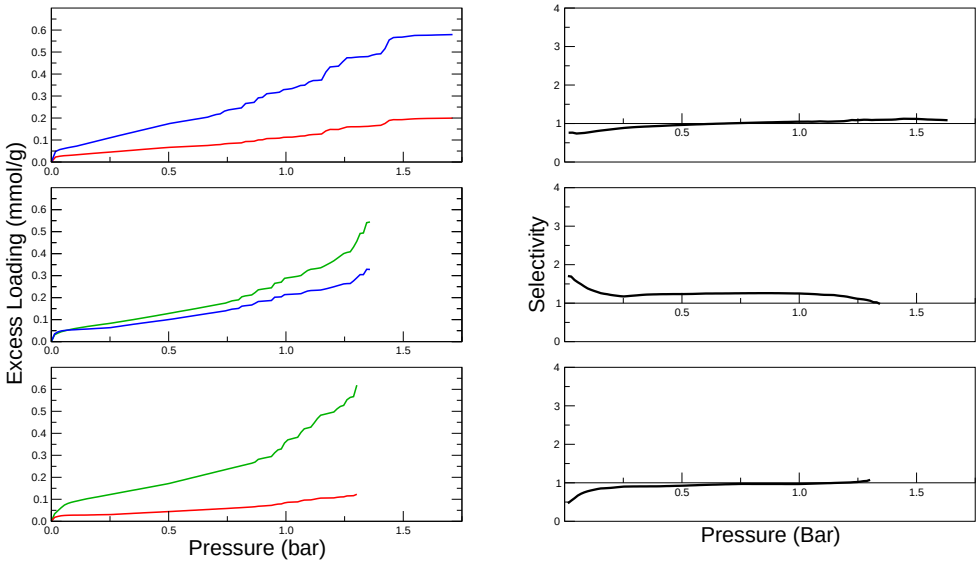

Figure 6.12: Predicted adsorption isotherms for binary mixtures on IVD at 390 K (left panel) and the associated selectivity isotherm (right panel). From top to bottom, the binary mixtures are: From top to bottom binary mixtures are: i-octane(75 %) / n-heptane (25 %); i-octane(50 %) / toluene(50 %); and n-heptane (25 %) / toluene(75%); i-octane is shown in blue, n-heptane in red and toluene in green, respectively. Selectivity isotherms are shown in black.

6.3 Ternary Systems

Finally we consider the ternary mixture of i-octane, toluene and n-heptane. The ratios of this blend were based on the same fuel specification[73] and corresponds to 3:3:1 (by liquid volume), respectively. Results for the adsorption predictions in IVD and CCD are shown in Figures 6.13 and 6.14 respectively. To assess the possible effect of selective adsorption on engine operation, we perform selectivity analysis of these isotherms by grouping toluene and i-octane into one, high octane species. Adsorption selectivity of this species over n-heptane is shown in Figures 6.13 and 6.14 for IVD and CCD respectively. It is interesting to note that the deposits exhibit slight selectivity towards the higher octane species at higher pressures. At low pressure, the selectivity is towards the linear n-heptane. Both deposits exhibit similar trends, indicating that this trend can be considered quite general, irrespective of the type of the deposit under relevant conditions.

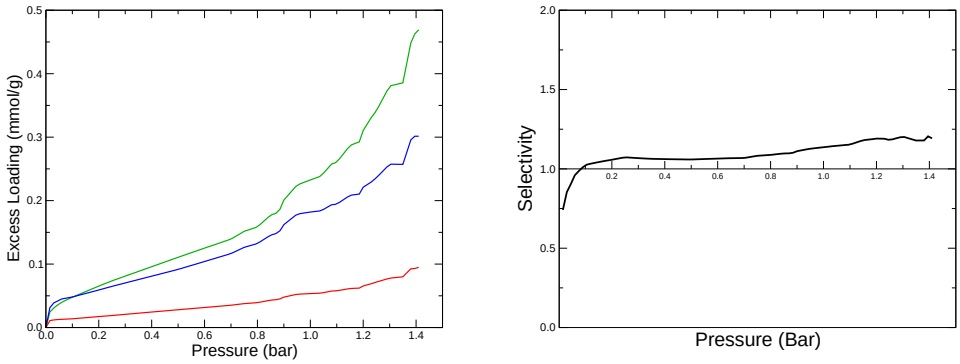

Figure 6.13: On the left: predicted adsorption isotherms for a ternary mixture of i-octane (blue line), toluene (green line) and n-heptane (red line) in IVD at 390 K. Ratios are on a liquid volume basis, and correspond to 3 : 3 : 1 for i-octane, toluene and n-heptane respectively. On the right: selectivity of combined i-octane and toluene species over n-heptane in the same system.

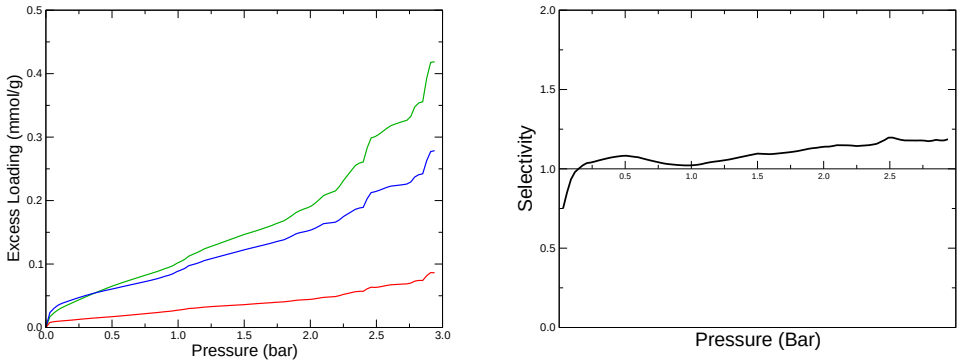

Figure 6.14: On the left: predicted adsorption isotherms for a ternary mixture of i-octane (blue line), toluene (green line) and n-heptane (red line) in CCD at 420 K. Ratios are on a liquid volume basis, and correspond to 3 : 3 : 1 for i-octane, toluene and n-heptane respectively. On the right: selectivity of combined i-octane and toluene species over n-heptane in the same system.

6.4 Impact on Engine Operation: Adsorption Uptake Studies

In this section we set aside selectivity effects and turn to the issue that was the driving force of this project: to what extent do engine deposits adsorb components of the fuel under engine conditions. Towards this goal we perform several simple calculations involving the predicted adsorption isotherms in order to give estimated quantities for the degree of adsorption uptake that we might expect in a working engine. This allows us to give the original speculations of Costa and co-workers (that the amount of hydrocarbons adsorbed in engine deposits, under static pressure and temperature conditions, is substantial and may have a direct impact on the operation of the engine) a more quantitative footing.

In these calculations we estimate the amount of fuel injected per cylinder, and use this to estimate the adsorption extent under different conditions. We consider each alkane in turn, and assume a fuel that is comprised 100 % of the relevant alkane. Other assumptions include: the system pressure at fuel injection is 1 atm, all of the fuel is vaporised, and the pre-combustion mixture of the fuel and air follows the ideal gas law. We consider a 2.0 L, four cylinder engine, with the volume of a single cylinder given by: $V = 0.5\,L = 0.5 \times 10^{-3}\,m^3$. It should be noted that no account was taken of possible fuel uptake by other deposits during the engine cycle; the CCD calculations were made assuming 100% of the injected fuel reached the combustion chamber, whereas in reality we would expect some of this to be adsorbed by the IVD beforehand. The amount of injected fuel is given by:

$$n = \frac{PV}{RT}\, y_{alkane}$$

where P is pressure, V is cylinder volume, R and T are the gas-constant and temperature at fuel injection, and y_{alkane} is the mole fraction of the alkane in the corresponding combustion reaction. The fuel is introduced together with the air in a stoichiometric air to fuel ratio, corresponding to the following combustion reactions for i-octane, n-heptane and toluene:

$$
\begin{aligned}
12.5\,O_2 + 47\,N_2 + C_8H_{18} &\rightarrow 8\,CO_2 + 9\,H_2O + 47\,N_2 \\
11\,O_2 + 41.36\,N_2 + C_7H_{16} &\rightarrow 7\,CO_2 + 8\,H_2O + 41.36\,N_2 \\
9\,O_2 + 33.84\,N_2 + C_7H_8 &\rightarrow 7\,CO_2 + 4\,H_2O + 33.84\,N_2
\end{aligned}
$$

The mole fractions are then given by:

$$
\begin{aligned}
y_{C_8H_{18}} &= \frac{1}{12.5 + 47 + 1} &&= 0.017 \\
y_{C_7H_{16}} &= \frac{1}{11 + 41.36 + 1} &&= 0.019 \\
y_{C_7H_8} &= \frac{1}{9 + 33.84 + 1} &&= 0.023
\end{aligned}
$$

We begin by considering the adsorption extent for both CCD and IVD at 1 bar and the respective temperatures of 420 K and 390 K, shown in Table 6.2. The values for adsorption loading are read from the single component adsorption of the appropriate system, which was presented previously in this chapter (Figure 6.1). Note that we are interested in system pressures of 1 bar, however the partial pressure of a single component is obtained from the alkane mole fraction via $P_{partial} = y_{alkane} \cdot P_{total}$.

	Injected Fuel (mmol)	Partial Pressure (Bar)	CCD at 420 K, 1 bar		IVD at 390 K, 1 bar	
			Loading (mmol/g)	Total Fuel Adsorbed (%)	Loading (mmol/g)	Total Fuel Adsorbed (%)
i - Octane	0.26	0.017	0.023	9	0.053	21
n - Heptane	0.29	0.019	0.023	8	0.057	19
Toluene	0.36	0.023	0.030	8	0.063	18

Table 6.2: Calculated data for the adsorption uptake of i-octane, n-heptane and toluene in CCD at 420 K and IVD at 390 K, and 1 bar. Calculations are made assuming the fuel is exclusively comprised of the alkane in question. Adsorption loadings were read from the single-component isotherms presented in Figure 6.1. For a sample calculation, and details on other assumptions, see text.

Temperature and pressure conditions within the combustion chamber are highly transient, and we know from the engine profile in Chapter 1 (Figure 1.8) that 1 bar is the lowest pressure from the range that CCD is exposed to. As an extreme example,

we can consider the adsorption extent at the maximum pressure that the combustion chamber reaches, and so we perform similar calculations at a pressure of 19 bar and temperature of 420 K. We note that at the point where pressure reaches 19 bar, the temperature of the gas in the combustion chamber reaches 2400 K due to flame propagation (see Figure 1.8, Chapter 1). Adsorption at this high temperature must be negligible, however we may argue that the surfaces of the engine (where engine deposits accumulate) remain at a fairly constant and much lower temperature due to the engine cooling system.[4] It is not unreasonable to assume that while pressure may fluctuate quite dramatically, the temperature of the deposits will remain much lower than those shown in Figure 1.8. We also note that although the conditions for adsorption have changed, the amount of fuel was injected prior to entering the combustion chamber, and so remains the same. Calculations at this elevated pressure are shown in Table 6.3.

	Injected Fuel (mmol)	Partial Pressure (Bar)	CCD at 420 K, 19 bar	
			Loading ($^{mmol}/_{g}$)	Amount Fuel Adsorbed (%)
i - Octane	0.26	0.314	0.101	39
n - Heptane	0.29	0.356	0.108	37
Toluene	0.36	0.433	0.131	37

Table 6.3: Calculated data for the adsorption of i-octane, n-heptane and toluene at a high-pressure scenario of 19 bar in CCD at 420 K. Calculations are made assuming the fuel is exclusively comprised of the alkane in question. Adsorption loadings were read from the single-component isotherms presented in Chapter 6. For an sample calculation, and details on other assumptions, see Section **??**.

From Table 6.2 we can see that the original speculations of Costa and co-workers were correct; the adsorption of 19 and 21 % (per gram) of the total fuel injected into the engine for i-octane and n-heptane is quite a significant proportion. The calculations for toluene show similar levels of adsorption. It is interesting to note that the calculations at 1 bar suggest the intake valve deposits will have a larger impact on changing the fuel composition than the combustion chamber. This is likely due to the higher temperature of the conditions within the combustion chamber. However, this temperature penalty is overcome by the much higher pressure that CCDs are exposed to during the compression stroke of the combustion cycle. While in previous studies it was thought that the IVD would have the largest impact in fuel composition,[17]

comparison of the above data suggests that the high pressure of the combustion chamber could have a larger influence. We appreciate that the values presented here are very coarse approximations and subjected to several assumptions that deviate from reality, and as such only serve to provide a qualitative idea on the adsorption extent.

6.5 Conclusions

In this chapter we have presented isotherms for the adsorption of single component systems of i-octane, n-heptane and, for the first time, toluene on both CCD at 420 K and IVD at 390 K. We found that the adsorption extent of toluene is of a similar level to that of i-octane and n-heptane: all adsorb fuel components in considerable amounts in the context of engine requirements.

Adsorption and selectivity isotherms for the binary mixtures were also presented for both CCD and IVD samples. In the case of CCD, an extensive analysis of these systems was performed, providing insight on the adsorption trends of binary alkane mixtures in slit pores. The stronger interaction potential of i-octane caused preferential adsorption in situations where interaction strengths dominated behaviour (narrow pores at low pressure, for example), and toluene was found to exhibit a more efficient packing over both i-octane and n-heptane. Some unusual selectivity trends were also observed. Large mesopores showed selectivity towards i-octane over n-heptane at high pressures, where it was expected that n-heptane would exhibit more favourable adsorption. At high pressures, toluene showed a higher selectivity over n-heptane for a band of narrow pores where overlapping interaction potentials typically enhanced adsorption for the more strongly attracted species. The peak in selectivity of toluene over n-heptane in this range is surprising. Both of these effects are unexplained and require further investigation, but suspected to be a combination of mixture composition and packing effects.

Adsorption for ternary systems of i-octane, n-heptane and toluene were also investigated. Adsorption isotherms were presented, and possible selectivity of "high-octane" species was investigated by grouping toluene and i-octane together against n-heptane. At high pressure, the selectivity shifts in favour of the "high octane" group. However, at very low pressures there is a slight preference towards n-heptane. At this point, it is important to revisit the comments we made regarding the model

for toluene interactions in Chapter 4. If indeed our current model underestimates the strength of toluene to pore wall interactions, then a more accurate model should lead to a greater adsorption of toluene and a potential shift in the selectivity trends for all binary and ternary systems. It is likely that in this case the selectivity for the grouped "high octane" species will be above one in the whole pressure range and over multiple cycles of the engine this slight preference for high octane species may lead to some additional effects in the engine operation associated with the diminished octane number.

Finally, studies into the extent of adsorption uptake of the engine deposits was investigated by calculating the amounts of i-octane, n-heptane and toluene that could be adsorbed into both IVD and CCD at conditions within the engine. Although these calculations are subject to large assumptions, they serve as a guide to the potential adsorption impact deposits can have. When compared to the amount of fuel injected into the engine, the adsorption extent of the deposits is considerable, and so we provide evidence to support the original hypothesis that the adsorption of fuel components into engine deposits has a large, detrimental impact on engine operation.

Chapter 7

Conclusions and Perspectives

In this final chapter of this thesis we summarise the original objectives in order to review how they were approached and provide a summary of the outcomes. In doing so we are able to offer some perspectives on how this research could be extended and developed further.

The objectives of this thesis are closely tied to those of previous work by Costa and co-workers. The over-arching aim of both theses is to understand to what extent engine deposits can adsorb components of gasoline fuel and their mixtures under relevant, fixed conditions of temperature and pressure. At the heart of the strategy to achieve this aim was the development of a predictive model that is able to capture the adsorptive properties of the engine deposits. This model was constructed using a combination of molecular simulations and experiments. Within this model, the structure of the deposits was first characterised in terms of a distribution of slit pores of different sizes; and second, this distribution was used to make predictions for adsorption of species and under conditions more relevant to the operation of the engine

In particular, this model allowed the prediction of the adsorption of i-octane, n-heptane and toluene in two engine deposits, CCD and IVD under relevant temperature conditions, 420 K and 390 K, respectively. These species were chosen to represent the branched, linear and aromatic classes of alkanes that make up the majority of gasoline fuel. Initial studies of single-component adsorption were complemented by studies of binary and ternary mixtures.

The key findings of the thesis can be summarised in the three main areas as follows.

Structure of the Deposits:

Structurally, the deposits mainly consist of two bands of pores, a band in the microporous region around 10 Å and a band in the lower mesoporous region between 30 and 50 Å. Exact details of the structure depend on the deposit type (a result of different formation conditions). Between the two samples studied here, CCDs have a broader range of pores that begin to transition between the micro and mesoporous range, whereas IVDs are more distinctly split into the two bands of pore sizes.

Adsorption Affinity of the Deposits:

According to our predictions, the deposits can adsorb considerable amounts of fuel components. We have shown that the three alkane classes adsorb in comparable amounts in both CCD and IVD. Adsorption uptake studies revealed that engine deposits have the potential to adsorb a substantial proportion of the fuel present in the engine. In context of the original hypothesis, this provides strong evidence that engine deposits have a detrimental impact on engine performance through fuel component adsorption.

Selectivity of the Deposits:

For the majority of the pressure range considered, deposits exhibit selectivity towards i-octane over n-heptane and toluene. The selectivity between toluene and n-heptane depends on pressure, with low pressures favouring n-heptane, and high pressures favouring toluene. Ternary systems show slight selectivity towards high octane species over n-heptane. When considering the impact on engine operation, we are interested in very low values of partial pressure, where deposits exhibit not only a slight preference towards n-heptane, but it is also very difficult to obtain accurate data due to larger statistical errors.

Finally, building towards these predictive models also allowed us to explore a number of fundamental issues associated with adsorption of alkanes and their mixtures in slit pores, capillary condensation of these species in mesopores, hysteresis phenomena and energy aspects of adsorption.

Future Prospects:

This project was the second of a new area of research using molecular simulations and predictive modelling to investigate adsorption in the highly complex environment of the combustion chamber. Having built on the previous work, and having offered some new contribution to this effort, a natural question remains: what further avenues can this research take? In the remainder of this chapter we offer some speculative ideas on possible further developments of the project. In order to address this it is important to first understand the current limitations of the model, and speculations on future research will be briefly preceded by the motivation for such a direction.

One of the key assumptions of the characterisation approach used in this model is that the porous nature of the deposits can be described by a collection of independent slit pores. However, real porous materials are complex, and feature a network of interconnected pores. Can we construct a more realistic model that is able to take into account this complex network structure?

While remaining within the realm of the slit pore model, a possible first step in this direction is the consideration of the simplest pore network. This will provide some insights on how the behaviour of pore networks differ from those of independent slit pores. The simplest network consists of two slit pores of different widths, which form a variant of an ink-bottle pore within periodic boundary conditions. During this project, initial studies ventured down this research path, and some initial adsorption isotherms are shown in Figure 7.1 as well as visualisations of i-octane, n-heptane and toluene at various stages of the isotherm (Figure 7.2). As the deposits contain two main bands in the micro and mesoporous range, two pores of 10 and 33.45 Å were chosen to form the ink-bottle junction.

From the isotherms in Figure 7.1 we can see capillary filling in the micropore, followed by capillary condensation in the larger mesopore. An interesting feature from the visualisations is how the central cavity seems almost full at 55 kPa, despite not having undergone capillary condensation. A technical challenge to consider in this line of research is the dimensions of the unitcell, as periodic boundary conditions only extend the size of the cavity along one axis, not two.

Another equally important issue is that of the system dynamics: the current model does not take into account the transient nature of the engine conditions, nor

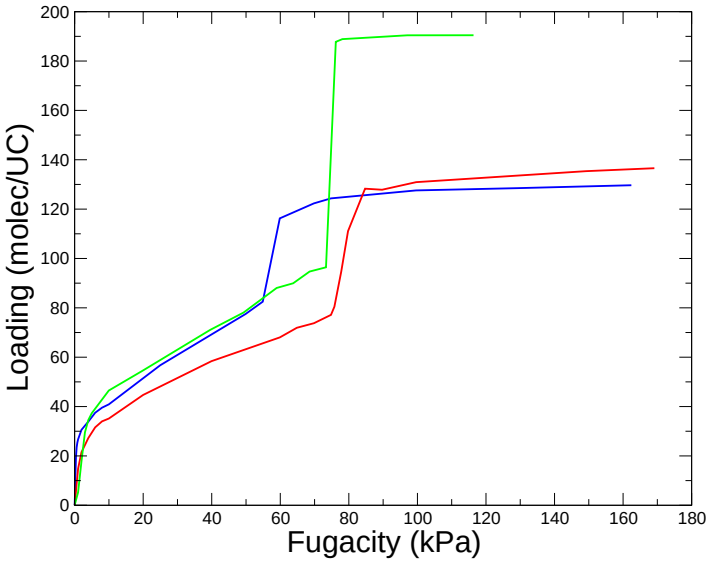

Figure 7.1: Adsorption isotherms for i-octane (blue line), n-heptane (red line) and toluene (green line) in an ink-bottle pore consisting of two adjacent pores, of 10 Å and 33.45 Å widths. Isotherms are plotted as molecules per unit-cell versus fugacity. Visualisations of the systems are shown in Figure 7.2

does it address the transport kinetics of the species within the material.

To address the simpler of these, an initial step might simply be to understand how the diffusion coefficients for different species depends upon confinement, loading, structure and composition of the system. A possible route to this is through molecular dynamics. Figure 7.3 shows the results from some preliminary studies examining the mean square displacement of i-octane, n-heptane and toluene in both 10 and 40 Å pores. From such plots it is possible to determine the diffusion coefficients for species within the confined pores, however the plots in 7.3 are unsuitable for such calculations. Typically, the initial portion of the simulation shows high scattering and smooths out into a linear regime with time, from which the diffusion coefficients can be calculated. However, these results appear to begin in a linear regime and deviate from this with time. Further investigation is required to pursue this direction of research, but the figures serve as an example starting point.

One can also consider a system setup that would more closely resemble the transient nature of the engine. Consider an example system of open slit pores surrounded by a bulk reservoir of species. A molecular dynamics simulation can be set up where

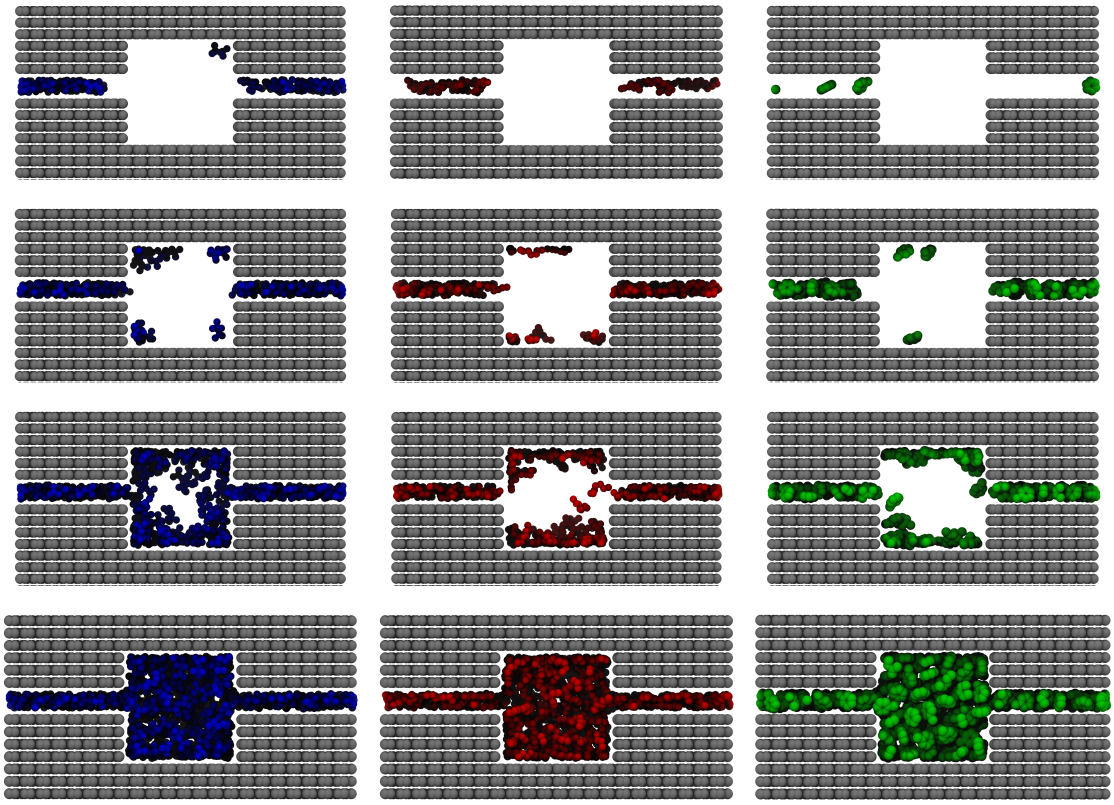

Figure 7.2: Visualisations for the single component adsorption of i-octane (left column), n-heptane (middle column) and toluene (right column) in an ink-bottle pore at 390 K. From top to bottom, the pressures of the systems are: 0.01 bar, 0.1 bar, 0.6 bar (for i-octane, the system is at 0.55 bar which is just prior capillary condensation) and 1 bar.

the adsorbate molecules are initially located in the bulk phase, but are adsorbed into the slit pore structure as the simulation progresses. Visualisations from such a simulation are shown in Figure 7.4, which shows an initial bulk reservoir of n-heptane and i-octane next to several open 10 Å pores. This could be a very useful simulation as it may provide some time-scale on the uptake process as a function of structure, temperature and bulk pressure. A further advancement on this could be a simulation where both the temperature and pressure of the bulk reservoir are controlled during the simulation, allowing conditions of the system to reflect the transient nature of the engine.

The third issue is regarding the formation and consistency of the engine deposit samples themselves. All the work, both in this project and the previous by Costa

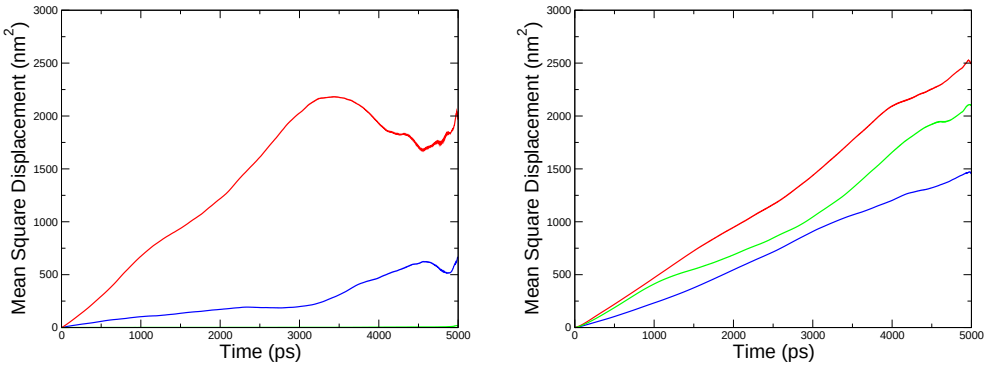

Figure 7.3: Preliminary mean square displacement results for i-octane (blue lines), n-heptane (red lines) and toluene (green lines) in a 10 Å pore (left) and 40 Å pores (right) at 420 K. Simulations were run at low loading densities, which in the 10 Å equated to 5 molecules in the 10 Å pore, and 46 molecules in the 40 Å pore.

and co-workers, is based on experimental data for adsorption in these two samples. In Chapter 4 we have alluded to the sensitivity of adsorption behaviour in the microporous region, and speculated on changes in selectivity behaviour with small shifts in the location of these micropores. Due to the large number of factors that influence deposit formation, it is unclear if the structures reported here are general trends across a wider range of deposits or not. While we may speculate that the structural trends will differ strongly with the formation factors, this can not be confirmed without further experimental results. Characterisation of a new set of sample deposits was attempted during the project, however difficulties with the limited sample size as well as unusual adsorption behaviour at high pressure prevented further characterisation.

The final issue we speculate on is regarding chemical reactions. All of the work in this project has been concerned with the physical adsorption of fuel components and combustion reactions, and reactions associated with the formation of the engine, were left out of the picture. Can we incorporate the process of deposit formation in the picture? This is a challenging problem to address, and will likely require computational quantum mechanics methods.

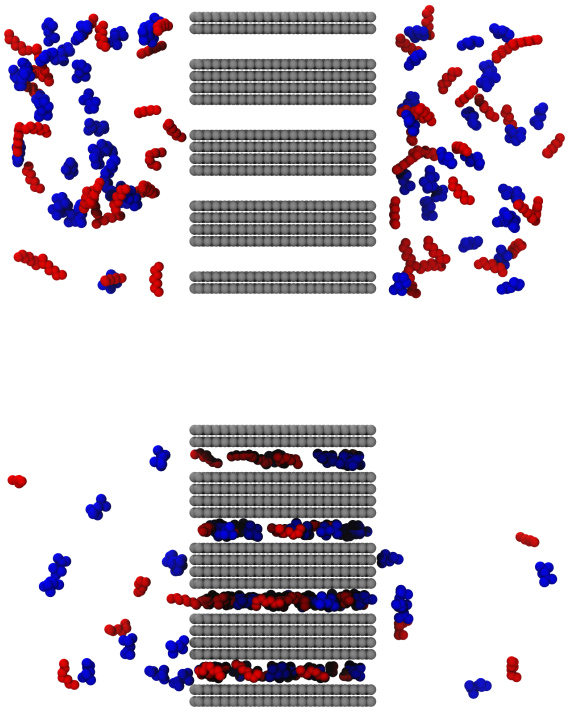

Figure 7.4: The top figure shows the initial configuration for a binary mixture of 50 i-octane and 50 n-heptane molecules in the vicinity of several 10 Å slit pores at 390 K. The bottom figure shows the final configuration of the same system after 200 nano-seconds of simulation time.

As a final, overall conclusion we can state that although the project was motivated by and focused on one very specific industrial issue, it tapped into a number of fundamental problems and outlined new directions of research, not only to the automotive industry but also for the adsorption and material science communities.

List of Publications

Conferences

1. *Oral Presentation:* A. J. Harrison, L. Sarkisov, R. Cracknell, J. Krueger-Venus, J. M. C. Pinto da Costa, and N. Seaton "Investigation of adsorption of fuel components in engine deposits" *9th International Colloquium Fuels.* Stuttgard/Ostfildern, Germany (2013)

2. *Poster Presentation:* A. J. Harrison, L. Sarkisov, R. Cracknell and J. Krueger-Venus "Computer Simulations and Experiments of Alkane Adsorption in Complex Carbonaceous Materials" *Annual World Conference Carbon.* Krakow, Poland (2012)

Journal Articles

1. A. J. Harrison, R. F. Cracknell, J. Krueger-Venus, and L. Sarkisov. "Molecular Simulation Studies of Adsorption of Gasoline Components and their Binary and Ternary Mixtures in Engine Deposits" *(In preparation for submission to Fuel)*

2. *(Calculations for)* J. Pinto da Costa, R. F. Cracknell, N. A. Seaton, and L. Sarkisov. "Corrigendum to "Towards predictive molecular simulations of normal and branched alkane adsorption in carbonaceous engine deposits"[*Carbon* 49 (2011) 445-456]" *Carbon*, 81, 854-856 (2014).

3. A. J. Harrison, R. F. Cracknell, J. Krueger-Venus, and L. Sarkisov. "Branched versus linear alkane adsorption in carbonaceous slit pores" *Adsorption,* 20(2-3):427-437 (2014)

4. A. J. Harrison, R. F. Cracknell, J. Krueger-Venus, and L. Sarkisov. "Computer Simulation Studies of Adsorption of Binary and Ternary Mixtures of Gasoline

Components in Engine Deposits" *SAE Int. J. Fuels Lubr.,* 7(3):756-761 (2014)

5. L. Sarkisov and A. J. Harrison "Computational structure characterisation tools in application to ordered and disordered porous materials" *Molecular Simulation,* 37(15):1248-1257 (2011)

List of Figures

Figure 2.6: Two stage process for the placement of the third site during the growth of an alkane chain in configurational bias Monte Carlo. The first stage, shown on the left, involves the selection of the 1 - 2 - 3 bond bending angle, θ. Trial locations are placed on a 2D circle centred on the second site. The second stage, shown on the right, involves the selection of the axial rotation about the 1-2 bond ϕ. Trial locations are placed on the rim of a cone, projecting from the second site with the 1 - 2 - 3 bond angle θ. Note that for placement of the third site, the axial angle shown is for orientation only, there is no internal energy consideration associated with this bond.

Figure 2.7: Representation of trial site locations for the placement of the fourth site during the growth of an alkane chain in configurational bias Monte Carlo. Axial rotation about the 2-3 bond cause the trial locations to be projected onto the rim of a cone, projecting from the third site. Internal energy considerations include both bond bending, as well as the torsional contribution around the 1-2-3-4 bond.

Figure 2.8: Example of two n-pentane configurations with similar internal bending energies, but different intramolecular dispersion interactions. In n-pentane, intramolecular forces arise between the first and last sites. As shown by the dashed lines, these sites are much further apart in the conformation on the right and so have weaker intramolecular interaction.

Figure 2.9: A schematic diagram showing the necessary elements and steps in the construction of predictive adsorption model. The AIE is shown in the centre (Equation 2.26). A) shows an experimental isotherm, B) shows an adsorption kernel for conditions identical to the experimental isotherm, D) shows the pore size distribution, and C) represents a predicted adsorption isotherm.

Figure 2.10: Typical L-Curve for the characterisation of a combustion chamber deposit sample taken from this work. Shape and scale are similar to those found in the literature.[17, 71, 72]

Figure 3.9: Predicted single component adsorption isotherms for CCD at 420 K (left) and IVD at 390 K (right). Blue lines are for i-octane and red lines are for n-heptane.

Figure 4.1: On the left: a schematic visualisation of the 10 Å slit pore model. Only four layers of each wall are shown, in the actual model each wall consists of six layers. On the right: united atom representations of the adsorbate species considered in this work. The first column shows, from top to bottom, i-butane, i-octane and toluene. The second column shows, from top to bottom, ethane, n-butane, n-heptane and n-octane. The size of the atoms in both panels is scaled down from the original σ values by ~30 % for better visualisation.

Figure 4.2: On the left: Schematic of an adsorption/desorption isotherm exhibiting hysteresis. The dashed and solid lines indicate the adsorption and desorption branches respectively. According to classical theories of adsorption, the adsorption branch extends into the meta-stable region while the desorption branch links the vapour and liquid phases at thermodynamic equilibrium. On the right: in the first column, a schematic showing the nucleation process during adsorption in a slit pore. In the second column, a schematic showing how the menisci move into the pore as evaporation occurs during the desorption process.

Figure 4.3: Schematic of an adsorption/desorption isotherm highlighting the meta-stable regions of hysteresis within molecular simulations of adsorption in an infinitely long slit pore. Both adsorption and desorption branches are associated with a nucleation process, and extend into a meta-stable region (shown by dashed lines). The red line indicates the location of the true phase coexistence at pressure P_{eq}.

Figure 4.4: On the left: schematic showing hysteresis isotherms for two different temperatures, T_1 and T_2, in identical pores. Included are the meta-stable regions of the adsorption and desorption branches (black dashed lines) and the true phase coexistence pressure (red solid line). On the right: schematic showing the temperature - density phase diagram for the bulk (dashed blue line) and confined (solid blue line) fluid phase. The critical point of the confined fluid is suppressed compared to the bulk, gas - phase densities are higher, and liquid - phase densities are slightly lower compared to the bulk phase. Solid red lines indicate the two-phase coexistence, corresponding to the capillary condensation on the left, at two different temperature, T_1 and T_2. These are linked to the isotherms by the dotted red lines, and temperature T_1 is greater than T_2. As temperature is increased, the isotherm hysteresis loops on the left shrink as the coexistence curves move closer to the confined critical point.

Figure 4.5: Schematic showing how isotherm shape changes from capillary condensation towards capillary filling as the extent of confinement increases.

Figure 4.6: Adsorption isotherms (number of molecules per simulation cell as a function of pressure) for n-butane (black triangles and black lines) and i-butane (white triangles and black lines) in 10 Å slit pore at 390 K. Right panel uses the logarithmic scale for pressure.

Figure 4.7: Adsorption isotherms (number of molecules per simulation cell as a function of pressure) for n-butane (black triangles and black lines) and i-butane (white triangles and black lines) in 20 Å slit pore (left panel) and 40 Å slit pore (right panel) at 390 K.

Figure 4.8: Adsorption isotherms (number of molecules per simulation cell as a function of pressure) for n-heptane (red lines) and n-octane (black lines) and i-octane (blue lines) in 10 Å slit pore at 390 K. Right panel shows the data using the logarithmic pressure scale.

Figure 4.9: Visualisation snapshots of i-octane (left) and n-heptane (right) at high loadings in a 10 Å pore. Two layers of graphene out of six constituting the walls of the pore are shown. In both panels the size of the pore atoms are scaled down from the original σ by ~30 % for better visualisations. Species atoms remain unscaled.

Figure 4.10: Adsorption and desorption isotherms (number of molecules per simulation cell as a function of pressure) for n-heptane (red solid line for adsorption, red dashed line for desorption), n-octane (black solid line for adsorption, black dashed line for desorption) and i-octane (blue solid line for adsorption, blue dashed line for desorption) in a 20 Å slit pore (left panel) and a 40 Å slit pore (right panel) at 390 K. On the left, the initial adsorption in 20 Å pore is expanded in the inset.

Figure 4.11: Adsorption and desorption isotherms (number of molecules per simulation cell as a function of relative pressure) for n-heptane (red solid line for adsorption, red dashed line for desorption), n-octane (black solid line for adsorption, black dashed line for desorption) and i-octane (blue solid line for adsorption, blue dashed line for desorption) in a 40 Å slit pore at 390 K.

Figure 4.12: Adsorption isotherms for a binary mixture of n-heptane (red line) and i-octane (blue line) in a 10 Å slit pore at 390 K. The mixture corresponds to a 0.89 mol fraction of i-octane. Right panel shows the data using the logarithmic pressure scale.

Figure 4.13: Adsorption isotherms for a binary mixture of n-heptane (solid red lines) and i-octane (solid blue lines) in a 20 Å pore (left panel) and a 40 Å pore (right panel) at 390 K. The mixture corresponds to a 0.89 mol fraction of i-octane. For 40 Å pore desorption, hysteresis is also shown via dashed red lines for n-heptane, and dashed blue lines for i-octane.

Figure 4.14: Selectivity adsorption isotherms for i-octane : n-heptane mixture at 390 K (composition of the mixture corresponds to 0.89 mol fraction of i-octane). Closed black circles are for a 10 Å pore, open black circles are for a 20 Å pore, and open blue circles are for a 40 Å pore. Root mean squared error bars are shown for 20 and 40 Å pores as black and blue lines respectively.

Figure 4.15: Selectivity of i-octane over n-heptane in a 75 : 25 (by liquid volume at ambient temperature) mixture at both 420 K (left) and 390 K (right) as a function of pore width for available pore sizes. Both high (3.6 bar for 420 K, 1.7 bar for 390 K) and low pressures (0.1 bar in both cases) are shown as black and red circles respectively. A selectivity value of one is shown as the green dashed line. Selectivity values above one indicate a preference for i-octane, selectivity values below one indicate a preference for n-heptane.

Figure 4.16: Density profiles for the binary mixture of i-octane (blue dashed line) and n-heptane (red dashed line) in a 12 Å pore at 3.6 bar. Iso-octane molecules mainly form a single layer in the centre of the pore, while n-heptane is able to form a double layer.

Figure 4.17: Henry's constants of adsorption as a function of pore width for the microporous range on the left, and mesoporous range on the right, both at 420 K. Blue dashed line with open blue circles shows i-octane, red dashed line with open red circles shows n-heptane and green dashed line with open green circles shows toluene.

Figure 4.18: Isosteric heats of adsorption for single-component systems as a function of pore width at 420 K. Each panel represents a different degree of loading, and in each case i-octane is represented in blue, n-heptane in red and toluene in green. The top-left panel shows energies at zero loading; the energy of a single molecule is considered in each pore. In this panel isosteric heats of adsorption for each species are represented as dashed lines. Panels in the top-right, bottom-left and bottom-right show isosteric heats of adsorption at 0.1 bar, 0.5 bar and ~2 bar respectively (2.12 bar for n-heptane, 2.0 bar for toluene and 2.13 bar for i-octane). Data points for these three panels are represented by open circles. The dashed vertical lines (dark green) indicate example pores for which pressure profiles are shown in Figures 4.20 and 4.21.

Figure 4.19: Standard entropy of adsorption as a function of pore width for i-octane (blue line, open circles) n-heptane (red line, open circles) and toluene (green line, open circles). Results were calculated using the accessible pore volume.

Figure 4.20: Isosteric heats of adsorption for single-component systems in a 10 Å (left) and 15 Å (right) pore as a function of pressure at 420 K. Species shown include i-octane (blue open circles), n-heptane (red open circles) and toluene (green open circles).

Figure 4.21: Isosteric heats of adsorption for single-component systems in a 20 Å (left) and 40 Å (right) pore as a function of pressure at 420 K. Isosteric heats of adsorption for species shown include i-octane (blue open circles), n-heptane (red open circles) and toluene (green open circles). Excess adsorption isotherms are also included for i-octane (dashed blue line), n-heptane (dashed red line) and toluene (dashed green line) to highlight association between capillary condensation and step-increases in isosteric heats of adsorption. Units for the excess adsorption loading are arbitrary.

Figure 5.1: The graph at the top shows the set of adsorption isotherms used for the construction of the original ethane kernel at 278 K. Open circles depict simulated pressure points, lines are to guide the eye. Pores highlighted in red are, from left to right, pore widths of 20, 30 and 40 Å. The isotherm highlighted in blue is the 80 Å pore, and shows a reasonable threshold above which adsorption isotherms become linear within this pressure range. Interpolation between the simulated isotherms allows the construction of the ethane kernel, which is shown on the bottom. Interpolated pressure points are not shown. This kernel was used by Costa et al. in the original characterisation of both CCD and IVD.

Figure 5.2: Top: Original set of simulated isotherms used for the prediction of n-heptane at 420 K, by Costa and co-workers.[39] Adsorption isotherms in slit pores of widths present in the PSD for CCD are shown in blue. Isotherms in black represent pores not present in the CCD PSD. Isotherms shown as blue lines with open blue triangles represent, from higher loading to lowest, adsorption in pores of 40, 50 and 60 Å respectively. Bottom: Original PSD (black line) for CCD structure. Pores present in the set of simulated n-heptane isotherms are shown in green dashed lines.

Figure 5.3: Simulated adsorption isotherms for ethane at 278 K in, from highest loading to lowest, 60, 80, 100 and 200 Å pores. The linear nature of pores above 60 Å is the justification for using it as the upper bound for the window or reliability.

Figure 5.4: Sets of simulated adsorption isotherms for ethane at 278 K used for calculating the pore size distributions. The original set from the work of Costa and co-workers is shown in the upper graphic, the more detailed set, with the described improvements, is shown in the bottom graphic. Isotherms shown in blue correspond to pores in the range between 30 Å and 60 Å, a range of pores now known to be present on the PSDs. Pores between w_{upper} (60 Å) and w_{max} (800 Å) were removed as they lie beyond the window of reliability.

Figure 5.5: Pore size distributions for CCD-I (dashed line) and CCD-II (solid line).

Figure 5.6: Experimental adsorption isotherm for ethane at 273 K on CCD by Costa and co-workers[39] shown by open blue diamonds and blue line. Adsorption isotherms of slit pores including 10, 20, 30, 40, 50 and 60 Å pores are shown as closed circles, closed squares, closed triangles, open circles, open squares and open triangles respectively. A pressure range of interest is highlighted by dashed green lines, details of which can be found in the text.

Figure 5.7: Experimental adsorption isotherm for ethane at 273 K on CCD by Costa and co-workers[39] shown by open blue diamonds and blue line. Adsorption isotherms of ethane in slit pores of widths 30, 32, 34, 36, 38 and 40 Å are shown as closed circles, closed squares, closed triangles, open circles, open squares and open triangles respectively. A pressure range of interest is highlighted by dashed green lines, details of which can be found in the text.

Figure 5.8: Pore size distributions for IVD-I (dashed line) and IVD-II (solid line).

Figure 5.9: Panel on the left shows the improved adsorption kernel for n-heptane at 420 K. Panel on the right shows predictions of n-heptane adsorption on CCD. The dashed line shows original results from Costa and co-workers (original kernel integrated over CCD-I), and the solid line shows new results (new kernel integrated over CCD-II).

Figure 5.10: Prediction of n-heptane adsorption at 420 K on CCD-II, overlayed with isotherms for slit-pore adsorption in 44 and 46 Å pores (left and right black dashed lines, respectively). Steps in excess loading can be accounted for by condensation in the associated pore.

Figure 5.11: Predictions of n-heptane adsorption at 420 K on CCD-I (dashed line) and CCD-II (solid line). All predictions were made using the updated adsorption kernel for n-heptane.

Figure 5.12: Comparison of simulated adsorption isotherms for different PSD generations versus experimental isotherms for ethane on CCD. Dashed red line shows the original kernel integrated over CCD-I, solid line shows the improved kernel integrated over CCD-II. Blue diamonds show experimental measurements. Left graph shows results at 278 K, right graph shows results at 298 K.

Figure 5.13: Comparison of simulated adsorption isotherms for different PSD generations versus experimental isotherms for ethane on IVD. Dashed red line shows the original kernel integrated over IVD-I, solid line shows the improved kernel integrated over IVD-II. Blue diamonds show experimental measurements. Left graph shows results at 278 K, right graph shows results at 293 K.

Figure 5.14: Comparison of simulated adsorption predictions for different PSD generations versus experimental data for n-butane on CCD at 293 K. Dashed red line shows the original kernel integrated over CCD-I, solid line shows the improved kernel integrated over CCD-II. Blue diamonds show experimental measurements.

Figure 5.15: Comparison of simulated adsorption isotherms for different PSD generations for n-heptane (left graph, red lines) and i-octane (right graph, blue lines) on CCD at 420 K. Dashed lines show the original kernel integrated over CCD-I, solid lines shows the improved kernel integrated over CCD-II.

Figure 5.16: Comparison of simulated adsorption isotherms for different PSD generations for n-heptane (left graph, red lines) and i-octane (right graph, blue lines) on IVD at 390 K. Dashed lines show the original kernel integrated over IVD-I, solid lines shows the improved kernel integrated over IVD-II.

Figure 6.1: Predictions of single-component adsorption on IVD at 390 K (left) and CCD at 420 K (right). Predictions are shown for i-octane (blue), n-heptane (red) and toluene (green) adsorption. Insets are zoomed in on the low pressure region where initial adsorption takes place.

Figure 6.2: Henry's constants of adsorption for integrated isotherms on IVD at 390 K (left) and CCD at 420 K (right).

Figure 6.3: Predicted adsorption isotherms for binary mixtures on CCD at 420 K (left) and IVD at 390 K (right). From top to bottom binary mixtures are: i-octane(75 %) / n-heptane (25 %); i-octane(50 %) / toluene(50 %); and n-heptane (25 %) / toluene(75%); i-octane is shown in blue, n-heptane in red and toluene in green, respectively.

Figure 6.4: On the left: Isosteric heat of adsorption of a single molecule of adsorbing species with slit pore as a function of pore width at 420 K. Iso-octane is shown as a blue dashed line, n-heptane as a red dashed line and toluene as a green dashed line respectively. The CCD PSD is shown by a black line, in arbitrary units. On the right: Henry's constants of adsorption as a function of pore width for i-octane (blue dashed line, open blue circles), n-heptane (red dashed line, open red circles) and toluene (green dashed line, open green circles) at 420 K. CCD PSD is shown by a black line, in arbitrary units. The inset shows the full range of K_H for the narrow pore range from 6 - 14 Å, while the main graph shows the K_H range of interest for the larger mesopores.

Figure 6.5: On the left: Predicted adsorption isotherms for binary i-octane (75 %, blue line) and n-heptane (25 %, red line) mixture in CCD at 420 K. On the right: selectivity of i-octane over n-heptane in the binary system as a function of pressure for CCD at 420 K.

Figure 6.6: Selectivity of i-octane over n-heptane in a 75 : 25 mixture at 420 K as a function of pore width for high (3.6 bar, black circles) and low pressure (0.1 bar, red circles). A selectivity value of 1 is shown as a green dashed line. Estimations for available errors in selectivity are shown by the appropriate error bars, calculated using the root mean squared method. The PSD for CCD is shown as a black dashed line in arbitrary units.

Figure 6.7: On the left: Predicted adsorption isotherms for binary i-octane (50 %, blue line) and toluene (50 %, green line) mixture in CCD at 420 K. Low pressure region with a logarithmic scale for pressure is shown in the inset. On the right: Selectivity in the binary i-octane : toluene system as a function of pressure for CCD at 420 K.

Figure 6.8: Selectivity of i-octane over toluene in a 50 :50 mixture (on a liquid volume basis) at 420 K as a function of pore width for high (2.9 bar, black circles) and low pressure (0.1 bar, red circles). Selectivity value of 1 is shown as a green dashed line. Estimations for available errors in selectivity are shown by the appropriate error bars, calculated using the root mean squared method. The PSD for CCD is shown as a black dashed line in arbitrary units

Figure 6.9: Density profile of a 12 Å pore for i-octane (blue dashed line with blue crosses) and toluene (green dashed-line with green crosses) at 2.88 bar. The majority of i-octane is found in the centre of the pore, although the profile features three peaks in density. Two distinct layers of toluene can be seen. Density is given in reduced units of $\rho/\rho_{i_{max}}$, where $\rho_{i_{max}}$ is the total density of species i in the pore, the density profile essentially shows the chance of observing a molecule in a given cross-section of the pore.

Figure 6.10: On the left: predicted adsorption isotherms for binary toluene (75 %, green line) and n-heptane (25 %, red line) mixture in CCD at 420 K. On the right: selectivity in the binary toluene : n-heptane system as a function of pressure for CCD at 420 K.

Figure 6.11: Selectivity of toluene over n-heptane in a 75 :25 mixture at 420 K as a function of pore width for high (2.8 bar, black circles) and low pressure (0.1 bar, red circles). Selectivity value of 1 is shown as a green dashed line. Estimations for available errors in selectivity are shown by the appropriate error bars, calculated using the root mean squared method. The PSD for CCD is shown as a black dashed line in arbitrary units.

Figure 6.12: Predicted adsorption isotherms for binary mixtures on IVD at 390 K (left panel) and the associated selectivity isotherm (right panel). From top to bottom, the binary mixtures are: From top to bottom binary mixtures are: i-octane(75 %) / n-heptane (25 %); i-octane(50 %) / toluene(50 %); and n-heptane (25 %) / toluene(75%); i-octane is shown in blue, n-heptane in red and toluene in green, respectively. Selectivity isotherms are shown in black.

Figure 6.13: On the left: predicted adsorption isotherms for a ternary mixture of i-octane (blue line), toluene (green line) and n-heptane (red line) in IVD at 390 K. Ratios are on a liquid volume basis, and correspond to 3 : 3 : 1 for i-octane, toluene and n-heptane respectively. On the right: selectivity of combined i-octane and toluene species over n-heptane in the same system.

Figure 6.14: On the left: predicted adsorption isotherms for a ternary mixture of i-octane (blue line), toluene (green line) and n-heptane (red line) in CCD at 420 K. Ratios are on a liquid volume basis, and correspond to 3 : 3 : 1 for i-octane, toluene and n-heptane respectively. On the right: selectivity of combined i-octane and toluene species over n-heptane in the same system.

Figure 7.1: Adsorption isotherms for i-octane (blue line), n-heptane (red line) and toluene (green line) in an ink-bottle pore consisting of two adjacent pores, of 10 Å and 33.45 Å widths. Isotherms are plotted as molecules per unit-cell versus fugacity. Visualisations of the systems are shown in Figure 7.2

Figure 7.2: Visualisations for the single component adsorption of i-octane (left column), n-heptane (middle column) and toluene (right column) in an ink-bottle pore at 390 K. From top to bottom, the pressures of the systems are: 0.01 bar, 0.1 bar, 0.6 bar (for i-octane, the system is at 0.55 bar which is just prior capillary condensation) and 1 bar.

Figure 7.3: Preliminary mean square displacement results for i-octane (blue lines), n-heptane (red lines) and toluene (green lines) in a 10 Å pore (left) and 40 Å pores (right) at 420 K. Simulations were run at low loading densities, which in the 10 Å equated to 5 molecules in the 10 Å pore, and 46 molecules in the 40 Å pore.

Figure 7.4: The top figure shows the initial configuration for a binary mixture of 50 i-octane and 50 n-heptane molecules in the vicinity of several 10 Å slit pores at 390 K. The bottom figure shows the final configuration of the same system after 200 nano-seconds of simulation time.

Figure D.1: Experimental adsorption isotherms for n-heptane (red line) and benzene (black line) on two carbon fibers at 303 K. The left panel shows adsorption on AF1500-Ar(1300), the right panel shows adsorption on AF1500-Ar(1500).

List of Tables

Appendix A

Economic Worth of Deposit Control Additives in Europe

The Technical Committee of Petroleum Additive Manufacture in Europe (ATC) released a report entitled "Fuel Additives: Use and Benefits" wherein they describe the benefits and size of the fuel additive market throughout Europe. Fuel additives are often added to help meet required demands on vehicle manufacturers, such as reduced pollutant levels, increased power, increased fuel efficiency and greater reliability of the engine. A portion of these additives includes those dedicated solely to combating engine deposits, either through reducing formation or removing existing deposits. Data from the ATC report can be used to calculate a rough estimate for the proportion of these additives that are dedicated to control of engine deposits.

From this data, treatment levels for typical multi-functional additive package range from $350-3500\,^{\mathrm{mg}}/_{\mathrm{kg}}$, which equates to 0.035 - 0.35 5 of the total fuel volume. Of these, a combination of of deposit control additives (DCA) and carrier oils (thermally stable structures designed to deliver the DCA to the required engine locations) have treatment levels between 100 - 1000 $^{\mathrm{mg}}/_{\mathrm{kg}}$, and the ratio of carrier oil : DCA is typically between 0.5 and 3.

With these numbers, it can be seen that the absolute content of DCA in fuels is usually between 25 and 666 $^{\mathrm{mg}}/_{\mathrm{kg}}$. Assuming the highest treatment levels of the overall additives, the highest treatment of DCA and the ratio of carrier oil ; DCA at 3, the overal proportion of DCA is $\frac{666}{3500} \times 100 = 0.19$, or 19% of the total additive package.

Appendix B

Critical Properties and Saturation Pressures

The critical properties, for all the species considered in this work are shown in Table B.1. Single-component saturation pressures at relavent temperatures are shown in Table B.2.

Species	T_c (K)	P_c (Bar)	ω
Ethane	305.42	48.80	0.099
n-Butane	425.18	37.97	0.199
i-Butane	408.05	37.02	0.1825
n-Heptane	540.26	27.36	0.351
n-Octane	569.32	24.87	0.393
i-Octane	543.96	25.68	0.303
Toluene	591.79	41.09	0.264

Table B.1: Critial properties at conditions of interest for species considered in this work

Species	Saturation Pressure (Bar)				
	at 420 K	at 390 K	at 298 K	at 293 K	at 278 K
Ethane	-	-	42.29	38.24	27.62
n-Butane	35.15	21.54	-	2.09	-
i-Butane	-	27.39	-	-	-
n-Heptane	3.55	1.7	-	-	-
n-Octane	-	0.79	-	-	-
i-Octane	3.33	1.64	-	-	-
Toluene	2.59	1.21	-	-	-

Table B.2: Saturation pressures at conditions of interest for species considered in this work

Appendix C

Lennard-Jones Interactions and Intramolecular Contributions

Lennard-Jones Interaction Parameters

In Table C.1 we provide a complete list for the ϵ and σ properties used for the Lennard-Jones interaction potentials (Equation 2.11) in this work. Values are taken from the TraPPE forcefield,[53–55] and from the work of Costa and co-workers.[39,40]

	$\frac{\epsilon}{k_B}$ (K)	σ (Å)
C	0.5	6.4
$C_{Aromatic}$	21.0	3.88
CH	10.0	4.68
$CH_{Aromatic}$	50.5	3.695
CH_2	46.0	3.95
CH_3	98.0	3.75
C_{slit}	12.0	3.4

Table C.1: Interaction parameters for use in the Lennard-Jones interaction for all components of molecules used in this work. Values are taken from both the TraPPE forcefield and the characterisation model by Costa and co-workers.

Intramolecular Contributions

Within our molecular simulations, the bond-bending of flexible molecules (associated with chains of three interaction sites and above) is given by:

$$u_{bend}(\theta) = \frac{k_\theta}{2}\left(\theta - \theta_0\right)^2$$

In all cases, $k_\theta = 62500\,{}^{\mathrm{K}}/_{\mathrm{rad}^2}$, however the equilibrium bond angle, θ_0, depends on the central interaction group of the bond, and the different scenarios are provided in Table C.2.

	θ_0
$CH_X - CH_2 - CH_Y$	114^{o}
$CH_X - CH - CH_Y$	112^{o}
$CH_X - C - CH_Y$	109.47^{o}

Table C.2: Equilibrium bond angles used in this work, dependent on the central interaction site of the bond.

The torsional contribution to flexible molecules is given by:

$$u_{torsion}(\phi) = c_0 + c_1\left[1 + \cos(\phi)\right] + c_2\left[1 - \cos(2\phi)\right] + c_3\left[1 + \cos(3\phi)\right]$$

The values for the c_0 to c_3 constants again depend on the interaction groups within the bond. A summary of the various bond configurations for torsional angles are given in Table C.3.

	c_0 $\left({}^{\mathrm{kCal}}/_{\mathrm{mol}}\right)$	c_1 $\left({}^{\mathrm{kCal}}/_{\mathrm{mol}}\right)$	c_2 $\left({}^{\mathrm{kCal}}/_{\mathrm{mol}}\right)$	c_3 $\left({}^{\mathrm{kCal}}/_{\mathrm{mol}}\right)$
$CH_X - CH_2 - CH_2 - CH_y$	2.006	4.011	0.271	-6.288
$CH_X - CH_2 - CH - CH_y$	1.283	1.778	0.444	-3.506
$CH_X - CH_2 - C - CH_y$	0.9160	2.741	0	-3.66

Table C.3: Constants for torsional bond potentials used in this work, dependent on the central interaction sites of the bond.

Appendix D

Experimental Adsorption of n-Heptane and Benzene on Carbon Fibers

In their work on the surface fractal dimension of activated carbon fibers, Sato and co-workers experimentally investigated adsorption of benzene and n-heptane.[103] From their unpublished data we were able to plot experimental isotherms for the adsorption of benzene and n-heptane on two ACFs; KF1500-Ar(1500) and KF155-Ar(1300) at 303 K. These are shown in Figure D.1. Calculation of the Henry's constants of adsorption show a stronger affinity for benzene over n-heptane at zero loading; the values were determined as 1858.3 and 740.39 $^{\text{mmol}}/_{\text{g·bar}}$ for benzene and n-heptane on KF1500-Ar(1500), and 3264.5 and 1749.7 $^{\text{mmol}}/_{\text{g·bar}}$ for benzene and n-heptane on AF1500-Ar(1300). The KF1500-Ar(1300) and KF1500-Ar(1500) carbon fibers were generated by heating KF1500 in an argon atmosphere for 1 hour at 1300 °C and 1500 °C respectively.

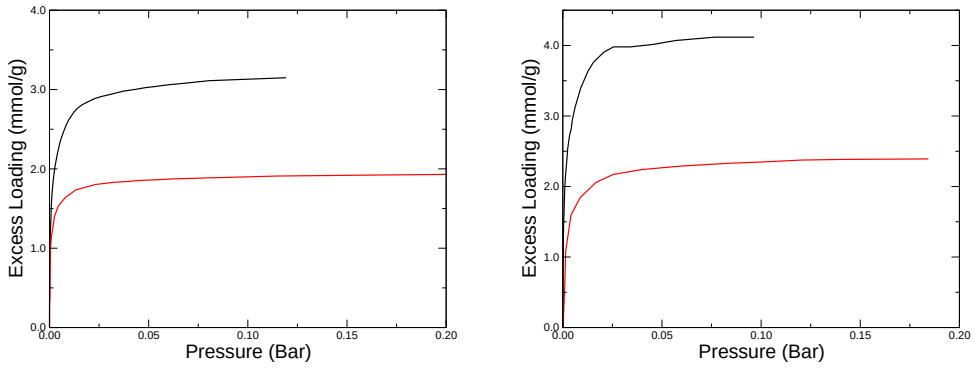

Figure D.1: Experimental adsorption isotherms for n-heptane (red line) and benzene (black line) on two carbon fibers at 303 K. The left panel shows adsorption on AF1500-Ar(1300), the right panel shows adsorption on AF1500-Ar(1500).

Appendix E

Selectivity Error Calculation Method

The errors in selectivities, shown in Table 6.1, were calculated by applying a root mean squared error analysis on the appropriate loading data for both components in each binary system. Both micro and mesopore regimes were represented by 10 Å and 40 Å pores respectively (11 Å and 40 Å in the case of the i-octane : toluene system), and both low (0.1 bar) and high (depends on the system, see Table 6.1 for values) pressures were examined.

Information on the adsorption loading as a function of simulation progression was extracted from the output files and used to calculate the root mean squared error in loading for each pressure. A selection of these outputs were taken from the end of the simulation, within the region considered as equilibrated, and error analysis was applied. We can see from Equation 4.2 that the calculation of selectivity takes the form $a = {}^{b}/_{c}$, for which the propagation of errors can be calculated using the following equation:

$$\frac{\Delta a}{a} = \sqrt{\left(\frac{\Delta b}{b}\right)^2 + \left(\frac{\Delta c}{c}\right)^2} \tag{E.1}$$

here $\frac{\Delta a}{a}$ represents the overall fractional error in selectivity, and $\frac{\Delta b}{b}$ and $\frac{\Delta c}{c}$ are the fractional errors in each component.The simulations log data to output files in blocks of varying size, depending on requirements. These are typically every 100,000 to 1,000,000 simulation steps.

Bibliography

[1] O. Altin and S. Eser. Carbon Deposit Formation From Thermal Stressing of Petroleum Fuels. *Preprint Paper - American Chemical Society, Division of Fuel Chemistry*, 49(5):764–766, 2004.

[2] T. W. Zerda, X. Yuan, S. M. Moore, and C. A. Leon y Leon. Surface area, pore size distribution and microstructure of combustion engine deposits. *Carbon*, 37(12):1999–2009, jan 1999.

[3] Z. Ye, Q. Meng, H. P. Mohamadian, J. T. Wang, L. Chen, and L. Zhu. Investigation of Deposit Formation Mechanisms for Engine In-cylinder Combustion and Exhaust Systems Using Quantitative Analysis and Sustainability Study. *International Journal of Thermophysics*, 28(3):1056–1066, 2007.

[4] J. B. Heywood. *Internal combustion engine fundamentals*, volume 21 of *McGraw-Hill series in mechanical engineering*. McGraw-Hill, 1988.

[5] M. Diaby, M. Sablier, A. Le Negrate, M. El Fassi, and J. Bocquet. Understanding carbonaceous deposit formation resulting from engine oil degradation. *Carbon*, 47(2):355–366, feb 2009.

[6] T. W. Zerda, X. Yuan, and S. M. Moore. Effects of fuel additives on the microstructure of combustion engine deposits. *Carbon*, 39(10):1589–1597, aug 2001.

[7] Automotive Council UK. Driving success - A Strategy for Growth and Sustainability in the UK Automotive Sector. Technical Report July, HM Government, 2013.

[8] C. Rhodes. The Motor Industry. Technical report, Library House of Commons, 2014.

[9] The Society of Motor Manufacturers and Traders Limited. 2014 Automotive Sustainability Report. Technical report, 2014.

[10] The Technical Committee of Petroleum Additive Manufacturers in Europe. Fuel Additives: Use and Benefits. Technical Report September, 2013.

[11] G. T. Kalghatgi. Deposits in Gasoline Engines - A Literature Review, 1990.

[12] G. T. Kalghatgi. Combustion Chamber Deposits in Spark-Ignition Engines: A Literature Review. *Society of Automotive Engineers*, (SAE 952443), oct 1995.

[13] G. Shu, L. Dong, and X. Liang. A review of experimental studies on deposits in the combustion chambers of internal combustion engines. *International Journal of Engine Research*, 13(4):357–369, 2012.

[14] D. Caceres, A. Sklyarov, A. Poehlman, and J. R. Reisel. Exhaust Emission Deterioration and Combustion Chamber Deposit Composition Over the Life Cycle of Small Utility Engines. *Journal of Engineering for Gas Turbines and Power*, 125(1):358–364, dec 2002.

[15] G. C. Smith, A. B. Hopwood, and K. J. Titchener. Microcharacterization of heavy-duty diesel engine piston deposits. *Surface and Interface Analysis*, 33(3):259–268, mar 2002.

[16] M. Z. Haji-Sulaiman and F. Mat-Isa. The effects of different gasoline blends doped with used engine oil on the forming tendency of simulated intake valve deposits. *Proceedings of The Institution of Mechanical Engineers Part D-journal of Automobile Engineering*, 213(1):47–51, 1999.

[17] J. M.C. Pinto da Costa. *Structural Characterization of Carbonaceous Engine Deposits*. PhD thesis, The University of Edinburgh, 2010.

[18] F. Jorand, M. Brun, N. Blin-Simiand, and K. Sahetchian. Formation of Combustion Chamber Deposits during Ignition Delay. *Combustion Science and Technology*, 151(1):189–203, feb 2000.

[19] M. G. Reed, T. Wilson, R. Juškaitis, and M. A. A. Neil. Surface profiling of combustion chamber deposits using aperture correlation confocal microscopy. *Journal of Microscopy*, 189(3):188–191, mar 1998.

[20] H. L. Walmsley and Personal Communication. Engine Cycle Conditions, 2008.

[21] P. Tarazona, U. M. B. Marconi, and R. Evans. Phase equilibria of fluid interfaces and confined fluids. *Molecular Physics*, 60(3):573–595, feb 1987.

[22] N. A. Seaton, J. P. R. B. Walton, and N. Quirke. A new analysis method for the determination of the pore size distribution of porous carbons from nitrogen adsorption measurements. *Carbon*, 27(6):853–861, 1989.

[23] S. Figueroa-Gerstenmaier, F. Siperstein, A. Celzard, and V. Fierro. Application of Density Functional Theory for Determining Pore-Size Distributions of Microporous Activated Carbons. *Adsorption Science & Technology*, 32(1):23–36, jan 2014.

[24] J. Jagiello and M. Thommes. Comparison of DFT characterization methods based on N2, Ar, CO2, and H2 adsorption applied to carbons with various pore size distributions. *Carbon*, 42(7):1227–1232, 2004.

[25] J. Landers, G. Y. Gor, and A. V. Neimark. Density functional theory methods for characterization of porous materials. *Colloids and Surfaces A: Physicochemical and Engineering Aspects*, 437(0):3–32, nov 2013.

[26] P. I. Ravikovitch, A. Vishnyakov, R. Russo, and A. V. Neimark. Unified Approach to Pore Size Characterization of Microporous Carbonaceous Materials from N2, Ar, and CO2 Adsorption Isotherms. *Langmuir*, 16(5):2311–2320, jan 2000.

[27] N. Quirke and S. R. R. Tennison. The interpretation of pore size distributions of microporous carbons. *Carbon*, 34(10):1281–1286, 1996.

[28] C. Lastoskie, K. E. Gubbins, and N. Quirke. Pore size heterogeneity and the carbon slit pore: a density functional theory model. *Langmuir*, 9(10):2693–2702, oct 1993.

[29] C. Lastoskie, K. E. Gubbins, and N. Quirke. Pore size distribution analysis of microporous carbons: a density functional theory approach. *The Journal of Physical Chemistry*, 97(18):4786–4796, may 1993.

[30] J. P. Olivier. Modeling physical adsorption on porous and nonporous solids using density functional theory. *Journal of Porous Materials*, 2(1):9–17, 1995.

[31] J. P. Olivier. Improving the models used for calculating the size distribution of micropore volume of activated carbons from adsorption data. *Carbon*, 36(10):1469–1472, oct 1998.

[32] V. Y. Gusev, J. A. O'Brien, and N. A. Seaton. A Self-Consistent Method for Characterization of Activated Carbons Using Supercritical Adsorption and Grand Canonical Monte Carlo Simulations. *Langmuir*, 13(10):2815–2821, may 1997.

[33] V. Y. Gusev and J. A. O'Brien. Can Molecular Simulations Be Used To Predict Adsorption on Activated Carbons? *Langmuir*, 13(10):2822–2824, may 1997.

[34] M. B. Sweatman and N. Quirke. Characterization of Porous Materials by Gas Adsorption at Ambient Temperatures and High Pressure. *The Journal of Physical Chemistry B*, 105(7):1403–1411, feb 2001.

[35] M. B. Sweatman and N. Quirke. Gas Adsorption in Active Carbons and the Slit-Pore Model 1: Pure Gas Adsorption. *The Journal of Physical Chemistry B*, 109(20):10381–10388, may 2005.

[36] R. F. Cracknell, D. Nicholson, and N. Quirke. A Grand Canonical Monte-Carlo Study of Lennard-Jones Mixtures in Slit Pores; 2: Mixtures of Two Centre Ethane with Methane. *Molecular Simulation*, 13(3):161–175, sep 1994.

[37] R. F. Cracknell and D. Nicholson. Grand canonical Monte Carlo study of Lennard-Jones mixtures in slit pores. Part 3.-Mixtures of two molecular fluids: ethane and propane. *Journal of the Chemical Society, Faraday Transactions*, 90(11):1487–1493, 1994.

[38] L. F. Vega. Chapter 5 Structural characterization of nano- and mesoporous materials by molecular simulations. In Perla B Balbuena Chemistry, Jorge M Seminario B T Theoretical, and Computational, editors, *Nanomaterials: Design and Simulation*, volume Volume 18, pages 101–126. Elsevier, 2007.

[39] J. M.C. Pinto da Costa, R. F. Cracknell, L. Sarkisov, and N. A. Seaton. Structural characterization of carbonaceous combustion-chamber deposits. *Carbon*, 47(14):3322–3331, nov 2009.

[40] J. M.C. Pinto da Costa, R. F. Cracknell, N. A. Seaton, and L. Sarkisov. Towards predictive molecular simulations of normal and branched alkane adsorption in carbonaceous engine deposits. *Carbon*, 49(2):445–456, feb 2011.

[41] G. M. Davies, N. A. Seaton, and V. S. Vassiliadis. Calculation of pore size distributions of activated carbons from adsorption isotherms. *Langmuir*, 36(6):8235–8245, 1999.

[42] G. M. Davies and N. A. Seaton. Development and Validation of Pore Structure Models for Adsorption in Activated Carbons. *Langmuir*, 15(19):6263–6276, jul 1999.

[43] G. M. Davies and N. A. Seaton. Predicting adsorption equilibrium using molecular simulation. *AIChE Journal*, 46(9):1753–1768, 2000.

[44] W. A. Steele. *The interaction of gases with solid surfaces*. International encyclopedia of physical chemistry and chemical physics: Properties of interfaces. Pergamon Press, 1974.

[45] D. Frenkel and B. Smit. *Understanding Molecular Simulation: From Algorithms to Applications*. Computational science series. Elsevier Science, 2001.

[46] N. Metropolis, A. W. Rosenbluth, M. N. Rosenbluth, A. H. Teller, and E. Teller. Equation of State Calculations by Fast Computing Machines. *The Journal of Chemical Physics*, 21(6):1087, 1953.

[47] J. I. Siepmann and D. Frenkel. Configurational bias Monte Carlo: a new sampling scheme for flexible chains. *Molecular Physics*, 75(1):59–70, jan 1992.

[48] T. J. H. Vlugt, R. Krishna, and B. Smit. Molecular Simulations of Adsorption Isotherms for Linear and Branched Alkanes and Their Mixtures in Silicalite. *The Journal of Physical Chemistry B*, 103(7):1102–1118, feb 1999.

[49] M. D. Macedonia and E. J. Maginn. A biased grand canonical Monte Carlo method for simulating adsorption using all-atom and branched united atom models. *Molecular Physics*, 96(9):1375–1390, may 1999.

[50] D. Frenkel, G. C. A. M. Mooij, and B. Smit. Novel scheme to study structural and thermal properties of continuously deformable molecules. *Journal of Physics: Condensed Matter*, 4(12):3053, 1992.

[51] M. N. Rosenbluth and A. W. Rosenbluth. Monte Carlo Calculation of the Average Extension of Molecular Chains. *The Journal of Chemical Physics*, 23(2):356, 1955.

[52] P. Allen and D. J. Tildesley. *Computer Simulation of Liquids*. Oxford Science Publ. Clarendon Press, 1989.

[53] M. G. Martin and J. I. Siepmann. Transferable Potentials for Phase Equilibria. 1. United-Atom Description of n -Alkanes. *The Journal of Physical Chemistry B*, 102(97):2569–2577, 1998.

[54] M. G. Martin and J. I. Siepmann. Novel Configurational-Bias Monte Carlo Method for Branched Molecules. Transferable Potentials for Phase Equilibria. 2. United-Atom Description of Branched Alkanes. *The Journal of Physical Chemistry B*, 103(21):4508–4517, may 1999.

[55] C. D. Wick, M. G. Martin, and J. I. Siepmann. Transferable Potentials for Phase Equilibria. 4. United-Atom Description of Linear and Branched Alkenes and Alkylbenzenes. *The Journal of Physical Chemistry B*, 104(33):8008–8016, aug 2000.

[56] J. I. Siepmann, S. Karaborni, and B. Smit. Simulating the critical behaviour of complex fluids. *Nature*, 365(6444):330–332, sep 1993.

[57] R. Q. Snurr, A. T. Bell, and D. N. Theodorou. Prediction of adsorption of aromatic hydrocarbons in silicalite from grand canonical Monte Carlo simulations with biased insertions. *The Journal of Physical Chemistry*, 97(51):13742–13752, dec 1993.

[58] A. Gupta, S. Chempath, M. J. Sanborn, L. A. Clark, and R. Q. Snurr. Object-oriented Programming Paradigms for Molecular Modeling. *Molecular Simulation*, 29(1):29–46, jan 2003.

[59] A. Harrison, R. F. Cracknell, J. Krueger-Venus, and L. Sarkisov. Branched versus linear alkane adsorption in carbonaceous slit pores. *Adsorption*, 20(2-3):427–437, 2014.

[60] F. Rouquerol, J. Rouquerol, and K. S. W. Sing. *Adsorption by Powders and Porous Solids: Principles, Methodology and Applications*. Academic Press, 1999.

[61] M. V. Lopez-Ramon, J. Jagiello, T. J. Bandosz, and N. A. Seaton. Determination of the pore size distribution and network connectivity in microporous solids by adsorption measurements and Monte Carlo simulation. *Langmuir*, 7463(3):4435–4445, 1997.

[62] K. S. W. Sing. The use of gas adsorption for the characterization of porous solids. *Colloids and Surfaces*, 38(1):113–124, jan 1989.

[63] K. S. W. Sing. Characterization of porous materials: past, present and future. *Colloids and Surfaces A: Physicochemical and Engineering Aspects*, 241(1-3):3–7, jul 2004.

[64] R. F. Cracknell, K. E. Gubbins, M. Maddox, and D. Nicholson. Modeling Fluid Behavior in Well-Characterized Porous Materials. *Accounts of Chemical Research*, 28(7):281–288, jul 1995.

[65] W. H. Press, S. A. Teukolsky, W. T. Vetterling, and B. P. Flannery. *Numerical Recipes in FORTRAN; The Art of Scientific Computing*. Cambridge University Press, New York, NY, USA, 2nd edition, 1993.

[66] K. A. Sosin and D. F. Quinn. Using the high pressure methane isotherm for determination of pore size distribution of carbon adsorbents. *Journal of Porous Materials*, 1(1):111–119, 1995.

[67] S. Scaife, P. Kluson, and N. Quirke. Characterization of Porous Materials by Gas Adsorption: Do Different Molecular Probes Give Different Pore Structures? *The Journal of Physical Chemistry B*, 104(2):313–318, jan 2000.

[68] G. M. Davies and N. A. Seaton. The effect of the choice of pore model on the characterization of the internal structure of microporous carbons using pore size distributions. *Carbon*, 36(10):1473–1490, oct 1998.

[69] M. V. Szombathely, P. Bräuer, and M. Jaroniec. The solution of adsorption integral equations by means of the regularization method. *Journal of Computational Chemistry*, 13(1):17–32, 1992.

[70] J. D. Wilson. Statistical approach to the solution of first-kind integral equations arising in the study of materials and their properties. *Journal of Materials Science*, 27(14):3911–3924, 1992.

[71] G. M. Davies. *Molecular Simulation of Adsorption Equilibrium in Microporous Solids: Model Development and Performance Prediction.* PhD thesis, University of Cambridge, 1999.

[72] E. Di Biase. *Systematic Development of Predictive Molecular Models of High Surface Area Activated Carbons for the Simulation of Multi-Component Adsorption Processes Related to Carbon Capture.* PhD thesis, The University of Edinburgh, 2014.

[73] Personal Communication. Fuel Specification.

[74] L. Sarkisov and P. A. Monson. Hysteresis in Monte Carlo and Molecular Dynamics Simulations of Adsorption in Porous Materials. *Langmuir*, 16(25):9857–9860, dec 2000.

[75] L. Sarkisov and P. A. Monson. Modeling of Adsorption and Desorption in Pores of Simple Geometry Using Molecular Dynamics. *Langmuir*, 17(24):7600–7604, nov 2001.

[76] O. Talu and A. L. Myers. Molecular simulation of adsorption: Gibbs dividing surface and comparison with experiment. *AIChE Journal*, 47(5):1160–1168, 2001.

[77] L. D. Gelb, K. E. Gubbins, R. Radhakrishnan, and M. Sliwinska-Bartkowiak. Phase separation in confined systems. *Reports on Progress in Physics*, 62(12):1573–1659, dec 1999.

[78] B. L. Severson and R. Q. Snurr. Monte Carlo simulation of n-alkane adsorption isotherms in carbon slit pores. *The Journal of Chemical Physics*, 126(13):134708, apr 2007.

[79] S. K. Singh, A. Sinha, G. Deo, and J. K. Singh. Vapor-Liquid Phase Coexistence, Critical Properties, and Surface Tension of Confined Alkanes. *Journal of Physical Chemistry C*, 113(17):7170–7180, 2009.

[80] Z. Tan and K. E. Gubbins. Selective adsorption of simple mixtures in slit pores: a model of methane-ethane mixtures in carbon. *The Journal of Physical Chemistry*, 96(2):845–854, jan 1992.

[81] R. Krishna, B. Smit, and S. Calero. Entropy effects during sorption of alkanes in zeolites. *Chem. Soc. Rev.*, 31(3):185–194, 2002.

[82] S. Calero, B. Smit, and R. Krishna. Separation of linear, mono-methyl and dimethyl alkanes in the 5-7 carbon atom range by exploiting configurational entropy effects during sorption on silicalite-1. *Phys. Chem. Chem. Phys.*, 3(19):4390–4398, 2001.

[83] J. Jiang, S. I. Sandler, M. Schenk, and B. Smit. Adsorption and separation of linear and branched alkanes on carbon nanotube bundles from configurational-bias Monte Carlo simulation. *Phys. Rev. B*, 72(4):45447, jul 2005.

[84] J. Jiang and S. I. Sandler. Monte Carlo Simulation for the Adsorption and Separation of Linear and Branched Alkanes in IRMOF-1. *Langmuir*, 22(13):5702–5707, jun 2006.

[85] D. S. Santilli. Pore probe: A new technique for measuring the concentrations of molecules inside porous materials at elevated temperatures. *Journal of Catalysis*, 99(2):335–341, jun 1986.

[86] J. Jiang and S. I. Sandler. Shape versus inverse-shape selective adsorption of alkane isomers in carbon nanotubes. *The Journal of chemical physics*, 124(2):24717, jan 2006.

[87] D. S. Santilli, T. V. Harris, and S. I. Zones. Inverse shape selectivity in molecular sieves: Observations, modelling, and predictions. *Microporous Materials*, 1(5):329–341, sep 1993.

[88] J. Jiang. Pore Size or Geometry: Which Determines the Shape and Inverse-Shape Selective Adsorption of Alkane Isomers? *The Journal of Physical Chemistry B*, 110(17):8670–8673, may 2006.

[89] J. Jiang and S. I. Sandler. Capillary Phase Transitions of Linear and Branched Alkanes in Carbon Nanotubes from Molecular Simulation. *Langmuir*, 22(17):7391–7399, aug 2006.

[90] Y. Li, Y. Yu, Y. Zheng, and J. Li. Vapor-liquid equilibrium properties for confined binary mixtures involving CO2, CH4, and N2 from Gibbs ensemble Monte Carlo simulations. *Science China Chemistry*, 55(9):1825–1831, aug 2012.

[91] A. L. Myers and P. A. Monson. Physical adsorption of gases: the case for absolute adsorption as the basis for thermodynamic analysis. *Adsorption*, 20(4):591–622, 2014.

[92] W. Steele. Computer simulations of physical adsorption: a historical review. *Applied Surface Science*, 196(1-4):3–12, aug 2002.

[93] P. Kowalczyk, E. A. Ustinov, A. P. Terzyk, P. A. Gauden, K. Kaneko, and G. Rychlicki. Description of benzene adsorption in slit-like pores. Theoretical foundations of the improved Horvath-Kawazoe method. *Carbon*, 42(4):851–864, 2004.

[94] X. S. Zhao, Q. Ma, and G. Q. Lu. VOC Removal: Comparison of MCM-41 with Hydrophobic Zeolites and Activated Carbon. *Energy & Fuels*, 12(6):1051–1054, 1998.

[95] D. D. Do and H D Do. Effects of adsorbate- adsorbate interaction in the description of adsorption isotherm of hydrocarbons in micro-mesoporous carbonaceous materials. *Applied Surface Science*, 196(1-4):13–29, aug 2002.

[96] C. Wang, K. Chang, T. Chung, and H. Wu. Adsorption Equilibria of Aromatic Compounds on Activated Carbon, Silica Gel, and 13X Zeolite. *Journal of Chemical & Engineering Data*, 49(3):527–531, may 2004.

[97] W. Zhang, Z. Qu, X. Li, Y. Wang, D. Ma, and J. Wu. Comparison of dynamic adsorption/desorption characteristics of toluene on different porous materials. *Journal of Environmental Sciences*, 24(3):520–528, mar 2012.

[98] E. Díaz, S. Ordóñez, A. Vega, and J. Coca. Adsorption characterisation of different volatile organic compounds over alumina, zeolites and activated carbon using inverse gas chromatography. *Journal of Chromatography A*, 1049(1-2):139–146, sep 2004.

[99] M. A. Lillo-Ródenas, A. J. Fletcher, K. M. Thomas, D. Cazorla-Amorós, and A. Linares-Solano. Competitive adsorption of a benzene-toluene mixture on activated carbons at low concentration. *Carbon*, 44(8):1455–1463, jul 2006.

[100] N. Klomkliang, D. D. Do, and D. Nicholson. Affinity and Packing of Benzene, Toluene, and p-Xylene Adsorption on a Graphitic Surface and in Pores. *Industrial & Engineering Chemistry Research*, 51(14):5320–5329, apr 2012.

[101] J. P. Fox and S. P. Bates. Simulating the Adsorption of Binary and Ternary Mixtures of Linear, Branched, and Cyclic Alkanes in Zeolites. *The Journal of Physical Chemistry B*, 108(44):17136–17142, nov 2004.

[102] J. Liu and M. D. LeVan. Henrys law constants and isosteric heats of adsorption at zero loading for multi-wall carbon surfaces with different geometries. *Carbon*, 48(12):3454–3462, oct 2010.

[103] M. Sato, T. Sukegawa, T. Suzuki, S. Hagiwara, and K. Kaneko. Surface fractal dimensional change of microporous carbon fibers with partial graphitization. *Chemical Physics Letters*, 181(6):526–530, jul 1991.

[104] A. A. Isirikyan and A. V. Kiselev. The Absolute Adsorption Isotherms of Vapors of Nitrogen, Benzene and n-Hexane, and the Heats of Adsorption of Benzene and n-Hexane on Graphitized Carbon Blacks . I. Graphitized Thermal Blacks. *The Journal of Physical Chemistry*, 65(4):601–607, apr 1961.

[105] Qiong Cai. *A Hybrid Molecular Dynamics SImulation/Pore Network Model of Diffusion in Nanoporous Carbons*. PhD thesis, The University of Edinburgh, 2007.